

**FABRICATION OF CRYSTALLINE COLLOIDAL ARRAY PHOTONIC CRYSTALS  
AND APPLICATIONS**

by

**Luling Wang**

B.S. in Chemistry, Wuhan University, 2004

M.S. in Polymer Chemistry and Physics, Wuhan University, 2006

Submitted to the Graduate Faculty of the Kenneth P.

Dietrich School of Arts and Sciences in

partial fulfillment of the requirements for

the degree of Doctor of Philosophy

University of Pittsburgh

2012

UNIVERSITY OF PITTSBURGH  
DIETRICH SCHOOL OF ARTS AND SCIENCES

This dissertation was presented

by

Luling Wang

It was defended on

December 14, 2011

and approved by

Haitao Liu, Assistant Professor, Departmental of Chemistry

Nathaniel L. Rosi, Assistant Professor, Department of Chemistry

Sachin Velankar, Associate Professor, Department of Chemical and Petroleum Engineering

Dissertation Advisor: Sanford A. Asher, Distinguished Professor, Department of Chemistry

Copyright © by Luling Wang

2012

# **FABRICATION OF CRYSTALLINE COLLOIDAL ARRAY PHOTONIC CRYSTALS AND APPLICATIONS**

Luling Wang, PhD

University of Pittsburgh, 2012

Crystalline colloidal array (CCA) photonic crystals (PCs) are periodic structures formed by the self-assembly of monodisperse, highly-charged particles in low ionic strength aqueous solutions. Similar to an atomic crystal but with much larger lattice spacings, the CCA can efficiently diffract light in the UV, visible and near-IR spectral regions.

This thesis reports the development of new CCA materials, novel CCA Bragg diffraction devices, and utilization of CCA PC templates for new nanostructure and nanomaterial fabrication. We use CCA for development of a CCA deep UV narrow band filter that acts as a Rayleigh rejection filter for UV Raman spectroscopy and for templates for solid-state UV Raman cross section determinations.

We developed novel CCA PC deep UV Bragg diffraction devices. We synthesized small, monodisperse, highly surface-charged silica particles and prepared novel silica CCA through the self-assembly of these particles. The silica CCA efficiently Bragg diffract light in the deep UV. The diffracted wavelength was varied by tilting the CCA orientation to the incident beam. We demonstrated the utility of the silica CCA filter as a Rayleigh rejection filter in Teflon UV Raman measurements.

We conducted the first resonance Raman cross-section measurements of solids that avoids self-absorption bias by using PC templates. We fabricated complex stoichiometrically defined nanoparticles ( $\text{NaNO}_3/\text{Na}_2\text{SO}_4$  nanoparticles) by utilizing the defined interstitial volume

of close-packed PCs. We successfully determined the solid-state  $\text{NaNO}_3$  UV resonance Raman cross-sections by using solid  $\text{Na}_2\text{SO}_4$  as an internal standard. We also developed a refractive-index matching method to measure solid-state  $\text{Na}_2\text{SO}_4$  UV Raman cross sections that avoids the effect of the local field and avoids interface scattering of the incident light.

We developed a facile method to fabricate silica shell PCs through the use of flexible poly(N-isopropylacrylamide) (PNIPAm) core templates. We synthesized monodisperse PNIPAm-silica core-shell particles and demonstrated their reversible swelling and shrinking as the temperature is cycled. We fabricated close-packed PCs of PNIPAm-silica core-shell particles and further fabricated hollow silica shell PCs by removing the PNIPAm cores by calcination.

## TABLE OF CONTENTS

|                                                                                                 |           |
|-------------------------------------------------------------------------------------------------|-----------|
| <b>PREFACE.....</b>                                                                             | <b>XV</b> |
| <b>1.0 INTRODUCTION.....</b>                                                                    | <b>1</b>  |
| <b>1.1 LIGHT DIFFRACTION FROM PHOTONIC CRYSTALS.....</b>                                        | <b>4</b>  |
| 1.1.1 Bragg’s Law.....                                                                          | 4         |
| 1.1.2 Experimental Measurements of Photonic Crystal Light Diffraction.....                      | 6         |
| <b>1.2 CCA PARTICLE SYNTHESIS AND SELF-ASSEMBLY .....</b>                                       | <b>8</b>  |
| 1.2.1 Synthesis of Polymeric CCA Particles .....                                                | 13        |
| 1.2.2 Synthesis of Inorganic CCA Particles .....                                                | 14        |
| 1.2.3 Synthesis of Hybrid Particles .....                                                       | 14        |
| <b>1.3 CCA APPLICATIONS .....</b>                                                               | <b>15</b> |
| 1.3.1 CCA Optical Filters .....                                                                 | 15        |
| 1.3.2 CCA Sensing Materials .....                                                               | 17        |
| 1.3.3 Other CCA applications.....                                                               | 19        |
| <b>1.4 OVERVIEW OF RESEARCH PROGRAM.....</b>                                                    | <b>21</b> |
| <b>1.5 REFERENCES .....</b>                                                                     | <b>24</b> |
| <b>2.0 SILICA CRYSTALLINE COLLOIDAL ARRAY DEEP UV NARROW BAND<br/>DIFFRACTION DEVICES .....</b> | <b>31</b> |
| <b>2.1 INTRODUCTION .....</b>                                                                   | <b>32</b> |

|              |                                                                                                                                                                |           |
|--------------|----------------------------------------------------------------------------------------------------------------------------------------------------------------|-----------|
| <b>2.2</b>   | <b>EXPERIMENTAL SECTION.....</b>                                                                                                                               | <b>33</b> |
| <b>2.2.1</b> | <b>Fabrication of Highly Charged Monodisperse Small Silica Particles....</b>                                                                                   | <b>33</b> |
| <b>2.2.2</b> | <b>Silica CCA Fabrication and Transmission Measurements.....</b>                                                                                               | <b>34</b> |
| <b>2.2.3</b> | <b>Silica CCA Rayleigh Rejection Filter Raman Measurements .....</b>                                                                                           | <b>36</b> |
| <b>2.2.4</b> | <b>Characterization Techniques.....</b>                                                                                                                        | <b>36</b> |
| <b>2.3</b>   | <b>RESULTS AND DISCUSSION .....</b>                                                                                                                            | <b>37</b> |
| <b>2.3.1</b> | <b>Fabrication of Highly Charged, Monodisperse, Small Silica Particles..</b>                                                                                   | <b>37</b> |
| <b>2.3.2</b> | <b>Transmission Measurements of Silica CCA .....</b>                                                                                                           | <b>41</b> |
| <b>2.3.3</b> | <b>Utilization of CCA for UV Raman Rayleigh Rejection.....</b>                                                                                                 | <b>46</b> |
| <b>2.4</b>   | <b>CONCLUSIONS .....</b>                                                                                                                                       | <b>50</b> |
| <b>2.5</b>   | <b>ACKNOWLEDGEMENT .....</b>                                                                                                                                   | <b>51</b> |
| <b>2.6</b>   | <b>REFERENCES .....</b>                                                                                                                                        | <b>51</b> |
| <b>3.0</b>   | <b>TEMPLATED PHOTONIC CRYSTAL FABRICATION OF<br/>STOICHIOMETRICALLY COMPLEX NANOPARTICLES FOR RESONANCE<br/>RAMAN SOLID CROSS SECTION DETERMINATIONS .....</b> | <b>54</b> |
| <b>3.1</b>   | <b>INTRODUCTION .....</b>                                                                                                                                      | <b>55</b> |
| <b>3.2</b>   | <b>EXPERIMENTAL SECTION.....</b>                                                                                                                               | <b>56</b> |
| <b>3.2.1</b> | <b>Preparation of Close-Packed Silica PCs .....</b>                                                                                                            | <b>56</b> |
| <b>3.2.2</b> | <b>Formation of NaNO<sub>3</sub>/Na<sub>2</sub>SO<sub>4</sub> NPs in Close-packed PCs Interstices .....</b>                                                    | <b>57</b> |
| <b>3.2.3</b> | <b>Characterization .....</b>                                                                                                                                  | <b>57</b> |
| <b>3.2.4</b> | <b>Raman of NaNO<sub>3</sub>/Na<sub>2</sub>SO<sub>4</sub> NPs in PC Interstices .....</b>                                                                      | <b>59</b> |
| <b>3.3</b>   | <b>RESULTS AND DISCUSSION .....</b>                                                                                                                            | <b>59</b> |
| <b>3.4</b>   | <b>CONCLUSIONS.....</b>                                                                                                                                        | <b>68</b> |

|       |                                                                                                                                                                     |    |
|-------|---------------------------------------------------------------------------------------------------------------------------------------------------------------------|----|
| 3.5   | ACKNOWLEDGEMENTS .....                                                                                                                                              | 68 |
| 3.6   | REFERENCES .....                                                                                                                                                    | 69 |
| 4.0   | REFRACTIVE-INDEX MATCHING AVOIDS LOCAL FIELD<br>CORRECTIONS AND SCATTERING BIAS IN SOLID-STATE $\text{Na}_2\text{SO}_4$ UV RAMAN<br>CROSS SECTION MEASUREMENTS..... | 71 |
| 4.1   | INTRODUCTION .....                                                                                                                                                  | 72 |
| 4.2   | EXPERIMENTAL SECTION.....                                                                                                                                           | 74 |
| 4.2.1 | UV Raman Spectroscopy Instrumentation.....                                                                                                                          | 74 |
| 4.2.2 | UV Raman Measurements of Acetonitrile, Chloroform and<br>Chloroform/Acetonitrile .....                                                                              | 74 |
| 4.2.3 | UV Raman Measurements of Chloroform and $\text{Na}_2\text{SO}_4$ /Chloroform<br>Dispersion .....                                                                    | 76 |
| 4.2.4 | UV Raman Measurements of Acetonitrile and $\text{Na}_2\text{SO}_4$ / acetonitrile.....                                                                              | 78 |
| 4.3   | RESULTS AND DISCUSSION .....                                                                                                                                        | 78 |
| 4.3.1 | Dependence of Raman Cross Sections on the Local Field.....                                                                                                          | 78 |
| 4.3.2 | Chloroform 244 nm UV Raman Cross Section Determination .....                                                                                                        | 81 |
| 4.3.3 | 244 nm UV Raman Spectra of Chloroform and $\text{Na}_2\text{SO}_4$ /Chloroform...                                                                                   | 83 |
| 4.3.4 | UV Raman Spectra of Acetonitrile and $\text{Na}_2\text{SO}_4$ /acetonitrile.....                                                                                    | 85 |
| 4.4   | CONCLUSIONS .....                                                                                                                                                   | 87 |
| 4.5   | ACKNOWLEDGEMENT .....                                                                                                                                               | 88 |
| 4.6   | REFERENCES .....                                                                                                                                                    | 88 |
| 5.0   | FABRICATION OF SILICA SHELL PHOTONIC CRYSTALS THROUGH<br>FLEXIBLE CORE TEMPLATES .....                                                                              | 91 |

|            |                                                                     |            |
|------------|---------------------------------------------------------------------|------------|
| <b>5.1</b> | <b>INTRODUCTION .....</b>                                           | <b>92</b>  |
| <b>5.2</b> | <b>EXPERIMENTAL SECTION.....</b>                                    | <b>95</b>  |
| 5.2.1      | Preparation of monodisperse PNIPAm core particles .....             | 95         |
| 5.2.2      | Preparation of PNIPAm-silica core-shell particles .....             | 95         |
| 5.2.3      | Fabrication of silica shell PC .....                                | 96         |
| 5.2.4      | Characterization .....                                              | 96         |
| <b>5.3</b> | <b>RESULTS AND DISCUSSION .....</b>                                 | <b>97</b>  |
| <b>5.4</b> | <b>CONCLUSIONS .....</b>                                            | <b>109</b> |
| <b>5.5</b> | <b>ACKNOWLEDGMENT .....</b>                                         | <b>110</b> |
| <b>5.6</b> | <b>REFERENCES .....</b>                                             | <b>110</b> |
| <b>6.0</b> | <b>SUMMARY AND FUTURE WORK .....</b>                                | <b>114</b> |
| <b>6.1</b> | <b>SUMMARY OF WORK .....</b>                                        | <b>114</b> |
| <b>6.2</b> | <b>FUTURE WORK.....</b>                                             | <b>115</b> |
| 6.2.1      | Future work in the silica CCA deep UV narrow band rejection filter  | 115        |
| 6.2.1.1    | Improvement of the ordering of the silica CCA.....                  | 115        |
| 6.2.1.2    | Silica CCA solidification.....                                      | 120        |
| 6.2.1.3    | Silica CCA for imaging applications .....                           | 120        |
| 6.2.2      | Future work in solid-state UV Raman cross-section determinations .. | 123        |
| <b>6.3</b> | <b>REFERENCES .....</b>                                             | <b>124</b> |

## LIST OF TABLES

|                                                                            |    |
|----------------------------------------------------------------------------|----|
| Table 1-1 Summary of Photonic Crystal Research from Other Groups .....     | 3  |
| Table 2-1 Dependence of Silica CCA Particle Surface Charge on THOPS* ..... | 39 |

## LIST OF FIGURES

|                                                                                                                                                                                                                                                                                                                                                                                                                                                                                                                                                                             |    |
|-----------------------------------------------------------------------------------------------------------------------------------------------------------------------------------------------------------------------------------------------------------------------------------------------------------------------------------------------------------------------------------------------------------------------------------------------------------------------------------------------------------------------------------------------------------------------------|----|
| Figure 1.1 Derivation of Bragg's law. ....                                                                                                                                                                                                                                                                                                                                                                                                                                                                                                                                  | 5  |
| Figure 1.2 (a) Reflectance and (b) transmission measurements of photonic crystal light diffraction.....                                                                                                                                                                                                                                                                                                                                                                                                                                                                     | 7  |
| Figure 1.3 (a) BCC and (b) FCC structures. ....                                                                                                                                                                                                                                                                                                                                                                                                                                                                                                                             | 9  |
| Figure 1.4 Highly charged monodisperse polystyrene particles self-assemble into a CCA ( <i>from Asher, S. A.; Holtz, J.; Liu, L.; Wu, Z. J., J. Am. Chem. Soc. 1994, 116, 4997</i> ).....                                                                                                                                                                                                                                                                                                                                                                                   | 11 |
| Figure 1.5 (a) A typical setup for synthesis of polymeric particles ( <i>from Asher's group website</i> ); (b) A TEM image of PS particles with a diameter of 565 nm ( <i>from Reese, C. E.; Asher, S. A. J. Colloid interface Sci. 2002, 248, 41.</i> ); (c) A TEM image of PNIPAm particles with a diameter of ~300 nm ( <i>from Wang, L.; Asher, S. A. Chem. Mater. 2009, 21, 4608.</i> ); (d) Dependences of PNIPAm colloid diameter and turbidity on temperature ( <i>from Weissman, J. M.; Sunkara H. B.; Tse, A. S.; Asher, S. A. Science 1996, 274, 959.</i> )..... | 12 |
| Figure 1.6 (a) The orientation of a CCA filter to the incident light beam; (b) Spectra showing transmission through the CCA filter at an incident glancing angle of 90° and 80° ( <i>from Asher S. A.; Flaugh, P. L.; Washinger, G. Spectroscopy 1986, 1, 26.</i> ).....                                                                                                                                                                                                                                                                                                    | 16 |
| Figure 1.7 PCCA photonic crystal sensing materials consist of an embedded CCA in a hydrogel network functionalized with a molecular recognition element. The diffracted wavelength red                                                                                                                                                                                                                                                                                                                                                                                      |    |

shifts result from the hydrogel volume increase induced by the interaction of the analyte with the molecular recognition element in the hydrogel (from Asher, S. A. et al. *J. Am. Chem. Soc.* 2003, 125, 3322.). ..... 18

Figure 1.8 Fabrication of a PCCA of water voids. (1) Monodisperse silica particles self-assemble into a CCA; (2) The silica CCA is immobilized within a polyacrylamide hydrogel network to form a PCCA; (3) Silica particles are etched out with HF acid to result in a PCCA of water voids (from Liu, L.; Li, P.; Asher, S. A. *Nature* 1999, 397, 141.). ..... 20

Figure 2.1 (a) A CCA flow cell for transmission measurements; (b) Schematic of triple-stage monochromator for Raman measurements. .... 35

Figure 2.2 TEM images of (a) the Stöber silica particles; (b) the silica CCA particles. .... 38

Figure 2.3 TEM images of samples (a) synthesized with 10 mL and (b) 15 mL of ammonium hydroxide in the Stöber silica synthesis. 2 mL of THOPS was added in the surface modification. Other conditions are those of the typical recipe..... 40

Figure 2.4 Transmission spectrum of flow cell filled with pure water; and of the flow cells filled with highly charged silica CCA dispersion for incident glancing angles of 90°, 69° and 66°. Silica colloid diameter is  $47.3 \pm 5.1$  nm. .... 43

Figure 2.5 Observed and calculated transmission spectrum of diffraction by silica CCA at a 90° incident angle. .... 45

Figure 2.6 Teflon 229 nm UV Raman spectra in the absence (-----) and presence (——) of the CCA filter at an incident glancing angle of ~69°. In addition, the Raman spectrum is shown for the CCA close to normal incidence (— · —). The inset shows an expansion of the circled region. .... 47

Figure 2.7 Transmission calculated from the ratios of integrated intensities of Teflon Raman Bands in Fig. 2.6 for CCA at glancing incident angle of  $\sim 69^\circ$  (the dots, blue); Also shown are transmission data from Fig. 2.4 for CCA at glancing incident angle of  $\sim 69^\circ$  (the squares, red). For comparison, the Raman shifts and corresponding wavelengths were listed next to the data. 49

Figure 3.1 (a) TEM image of original silica colloid; (b) TEM image of silica colloid after cleaning and fractionation..... 58

Figure 3.2 Templated fabrication of nanoparticles in PC interstices..... 60

Figure 3.3 (a) SEM of close-packed PC; (b) Optical image of the close-packed silica PC; (c) SEM image of close-packed PC with NPs ( $\text{NaNO}_3$  to  $\text{Na}_2\text{SO}_4$  mole ratio 1:40) formed in the interstices; (d) Raman spectra of the PCs with NPs in the interstices (red), PC reference (green) and double stick tape..... 61

Figure 3.4 Raman spectra of the  $\text{NaNO}_3/\text{Na}_2\text{SO}_4$  nanoparticles ( $\text{NaNO}_3$  to  $\text{Na}_2\text{SO}_4$  mole ratio 1:40) in the PC interstices at illuminating times of 60 s, 120 s, 180 s and 240 s respectively. .... 66

Figure 3.5 Raman spectra of the  $\text{NaNO}_3/\text{Na}_2\text{SO}_4$  nanoparticles ( $\text{NaNO}_3$  to  $\text{Na}_2\text{SO}_4$  mole ratio 1.67:1) in the PC interstices under the spinning (blue) and stationary (red) conditions..... 67

Figure 4.1 UV-Vis absorbance spectra of pure chloroform, pure acetonitrile and 13.1 wt%  $\text{Na}_2\text{SO}_4$  in water. .... 75

Figure 4.2 Optical image of ground solid  $\text{Na}_2\text{SO}_4$  particles. .... 77

Figure 4.3 UV Raman spectra of chloroform (dashed line), acetonitrile (dotted line), and chloroform/acetonitrile mixture (volume ratio, 1:3, solid line). .... 82

Figure 4.4 UV Raman spectra of liquid chloroform and chloroform with increasing amounts of solid  $\text{Na}_2\text{SO}_4$  particles of 23.6 mg/mL, 29.8 mg/mL, and 86.6 mg/mL. Raman spectra were normalized to the chloroform  $668\text{ cm}^{-1}$  band..... 84

|                                                                                                                                                                                                                                                                                                                                      |     |
|--------------------------------------------------------------------------------------------------------------------------------------------------------------------------------------------------------------------------------------------------------------------------------------------------------------------------------------|-----|
| Figure 4.5 UV Raman spectra of liquid acetonitrile and acetonitrile with increasing amounts of solid Na <sub>2</sub> SO <sub>4</sub> particles of 19.4 mg/mL, 29.0 mg/mL, and 52.1 mg/mL. Raman spectra were normalized to the acetonitrile 1375 cm <sup>-1</sup> band.....                                                          | 86  |
| Figure 5.1 (a) TEM image of PNIPAm core particles. (b) Photograph of Bragg diffraction from PNIPAm core particles. ....                                                                                                                                                                                                              | 100 |
| Figure 5.2 Temperature dependence of diameter and turbidity of PNIPAm Particles. ....                                                                                                                                                                                                                                                | 101 |
| Figure 5.3 TEM of PNIPAm core particles after silica coating at (a) pH11.0 and (b) pH 8.0 (the inset shows a core-shell particle at higher magnification; the scale bar is 500 nm).....                                                                                                                                              | 103 |
| Figure 5.4 Temperature dependence of the DLS measured apparent particle diameter of the PNIPAm-silica core-shell particles (solid line drawn to help the eye). ....                                                                                                                                                                  | 103 |
| Figure 5.5 SEM of (a) unordered and (b) ordered close-packed silica-shell/ PNIPAm-core particles. ....                                                                                                                                                                                                                               | 105 |
| Figure 5.6 (a) SEM image of the cross section of silica shell photonic crystals. (b) TEM image of the silica shell photonic crystals. ....                                                                                                                                                                                           | 106 |
| Figure 5.7 Reflectance spectrum of silica shell photonic crystals in air (solid line) and water (dash line).....                                                                                                                                                                                                                     | 108 |
| Figure 6.1 Silica particles synthesized by water-in-oil microemulsion.....                                                                                                                                                                                                                                                           | 117 |
| Figure 6.2 (a) Scheme of the air-pulse-drive system for the uniform colloidal crystal fabrications; (b) Transmission spectra for colloidal crystals produced at various $\Delta P$ : $\Delta P$ is the difference from atmospheric pressure. (Both (a) and (b) are from Kanai et al., <i>Adv. Funct. Mater.</i> 2005, 15, 25.). .... | 119 |
| Figure 6.3 A diagram of a hyperspectral imaging device utilizing a CCA deep UV wavelength-selecting device that allows wavelength tuning with a stationary camera.....                                                                                                                                                               | 122 |

## PREFACE

I would like to thank my research advisor, Professor Sanford Asher, for his mentorship and support all these years during my graduate studies. He has provided great opportunity, fertile research environment, and significant guidance for each student in the group to be a good scientist and to be successful. I feel extremely lucky to have the opportunity to learn from him and to work with him. No matter where I am, I will continuously remind myself to be successful and to be prepared.

I also want to thank the members of the Asher Research Group for their discussion, collaboration, and friendship. I would like to thank specially Dr. Alexander Tikhonov, David Tuschel, Dr. Jiantao Zhang, Dr. Dan Qu, Dr. Sergei Bykov, Dr. Michelle Muscatello, Dr. Justin Bohn, Jia Luo, Zhenmin Hong, and Lu Ma for their scientific discussion and collaboration. I want also to especially thank Sharon Mansfield for always being so helpful and supportive.

I would like to thank the members of my comprehensive (C), proposal (P), and dissertation (D) committees: Dr. Nathaniel Rosi (C, P, D), Dr. Haitao Liu (P, D), Dr. David Waldeck (P), Dr. Sachin Velankar (D), and Dr. Tara Meyer (C). I highly appreciate your advice and time during my PhD studies.

I also want to thank Fran Nagy for the help on the PhD program, Lori Neu (Glass Shop) and Jeff Sicher (Machine Shop) for the help on building freeze-drying instruments, Tom Gasmire

(Machine Shop) for the help on making different experimental parts, Thomas Harper (Department of Biological Sciences) for the help on TEM, Albert Stewart (Mechanical Engineering & Materials Science) for the help on SEM.

Finally, I would like to thank my family for the infinite love, encouragement, and support. My parents didn't have opportunities to get good education when they were young: my father didn't finish the middle school; my mom didn't finish the elementary school. They had to work extremely hard to support their families at that time. However, they knew the importance of knowledge and they created the best learning environment they could offer for my sister and me. We went to the Top University in China. I am very proud of my parents and deeply appreciate their love, encouragement, and support. I want also to thank my husband, Peng Zheng, for his love and support. We are from different provinces of China but get to know each other in Pittsburgh. He is always there to help me and support me with great patience. I am thankful for our small home that we build with love, peace, and happiness. I want also to thank my sister, Yaling Wang, for her love and support and for taking care of parents in China. She is an amazing sister and I am proud of her. Thanks for all the friends in my life!

## 1.0 INTRODUCTION

Photonic crystals are of great interest because they can be used to control and manipulate the propagation of light.<sup>1-11</sup> In 1987, Yablonovitch<sup>12</sup> and John<sup>13</sup> theoretically predicted that structures with periodic variations in dielectric constant could profoundly impact the propagation of light in materials. Photonic crystals are composed of spatially periodic structures of varying refractive indices that affect the propagation of electromagnetic radiations.<sup>14</sup> Similar to a semiconductor having a bandgap between the conduction and valence bands, photonic crystals have photonic bandgaps that prevent light from propagating in certain directions with specified frequencies (for instance, a certain range of wavelengths, or colors of light).<sup>2, 14, 15</sup> Photonic bandgap structures have been developed for many applications such as optical filters,<sup>16-18</sup> optical switches,<sup>19-22</sup> sensors,<sup>23-26</sup> coatings,<sup>27-29</sup> control of spontaneous emission,<sup>30</sup> lasers,<sup>31, 32</sup> on-chip optical circuitry,<sup>33, 34</sup> and fiber optics.<sup>35, 36</sup>

Over the past two decades, many methods have been developed to fabricate photonic crystals with one-, two- or three-dimensional periodicities at different length scales.<sup>4-6, 37-50</sup> These methods include holographic lithography,<sup>40, 41</sup> chemical vapor deposition,<sup>47, 48</sup> electrochemical etching,<sup>49, 50</sup> layer-by-layer stacking,<sup>45, 46</sup> and colloidal particle self-assembly.<sup>4, 6, 8, 42-44</sup> Photonic crystals that operate from the UV to visible range made through colloidal particle self-assembly have attracted great attention because of their low cost and facile fabrication compared to those fabricated using other nanostructure fabrication methods.<sup>3, 4, 6, 42, 43</sup> The photonic crystals

fabricated by colloidal self-assembly are usually called colloidal photonic crystals or crystalline colloidal array (CCA) photonic crystals.

The Asher Research Group at the University of Pittsburgh has made significant contributions to design, fabrication, and applications of diverse CCA photonic crystals.<sup>21, 42, 43, 51-63</sup> These CCA photonic crystals have also been polymerized within hydrogels to form polymerized CCA (PCCA) that optically report (i.e. color change or wavelength shift) the hydrogel volume changes in response to targeted analytes.<sup>23-26, 64-72</sup> Recently, the Asher group developed a facile method to fabricate 2-D photonic crystals and utilized 2-D photonic crystals for sensing applications.<sup>73,74</sup> The photonic crystal research by other groups is summarized in Table 1-1.

**Table 1-1** Summary of Photonic Crystal Research from Other Groups

| <b>Research Group</b> | <b>Institution/University</b>              | <b>Photonic Crystal Research</b>                                                                                        |
|-----------------------|--------------------------------------------|-------------------------------------------------------------------------------------------------------------------------|
| The Sailor Group      | University of California, San Diego        | “Smart dust” (porous Si photonic crystal particles) for sensing of organic vapors. <sup>9, 75, 76</sup>                 |
| The Norris Group      | University of Minnesota                    | Convective assembly method for colloidal photonic crystals. <sup>6, 77</sup>                                            |
| The Stein Group       | University of Minnesota                    | Colloidal crystal templates for inverse opals (three-dimensionally ordered macroporous structures). <sup>78, 79</sup>   |
| The Braun Group       | University of Illinois at Urbana-Champaign | 3-D colloidal photonic crystals for solar cell <sup>80</sup> and optoelectronic device applications. <sup>81</sup>      |
| The Cunningham Group  | University of Illinois at Urbana-Champaign | Photonic crystals for biosensing applications. <sup>82</sup>                                                            |
| The Lyon Group        | Georgia Institute of Technology            | Microgel colloidal crystals <sup>8</sup>                                                                                |
| The Yin Group         | University of California, Riverside        | Self-assembly method for magnetically responsive photonic crystals. <sup>3</sup>                                        |
| The Jiang Group       | University of Florida                      | Spin-coating technique to fabricate colloidal photonic crystals for coating and sensing applications. <sup>83, 84</sup> |
| The Bartl Group       | University of Utah                         | Titania inverse opals fabricated by the combination of self-assembly and sol-gel chemistry. <sup>85</sup>               |
| The Zhao Group        | National University of Singapore           | Colloidal photonic crystals for novel porous materials fabrication and applications. <sup>86</sup>                      |
| The Gu Group          | Southeast University (China)               | Tunable photonic materials for multiplex biomolecular detection based on photonic crystals. <sup>87, 88</sup>           |
| The Jiang Group       | Chinese Academy of Sciences Beijing        | Bioinspired colloidal photonic crystals development. <sup>89, 90</sup>                                                  |
| The Ozin Group        | University of Toronto                      | Opal-patterned chips by using colloidal crystal assembly in silicon wafers. <sup>91</sup>                               |

## 1.1 LIGHT DIFFRACTION FROM PHOTONIC CRYSTALS

### 1.1.1 Bragg's Law

The diffracted light from photonic crystals closely follows Bragg's law.<sup>92, 93</sup> As shown in Fig. 1.1, the incident waves are reflected specularly from parallel planes spaced a distance  $d$  apart. The path difference between adjacent planes is  $2d\sin\theta$ , where  $\theta$  is the glancing angle. The diffracted beam occurs when the scatterings from parallel planes of atoms or colloidal particles interfere constructively. This occurs when the path differences are an integral number  $m$  of wavelengths  $\lambda$ , as shown in eqn. 1-1:<sup>92, 93</sup>

$$2d\sin\theta = m\lambda \quad (1-1)$$

# Incident Light

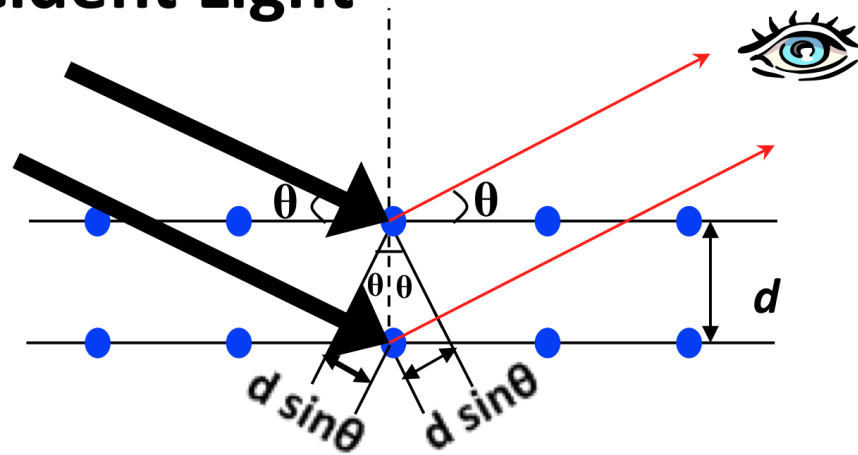
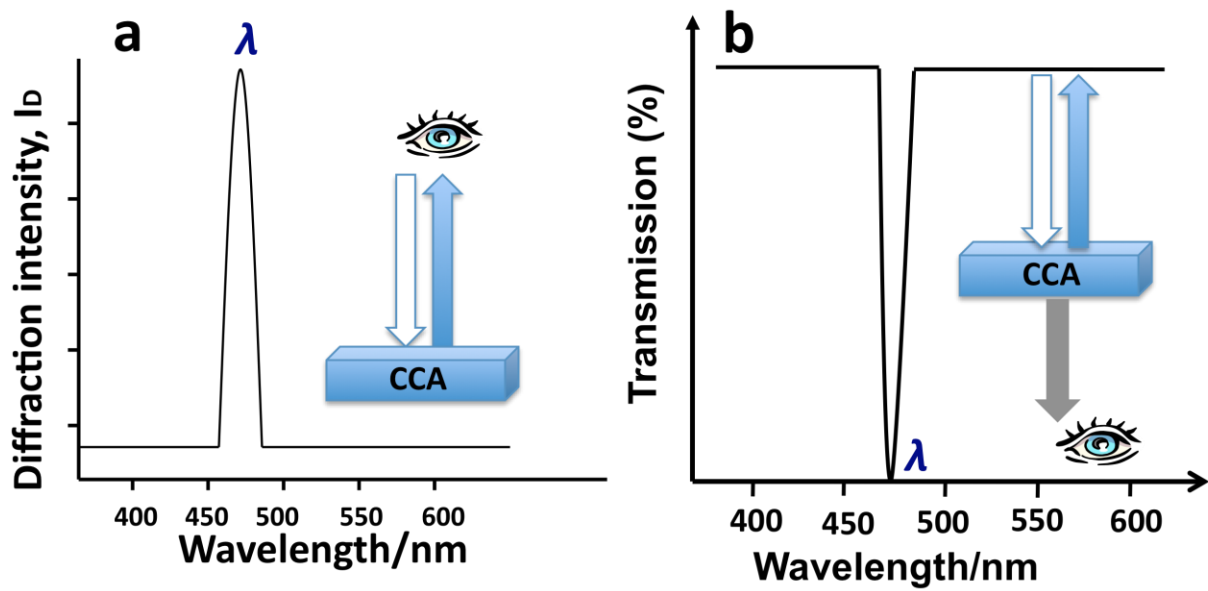


Figure 1.1 Derivation of Bragg's law.

### **1.1.2 Experimental Measurements of Photonic Crystal Light Diffraction**

The light diffraction from the photonic crystals can be measured either by reflectance or transmission. For the reflectance, fiber optics (Ocean optics, Inc.) are used to measure the diffracted beam intensity as shown in Fig. 1.2 a. The fiber probe is a six-around-one probe that produces excitation with white light from a closely surrounding set of six fibers and collects the back-diffracted light with a center fiber. For transmission, we use a UV-Vis spectrophotometer (Cary 5000, Varian, Inc.) to measure the intensity of the transmitted beam in the photonic crystal light diffraction process as shown in Fig. 1.2 b. A narrow and sharp diffraction peak will be observed in both cases if the photonic crystal is highly ordered and shows little absorption of light.<sup>55, 93</sup>



**Figure 1.2** (a) Reflectance and (b) transmission measurements of photonic crystal light diffraction.

## 1.2 CCA PARTICLE SYNTHESIS AND SELF-ASSEMBLY

In 1969, Krieger et al.<sup>94, 95</sup> found that highly charged monodisperse colloidal particles with covalently attached ionizing groups would self-assemble into highly ordered, non-close-packed three-dimensional arrays, now known as CCA. This self-assembly minimizes the total interparticle electrostatic repulsive energy of the system by forming either a body-centered cubic (BCC) or face-centered cubic (FCC) structure (Fig. 1.3).<sup>93, 94, 96-98</sup> The CCA orient with their highest particle density lattice planes (BCC (110) or FCC (111) planes) parallel to the container walls.<sup>63, 99, 100</sup>

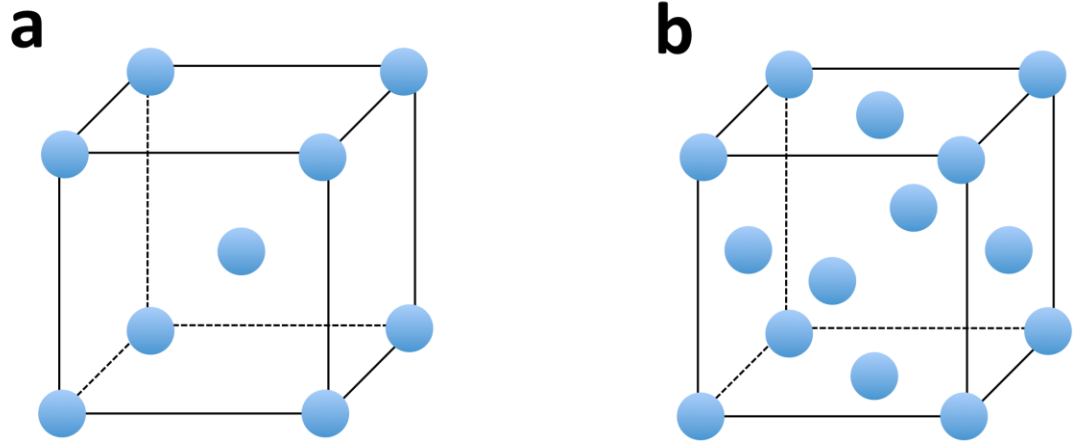


**Figure 1.3** (a) BCC and (b) FCC structures.

$$U(r) = \frac{Z^2 e^2}{\varepsilon} \left[ \frac{e^{\kappa a}}{1 + \kappa a} \right]^2 \frac{e^{-\kappa r}}{r} \quad (1-2)$$

$$\kappa^{-1} = \left[ \frac{4\pi e^2 (n_p Z + n_i)}{\varepsilon k_B T} \right]^{-1/2} \quad (1-3)$$

The potential energy of interaction between colloidal particles can be described by Dejaurin, Landau, Verwey and Overbeek (DLVO) theory that combines the effects of the electrostatic repulsion and the van der Waals forces.<sup>101-104</sup> Since the CCA particles have high surface charge, the major interparticle interactions in the CCA dispersion are caused by a screened Coulomb repulsive potential  $U(r)$  described in eqn. 1-2, where  $r$  is the center-to-center distance between the two particles,  $Z$  is the number of charges per particle,  $e$  is the electron charge,  $a$  is the radius of the particle, and  $\varepsilon$  is the dielectric constant of the dispersion medium. The Debye-Hückel screening length  $\kappa^{-1}$  is defined in eqn. 1-3, where  $k_B$  is Boltzmann constant,  $T$  is the temperature,  $n_p$  is the particle concentration,  $n_p Z$  is the counter ion concentration, and  $n_i$  is the ionic impurity concentration (assumed to be monovalent).<sup>105</sup>

The electrostatic repulsive force decreases strongly with increasing concentration of ionic impurities due to the screening effect caused by the counter ions in the double layers (eqns. 1-2 and 1-3).<sup>102, 106, 107</sup> To form a CCA, highly charged monodisperse colloidal dispersion needs to be exhaustively cleaned through dialysis (or centrifugation/redispersion) and ion-exchange resin (Fig. 1.4) to remove the ionic impurities.<sup>51-63</sup>

For low ionic strengths ( $<10^{-5}$  M), the electrostatic repulsive interactions occur over distances many times larger than the particle diameter. At low ionic strengths and at sufficient particle concentrations, the highly charged particles will self-assemble into a CCA to minimize the interparticle repulsive interactions.<sup>15, 17</sup>

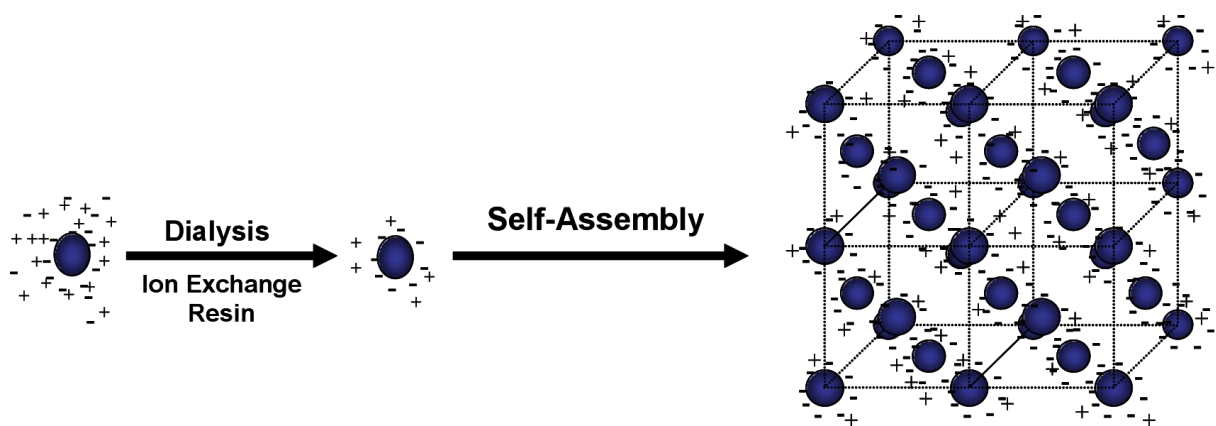


**Figure 1.4** Highly charged monodisperse polystyrene particles self-assemble into a CCA (*from Asher, S. A.; Holtz, J.; Liu, L.; Wu, Z. J., J. Am. Chem. Soc. 1994, 116, 4997*).

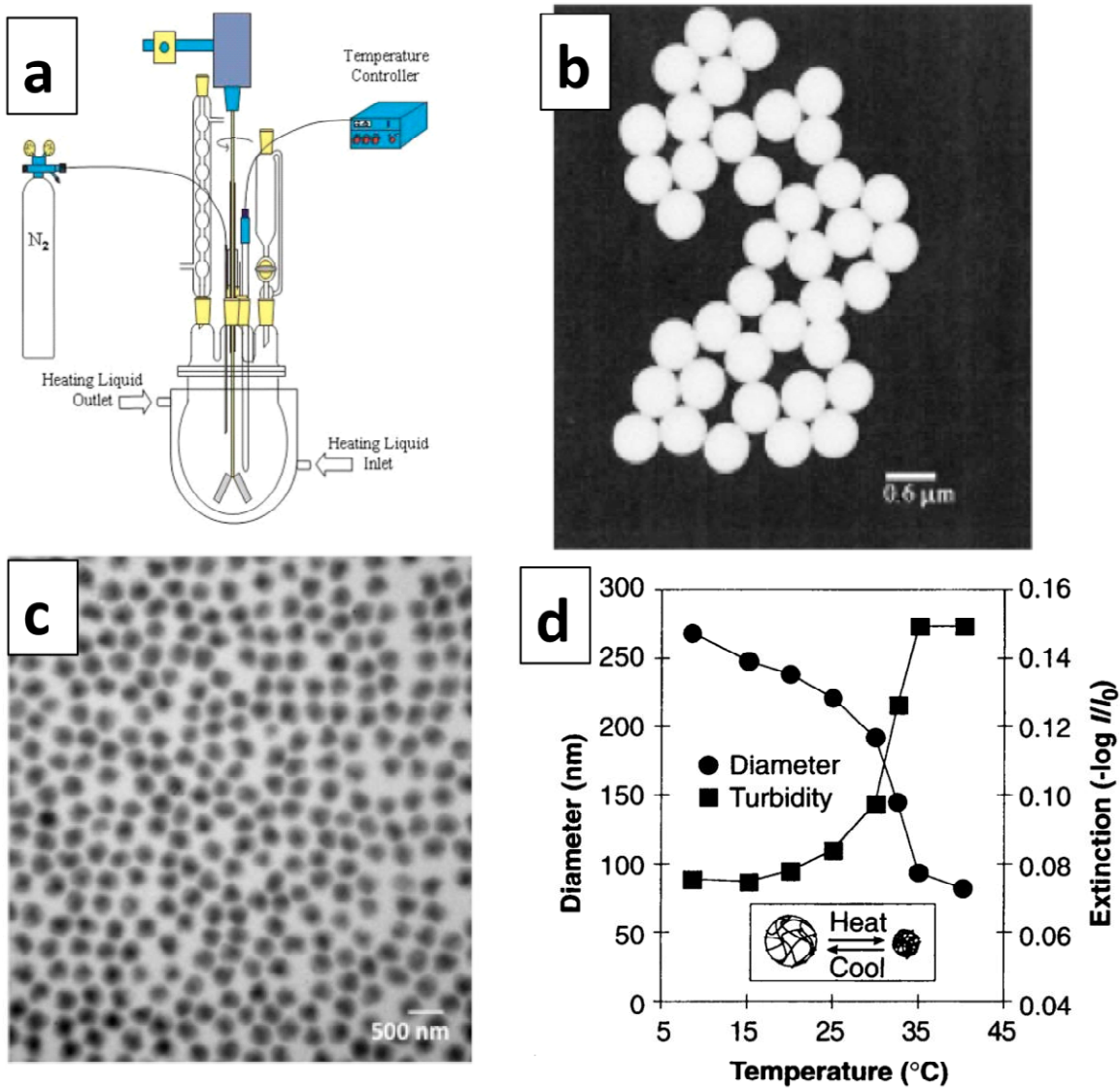


**Figure 1.5** (a) A typical setup for synthesis of polymeric particles (from Asher's group website); (b) A TEM image of PS particles with a diameter of 565 nm (from Reese, C. E.; Asher, S. A. *J. Colloid interface Sci.* 2002, 248, 41.); (c) A TEM image of PNIPAm particles with a diameter of ~300 nm (from Wang, L.; Asher, S. A. *Chem. Mater.* 2009, 21, 4608.); (d) Dependences of PNIPAm colloid diameter and turbidity on temperature (from Weissman, J. M.; Sunkara H. B.; Tse, A. S.; Asher, S. A. *Science* 1996, 274, 959.).

The CCA particles can be polymeric, inorganic, or hybrid particles which are monodisperse and highly charged.<sup>21, 42, 43, 51, 53, 54, 56-63</sup> Below we discuss general methods for preparing monodisperse CCA particles.

### 1.2.1 Synthesis of Polymeric CCA Particles

Polymeric CCA particles are usually synthesized by emulsion or dispersion polymerization.<sup>21, 42, 43, 58-60</sup> A typical setup for the synthesis is shown in Fig. 1.5a where a N<sub>2</sub> blanket is maintained to exclude oxygen and the temperature is usually kept at 70 °C during the polymerization. *N, N'*-methylene-*bis*-acrylamide is often used as a cross linker. Potassium persulfate or ammonium persulfate is used as the initiator. A surfactant (i.e. sodium dodecyl sulfate, SDS) is added to stabilize the particle dispersion and to control the particle size. An ionic comonomer (i.e. 2-acrylamido-2-methyl-1-propanesulfonic acid) is copolymerized to add surface charges to the polymeric particles. The reaction is rapidly stirred (i.e. 350 rpm) and refluxed for ~ 6 hrs.

Polystyrene (PS) particles are widely used for CCA fabrication because of their low cost and easy fabrication. Reese et al. synthesized highly charged monodisperse PS particles with diameters from 100 nm to 1 μm.<sup>42, 43</sup> Fig. 1.5b shows a transmission electron microscopy (TEM) image of PS particles with an average diameter of 565 nm.<sup>43</sup>

Poly(*N*-isopropylacrylamide) (PNIPAm) particles are well-known for their temperature-sensitive properties.<sup>20, 21, 53</sup> They have a lower critical solution temperature (LCST) around 32 °C. When temperature is lower than the LCST, the PNIPAm particles are hydrated and swollen. They undergo a reversible volume phase transition to a collapsed, dehydrated state when heated above the LCST. Fig. 1.5c shows a TEM image of PNIPAm particles with an average diameter

of ~300 nm.<sup>53</sup> Fig. 1.5d shows the dependences of the PNIPAm particle diameter and turbidity on temperature.<sup>20</sup>

### 1.2.2 Synthesis of Inorganic CCA Particles

Highly charged monodisperse inorganic particles have also been used for CCA fabrications.<sup>51, 56, 63</sup> Among these colloidal particles, silica particles are of great interest because of their low toxicity and facile fabrication.<sup>108</sup> In addition, for PCCA applications, the embedded silica CCA particles can be easily etched out by using HF acid to form hollow PCCA.<sup>109, 110</sup>

The Stöber method is a simple way to synthesize silica particles.<sup>111</sup> A typical recipe uses an alkyl silane (i.e. tetraethoxysilane, TEOS) as the precursor, ethanol/water as the reaction solvent, and ammonia as the catalyst.<sup>111</sup> The silica particle size is controlled by the amounts of silane precursor or ammonia in the reaction. In order to form CCA, the Stöber silica particles need to be functionalized with the charged groups because the  $pK_a$  of the surface  $-SiOH$  is relatively high (~7.1); the  $-SiOH$  groups do not provide enough charge for the silica CCA self-assembly.<sup>63, 112</sup> In Chapter 2, we describe a facile method to synthesize highly charged, monodisperse silica particles.

### 1.2.3 Synthesis of Hybrid Particles

Hybrid particles provide extra functionality (i.e. shell length/composition, core-shell ratio) for CCA fabrication. Xu et al. synthesized silica/PS core-shell particles and furthered fabricated hollow PS particles by etching out the silica cores with HF acid.<sup>54</sup> Chang et al. used a water-in-oil microemulsion method to prepare monodisperse silica-cadmium sulfide (CdS) nanocomposite

spheres.<sup>61</sup> Chang et al. further processed these nanocomposite spheres to form complex voids within the silica colloids by quantitatively etching out the CdS inclusions with concentrated nitric acid.<sup>62</sup> Wang et al. fabricated nanocomposite monodisperse silica spheres containing homogeneously dispersed Ag quantum dots through the photochemical reduction of silver ions during the synthesis of silica particles.<sup>113</sup> In Chapter 5, we describe a novel method to synthesize monodisperse PNIPAm-core/silica-shell particles.<sup>53</sup>

## 1.3 CCA APPLICATIONS

### 1.3.1 CCA Optical Filters

The light diffraction of a highly ordered CCA can be very efficient and therefore CCA can be used as optical filters to reject specific wavelengths while passing adjacent spectral regions.<sup>15-18</sup> According to Bragg's Law (eqn. 1-1), the diffracted wavelength ( $\lambda$ ) can be easily tuned by tilting the CCA orientation ( $\theta$ ) relative to the incident light. Larger diffracted wavelength changes can be achieved by changing the CCA concentrations to vary the particle array spacing  $d$ . Fig. 1.6a shows the orientation of a CCA filter to the incident light.<sup>16</sup> Fig. 1.6b shows transmission spectra of the CCA filter at incident angles of  $90^\circ$  and  $80^\circ$  giving diffracted wavelengths of 497 nm and 493 nm, respectively.<sup>16</sup> In Chapter 2, we describe a silica CCA deep UV filter and its utilization as a Rayleigh rejection filter for Teflon UV Raman measurements.

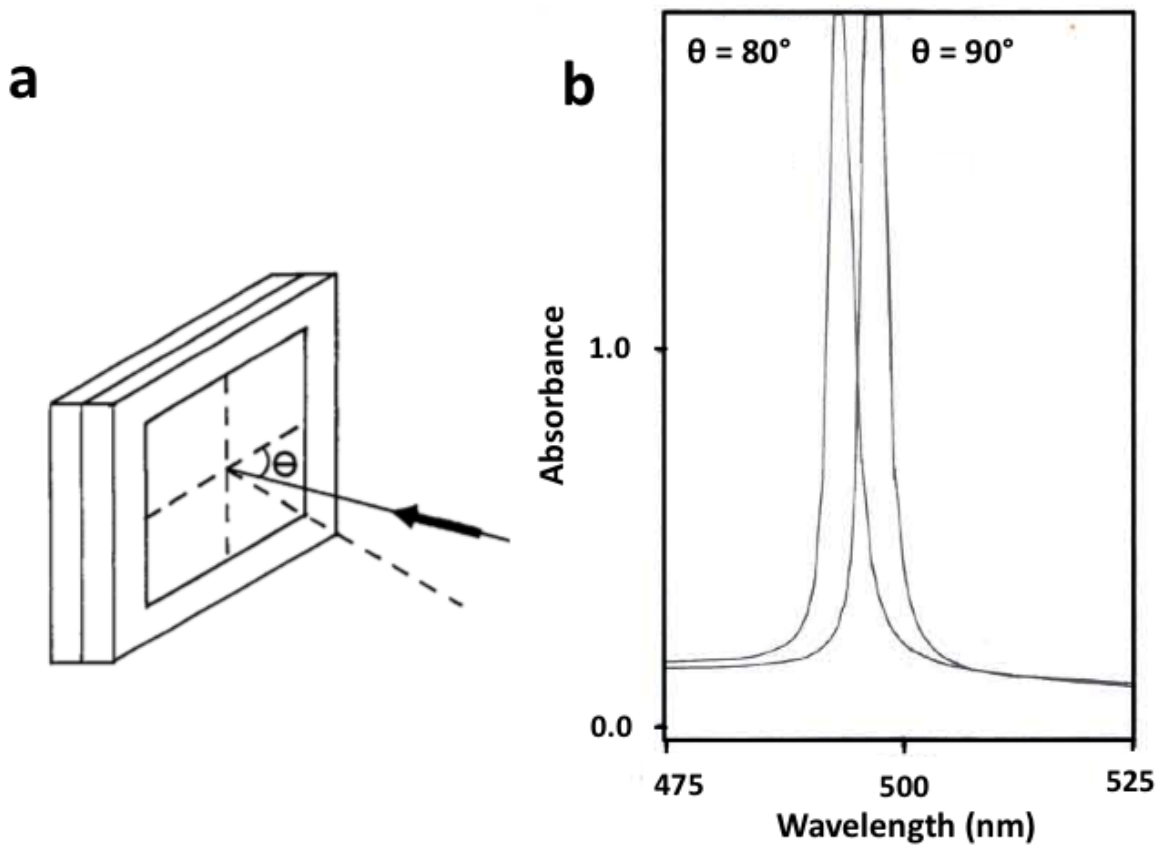


**Figure 1.6** (a) The orientation of a CCA filter to the incident light beam; (b) Spectra showing transmission through the CCA filter at an incident glancing angle of  $90^\circ$  and  $80^\circ$  (from Asher S. A.; Flaugh, P. L.; Washinger, G. *Spectroscopy* 1986, 1, 26.).

### 1.3.2 CCA Sensing Materials

CCA has been polymerized within hydrogels to form PCCA in which the hydrogels are functionalized with recognition groups so that the hydrogels swell or shrink in response to the targeted analytes.<sup>23-26, 64-73</sup> The hydrogel volume changes will vary the CCA particle spacings resulting in visually evident color changes or detectable wavelength shifts.<sup>23-26, 64-73</sup> Fig. 1.7 shows PCCA sensing materials consisting of an embedded CCA in a hydrogel network functionalized with a molecular recognition element.<sup>25</sup> The diffracted wavelength red shifts due to the hydrogel volume increase induced by the interaction of the analyte with the molecular recognition species in the hydrogel.<sup>25</sup> The PCCA sensing motif has been developed for  $\text{Pb}^{2+}$ ,<sup>26, 65, 71, 73</sup>  $\text{Ba}^{2+}$ ,<sup>26</sup>  $\text{K}^+$ ,<sup>26</sup>  $\text{Cu}^{2+}$ ,<sup>67, 70</sup>  $\text{Ni}^{2+}$ ,<sup>70</sup> pH,<sup>24, 66, 69, 71, 73</sup> ionic strength,<sup>24, 66</sup> temperature,<sup>66</sup> glucose,<sup>25, 65, 72</sup> creatinine,<sup>68</sup> and ethanol<sup>69</sup> detection.

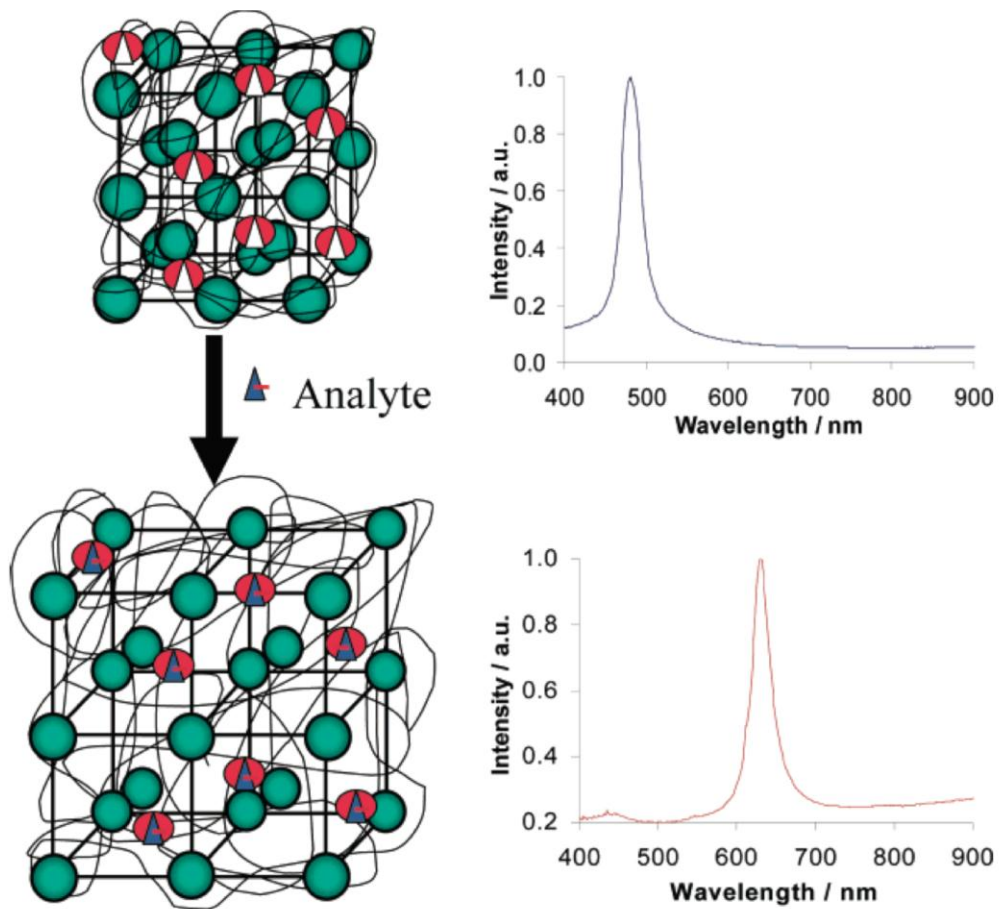


**Figure 1.7** PCCA photonic crystal sensing materials consist of an embedded CCA in a hydrogel network functionalized with a molecular recognition element. The diffracted wavelength red shifts result from the hydrogel volume increase induced by the interaction of the analyte with the molecular recognition element in the hydrogel (from Asher, S. A. et al. *J. Am. Chem. Soc.* 2003, 125, 3322.).

### 1.3.3 Other CCA applications

CCA consisting of ordered, monodisperse particles can be used as templates to fabricate inverted photonic crystals or other nanostructures. Liu et al. fabricated a PCCA of water voids (HPCCA) by using silica PCCA as a template and then etching out the silica particles in the PCCA (Fig. 1.8).<sup>109, 110</sup> They used the HPCCA to study macromolecule diffusion in a swollen polymeric gel matrix and gave the first direct experimental evidence for the entropic trapping phenomena of polymers in swollen polymeric gel media.<sup>109, 110</sup> Bohn et al. fabricated non-close-packed highly ordered direct and inverse opal silica photonic crystals using PS PCCA as templates.<sup>52</sup> In Chapter 3, we show a photonic crystal template method to fabricate stoichiometrically complex nanoparticles for UV Raman solid cross section determinations. In Chapter 5, we describe a method to fabricate silica shell photonic crystals through flexible PNIPAm core templates.

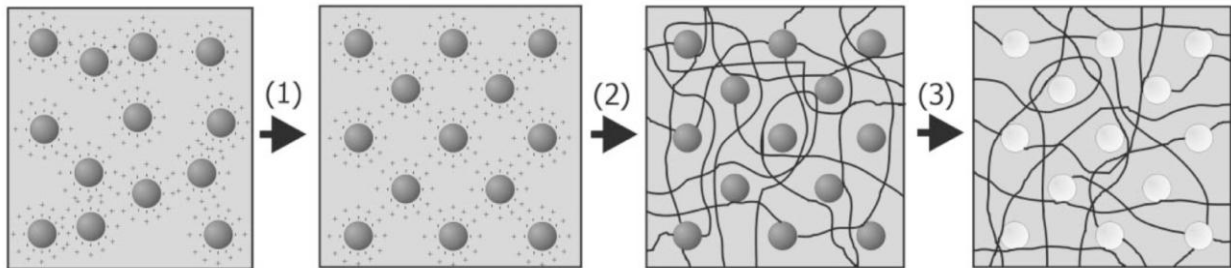


**Figure 1.8** Fabrication of a PCCA of water voids. (1) Monodisperse silica particles self-assemble into a CCA; (2) The silica CCA is immobilized within a polyacrylamide hydrogel network to form a PCCA; (3) Silica particles are etched out with HF acid to result in a PCCA of water voids (*from Liu, L.; Li, P.; Asher, S. A. Nature 1999, 397, 141.*).

## 1.4 OVERVIEW OF RESEARCH PROGRAM

The work reported herein discusses the advancements made in the development of new CCA photonic crystal materials, novel deep UV CCA photonic crystal Bragg diffraction devices and their applications, as well as applications of CCA photonic crystal templates.

Chapter 2 describes a facile method to fabricate photonic crystal CCA deep UV Bragg diffraction devices. The CCA were prepared through the self-assembly of small, monodisperse, highly surface charged silica particles (~50 nm diameter) that were synthesized by using a modified Stöber process. The particle surfaces were charged by functionalizing them with the strong acid, non UV absorbing silane coupling agent. These highly charged, monodisperse silica particles self-assemble into CCA that efficiently Bragg diffract light in the deep UV. The diffracted wavelength was varied between 237 nm to 227 nm by tilting the CCA orientation relative to the incident beam between glancing angles from 90° to ~66°. Theoretical calculations predict that the silica CCA diffraction will have a full width at half maximum (FWHM) of 2 nm with a transmission of  $\sim 10^{-11}$  at the band center. We demonstrate the utility of this silica CCA filter to reject the Rayleigh scattering in 229 nm deep UV Raman measurements of highly scattering Teflon.

In Chapter 3, we describe a facile method to fabricate complex stoichiometrically defined nanoparticles by utilizing the defined volume interstices of close-packed photonic crystals. Fabrication of small defined size nanoparticles enables measurements of resonance Raman cross sections of solid materials. We successfully utilized this method to fabricate mixed

NaNO<sub>3</sub>/Na<sub>2</sub>SO<sub>4</sub> nanoparticles with a defined stoichiometry on the surface of the photonic crystal spherical particles. We used these stoichiometrically defined NaNO<sub>3</sub>/Na<sub>2</sub>SO<sub>4</sub> nanoparticles to determine the solid-state UV resonance Raman cross-section of the NO<sub>3</sub><sup>-</sup> ν<sub>1</sub> symmetric stretching band (229 nm excitation wavelength) by monitoring the Raman spectrum of Na<sub>2</sub>SO<sub>4</sub> as an internal standard. These are the first resonance Raman cross-section measurements of solids that avoids the biasing of self-absorption. These NaNO<sub>3</sub>/Na<sub>2</sub>SO<sub>4</sub> nanoparticles appear to show a more facile photolysis than is observed for normal solid NaNO<sub>3</sub> samples.

In Chapter 4, we report a refractive-index matching method to measure nonabsorbing solid-state UV Raman cross sections that avoids the impact of the local field phenomenon and particle interface scattering of incident light. We used refractive-index matched chloroform as an internal intensity standard to determine the solid-state 995 cm<sup>-1</sup> Na<sub>2</sub>SO<sub>4</sub> 244 nm Raman cross sections. The pure liquid chloroform 668 cm<sup>-1</sup> 244 nm Raman cross section was determined by using acetonitrile as an internal standard and by calculating the local field corrections for the observed Raman intensities. Our measured 244 nm UV Raman cross sections of the solid state 995 cm<sup>-1</sup> SO<sub>4</sub><sup>2-</sup> band of  $1.97 \pm 0.07 \times 10^{-28}$  cm<sup>2</sup>/(mol·sr), is about half that of its aqueous solution Raman cross section indicating interactions between the sulfate species in the solid that decrease the Raman polarizability.

Chapter 5 describes a novel method to fabricate silica shell photonic crystals through flexible PNIPAm core templates. Monodisperse PNIPAm flexible core particles were synthesized by dispersion polymerization. Silica particles were attached to the partially swollen PNIPAm particles by the hydrolysis and condensation of tetraethoxysilane at 24 °C. The resulting silica particle-functionalized PNIPAm core particles show reversible swelling and shrinking as the temperature is cycled. These particles form close-packed-array photonic crystals

as the solvent evaporates; the cores shrink to form a silica shell around the pure PNIPAm dry core particles as they close pack. The PNIPAm cores were removed by calcination, leaving a PC composed of essentially pure continuous hollow silica shells. These silica shell photonic crystals Bragg diffract UV light at ~310 nm. The close packed particle interstices are continuous and are easily filled by water. In contrast, the silica shells are impervious to water because the process of making them results in a non-porous continuous shell of silica without holes.

Chapter 6 summarizes each of the projects and suggests opportunities for future studies.

## 1.5 REFERENCES

1. Colvin, V. L. *MRS Bull.* **2001**, 26, 637.
2. Joannopoulos, J. D.; Villeneuve, P. R.; Fan, S. H. *Nature* **1997**, 387, 830.
3. Ge, J. and Yin, Y. *Angew. Chem. Int. Ed.* **2011**, 50, 1492.
4. Xia, Y; Gates, B.; Li Z. *Adv. Mater.* **2001**, 13, 409.
5. Edrington, A. C.; Urbas, A. M.; DeRege, P.; Chen, C. X.; Swager, T. M.; Hadjichristidis, N.; Xenidou, M.; Fetters, L. J.; Joannopoulos, J. D.; Fink, Y.; Thomas, E. L. *Adv. Mater.* **2001**, 13, 421.
6. Norris, D. J.; Vlasov Y. A. *Adv. Mater.* **2001**, 13, 371.
7. López, C. *Adv. Mater.* **2003**, 15, 1679.
8. Lyon, L. A.; Debord, J. D.; Debord, S. B.; Jones, C. D.; McGrath, J. G.; Serpe, M. J. *J. Phys. Chem. B* **2004**, 108, 19099.
9. Sailor, M. J., Link, J. R. *Chem. Commun.* **2005**, 11, 1375.
10. Carlos I. Aguirre, Edilso Reguera, and Andreas Stein, *Adv. Funct. Mater.* **2010**, 20, 2565.
11. Zhang, Y.; Wang, J.; Huang, Y.; Song Y.; Jiang, L. *J. Mater. Chem.* **2011**, 21, 14113.
12. Yablonovitch, E. *Phys. Rev. Lett.* **1987**, 58, 2059.
13. John, S. *Phys. Rev. Lett.* **1987**, 58, 2486.

14. Joannopoulos, J. D.; Johnson, S. G.; Winn, J. N.; Meade, R. D. *Photonic crystals: Molding the Flow of the Light (Second Edition)*; Princeton University: New Jersey, 2008.
15. Rundquist, P. A.; Photinos, P.; Jagannathan, S.; Asher, S. A. *J. Chem. Phys.* **1989**, 91, 4932.
16. Asher S. A.; Flaugh, P. L.; Washinger, G. *Spectroscopy* **1986**, 1, 26.
17. Flaugh, P. L.; O'Donnell, S. E.; Asher, S. A. *Appl. Spectrosc.* **1984**, 38, 847.
18. Asher, S. A. *Crystalline Colloidal Narrow Band Radiation Filter*, U. S. Patent 4,632,517, Dec. 30, 1986
19. Maurer, M. K., *Nanotechnology for Telecommunications chapter 8*, CRC Press, 2010, p. 179.
20. Weissman, J. M.; Sunkara., H. B.; Tse, A. S.; Asher, S. A. *Science* **1996**, 274, 959.
21. Reese, C. E.; Mikhonin, A. V.; Kamenjicki, M.; Tikhonov, A.; Asher, S. A. *J. Am. Chem. Soc.* **2004**, 126, 1493.
22. Pan, G.; Kesavamoorthy, R.; Asher, S. A. *J. Am. Chem. Soc.* **1998**, 120, 6525.
23. Lee, M.; Fauchet, P. M., *Optics Express* **2007**, 15, 4530.
24. Lee, K.; Asher, S. A., *J. Am. Chem. Soc.* **2000**, 122, 9534.
25. Asher, S. A.; Alexeev, V. L.; Goponenko, A. V.; Sharma, A. C.; Lednev, I. K.; Wilcox, C. S.; Finegold, D. N. *J. Am. Chem. Soc.* **2003**, 125, 3322.
26. Holtz J. H.; Asher, S. A. *Nature* **1997**, 389, 829.
27. Aguirre, C. I.; Reguera, E.; Stein, A., *Applied Materials & Interfaces* **2010**, 2, 3257.
28. Singh, K. B.; Tirumkudulu, M. S. *Phys. Rev. Lett.* **2007**, 98, 218302.
29. McGrath, J. G.; Bock, R. D.; Cathcart, J. M.; Lyon, L. A. *Chem. Mater.* **2007**, 19, 1584.
30. Noda, S.; Fujita, M.; Asano, T. *Nature Photonics* **2007**, 1, 449.

31. Lončar, M.; Yoshie, T.; Scherer, A. *Appl. Phys. Lett.* **2002**, 81, 2680.
32. Wu, X.; Yamilov, A.; Liu, X.; Li, S.; Dravid, V. P.; Chang, R. P. H.; Cao, H. *Appl. Phys. Lett.* **2004**, 85, 3657.
33. Won, R. *Nature Photonics* **2009**, 3, 498 - 499.
34. Mortensen, N. A.; Xiao, S.; Pedersen, J. *Microfluid Nanofluid* **2008**, 4, 117.
35. Li, J.; Heman, P.; Valdivia, C.; Kitaev, V.; Ozin, G. *Optics Express* **2005**, 13, 6454.
36. Buczynski, R. *Acta Physica Polonica A* **2004**, 106, 141.
37. Kazmierczak, T.; Song, H.; Hiltner, A.; Baer, E. *Macromol. Rapid Commun.* **2007**, 28, 2210.
38. Hawkeye, M. M.; Joseph, R.; Sit, J. C.; Brett, M. J. *Optics Express* **2010**, 18, 13220.
39. Cheng, C. C.; Scherer, A.; Tyan, R.; Fainman, Y.; Witzgall G.; Yablonovitch, E. *J. Vac. Sci. Technol. B* **1997**, 15, 2764.
40. Campbell, M.; Sharp, D. N.; Harrison, M. T., Denning, R. G.; Turberfield, A. J. *Nature* **2000**, 404, 53.
41. Cheng, C. C.; Scherer, A. *J. Vac. Sci. Technol. B* **1995**, 13, 2696.
42. Reese, C. E.; Guerrero, C. D.; Weissman, J. M.; Lee, K.; Asher, S. A. *J. Colloid Interface Sci.* **2000**, 232, 76.
43. Reese, C. E.; Asher, S. A. *J. Colloid Interface Sci.* **2002**, 248, 41.
44. Im, S. H.; Lim, Y. T.; Suh, D. J.; Park, O. O. *Adv. Mater.* **2002**, 14, 1367.
45. Noda, S.; Tomoda, K.; Yamamoto, N.; Chutinan, A. *Science* **2000**, 289, 604.
46. Ozbay, E. *J. Opt. Soc. Am. B* **1996**, 13, 1945.
47. Rill, M. S.; Plet, C.; Thiel, M.; Staude, I.; Freymann, G. V.; Linden, S.; Wegener, M. *Nature Materials* **2008**, 7, 543.

48. Míguez, H.; Chomski, E.; García-Santamaría, F.; Ibisate, M.; John, S.; López, C.; Meseguer, F.; Mondia, J. P.; Ozin, G. A.; Toader, O.; van Driel, H. M. *Adv. Mater.* **2001**, 13, 1634.
49. Link, J. R.; Sailor, M. J. *Proc. Natl. Acad. Sci. USA.* **2003**, 100, 10607.
50. Trifonov, T.; Marsall, L. F.; Rodríguez, A.; Pallarès, J.; Alcubilla, R. *Physica Status Solidi C* **2005**, 2, 3104.
51. Luo, J.; Qu, D.; Tikhonov, A.; Bohn, J.; Asher, S. A. *J. Colloid Interface Sci.* **2010**, 345, 131.
52. Bohn, J. J.; Ben-Moshe, M.; Tikhonov, A.; Qu, D.; Lamont, D. N.; Asher, S. A. *J. Colloid Interface Sci* **2010**, 344, 298.
53. Wang L.; Asher, S. A. *Chem. Mater.* **2009**, 21, 4608.
54. Xu, X.; Asher, S. A. *J. Am. Chem. Soc.* **2004**, 126, 7940.
55. Asher, S. A.; Weissman, J. M.; Tikhonov, A.; Coalson, R. D.; Kesavamoorthy, R. *Phys. Rev. E* **2004**, 69, 066619.
56. Xu, X.; Friedman, G.; Humfeld, K.; Majetich, S.; Asher, S. A. *Adv. Mater.* **2001**, 13, 1681.
57. Wang, W.; Asher, S. A. *J. Am. Chem. Soc.* **2001**, 123, 12528.
58. Asher, S. A.; Pan, G.; Kesavamoorthy, R. *Nonlinear Optics* **1999**, 21, 343.
59. Pan, G.; Tse, A.S.; Kesavamoorthy, R.; Asher, S. A. *J. Am. Chem. Soc.* **1998**, 120, 6518.
60. Tse, A.; Wu, Z.; Asher, S. A. *Macromolecules* **1995**, 28, 6533.
61. Chang, S.; Liu L.; Asher S. A. *J. Am. Chem. Soc.* **1994**, 116, 6739.
62. Chang, S.; Liu L.; Asher S. A. *J. Am. Chem. Soc.* **1994**, 116, 6745.
63. Kesavamoorthy, R.; Tandon, S.; Xu, S.; Jagannathan, S.; Asher, S. A. *J. Colloid Interface Sci.* **1992**, 153, 188.
64. Asher, S. A.; Holtz, J.; Liu, L.; Wu, Z. *J. Am. Chem. Soc.* **1994**, 116, 4997.

65. Holtz, J. H.; Holtz, J. S. W.; Munro, C. H.; Asher, S. A. *Anal. Chem.* **1998**, 70, 780.
66. Reese, C. E.; Baltusavich, M. E.; Keim, J. P.; Asher, S. A. *Anal. Chem.* **2001**, 73, 5038.
67. Asher, S. A.; Sharma, A. C.; Goponenko, A. V.; Ward, M. M. *Anal. Chem.* **2003**, 75, 1676.
68. Sharma, A.; Jana, T.; Kesavamoorthy, R.; Shi, L.; Virji, M.; Finegold D.; Asher, S. A. *J. Am. Chem. Soc.* **2004**, 126, 2971.
69. Xu, X.; Goponenko A. V.; Asher, S. A. *J. Am. Chem. Soc.* **2008**, 130, 3113.
70. Baca, J. T.; Finegold D. N.; Asher, S. A. *Analyst* **2008**, 133, 385.
71. Muscatello, M. M. W.; Asher, S. A. *Adv. Funct. Mater.* **2008**, 18, 1186.
72. Muscatello, M. M. W.; Stunja, L. E.; Asher, S. A. *Anal. Chem.* **2009**, 81, 4978.
73. Zhang, J.; Wang, L.; Luo, J.; Tikhonov, A.; Kornienko, N.; Asher, S. A. *J. Am. Chem. Soc.* **2011**, 133, 9152.
74. Zhang, J.; Wang, L.; Chao, X.; Asher, S. A. *Langmuir* **2011** (accepted).
75. King, B. H.; Ruminski, A. M.; Snyder, J. L.; Sailor, M. J., *Adv. Mater.* **2007**, 19, 4530.
76. Kelly, T. L.; Gao, T.; Sailor, M. J. *Adv. Mater.* **2011**, 23, 1776.
77. Norris, D. J.; Arlinghaus, E. G.; Meng, L.; Heiny, R.; Scriven, L. E. *Adv. Mater.* **2004**, 16, 1393.
78. Aguirre, C. I.; Reguera, E.; Stein, A. *Adv. Funct. Mater.* **2010**, 20, 2565.
79. Fierke, M.A.; Lai, C. Z.; Buhlmann, P.; Stein, A. *Anal. Chem.* **2010**, 82, 680.
80. Mihi, A.; Zhang, C.; Braun, P. V. *Angew. Chem. Int. Ed.* **2011**, 50, 5712.
81. Nelson, E. C.; Dias, N.; Bassett, K.; Dunham, S.; Verma, V.; Miyake, M.; Wiltzius, P., Rogers, J.; Coleman, J.; Li, X.; Braun, P. V. *Nature Materials* **2011**, 10, 676.

82. Lidstone, E. A.; Chaudhery, V.; Kohl, A.; Chan, V.; Jensen, T. W.; Schook, L. B.; Bashir, R.; Cunningham, B. T. *Analyst* **2011**, 136, 3608.
83. Jiang, P.; Sun, C. H.; Linn, N. C.; Ho, B.; Venkatesh, S. *Current Nanoscience* **2007**, 3, 396.
84. Sun, C. H.; Jiang, P. *Nature Photonics* **2008**, 2, 9.
85. Jorgensen, M. R.; Bartl, M. H. *J. Mater. Chem.* **2011**, 21, 10583.
86. Yan, Q.; Wang, L.; Zhao, X. S. *Adv. Funct. Mater.* **2007**, 17, 3695.
87. Zhao, Y. J.; Zhao, X. W.; Hu, J.; Li, J.; Xu, W. Y.; Gu, Z. Z. *Angew. Chem. Int. Ed.* **2009**, 48, 7350.
88. Zhao, Y. J.; Zhao, X. W.; Hu, J.; Zhu, C.; Xu, H.; Sun, L. G.; Gu, Z. Z. *Adv. Mater.* **2009**, 21, 569.
89. Wang, J.; Zhang, Y.; Wang, S.; Song, Y.; Jiang, L. *Acc. Chem. Res.* **2011**, 44, 405.
90. Zhang, Y.; Wang, J.; Huang, Y.; Song Y.; Jiang, L. *J. Mater. Chem.* **2011**, 21, 14113.
91. Chomski E.; Ozin, G. A. *Adv. Mater.* **2000**, 12, 1071.
92. Kittel, C. *Introduction to Solid State Physics. (Seventh Edition)*; 1996, p. 29.
93. Rundquist, P. A.; Photinos, P.; Jagannathan, S.; Asher, S. A., *J. Chem. Phys.* **1989**, 91, 4932.
94. Hiltner, P. A.; Krieger, I. M. *J. Phys. Chem.* **1969**, 73, 2386.
95. Hiltner, P. A.; Papir, Y. S.; Krieger, I. M. *J. Phys. Chem.* **1971**, 75, 1881.
96. Luck, W.; Klier, M.; Wesslau, H. *Phys. Chem.* **1963**, 67, 75.
97. Luck, W.; Klier, M.; Wesslau, H. *Phys. Chem.* **1963**, 67, 84.
98. Carlson, R. J.; Asher, S. A. *Appl. Spectrosc.* **1984**, 38, 297.

99. Davis, K. E.; Russel, W. B.; Glantschnig, W. J. *Science* **1989**, 245, 507.
100. Monovoukas, Y.; Gast, A. P. *Langmuir* **1991**, 7, 460.
101. Behrens, S. H.; Christl, D. I.; Emmerzael, R.; Schurtenberger, P.; Borkovec, M. *Langmuir* **2000**, 16, 2566.
102. Croker, J. C.; Grier, D. G. *Phys. Rev. Lett.* **1994**, 73, 352.
103. Xia, Y. N.; Gates, B.; Yin, Y. D.; Lu, Y. *Adv. Mater.* **2000**, 12, 693.
104. Parfitt, G. D. *Dispersion of Powders in Liquids with Special Reference to Pigments*; Applied Science: London, 1981, p.1.
105. Zahorchak, J. C.; Kesavamoorthy, R.; Coalson, R. D.; Asher, S. A. *J. Chem. Phys.* **1992**, 96, 6873.
106. Kepler, G. M.; Fraden, S. *Phys. Rev. Lett.* **1994**, 73, 356.
107. Crocker, J. C.; Grier, D. G. *Phys. Rev. Lett.* **1996**, 77, 1897.
108. Beck, C.; Hartl, W.; Hempelmann, R. *Angew. chem. Int. Ed.* **1999**, 38, 1297.
109. Liu, L.; Li, P.; Asher, S. A. *Nature* **1999**, 397, 141.
110. Liu, L.; Li, P.; Asher, S. A. *J. Am. Chem. Soc.* **1999**, 121, 4040.
111. Stöber, W.; Fink, A. *J. Colloid Interface Sci.* **1968**, 26, 62.
112. Hair, M. L.; Hertl, W. *J. Phys. Chem.* **1970**, 74, 91.
113. Wang, W.; Asher, S. A. *J. Am. Chem. Soc.* **2001**, 123, 12528.

## 2.0 SILICA CRYSTALLINE COLLOIDAL ARRAY DEEP UV NARROW BAND DIFFRACTION DEVICES

(This chapter was submitted to the *Applied Spectroscopy*. The coauthors are Luling Wang, Alexander Tikhonov, and Sanford A. Asher.)

We developed a facile method to fabricate deep UV photonic crystal crystalline colloidal array (CCA) Bragg diffraction devices. The CCA were prepared through the self-assembly of small, monodisperse, highly surface charged silica particles (~50 nm diameter) that were synthesized by using a modified Stöber process. The particle surfaces were charged by functionalizing them with the strong acid, non UV absorbing silane coupling agent 3-(trihydroxysilyl)-1-propane-sulfonic acid (THOPS). These highly charged, monodisperse silica particles self-assemble into a face centered cubic CCA that efficiently Bragg diffracts light in the deep UV. The diffracted wavelength was varied between 237 nm to 227 nm by tilting the CCA orientation relative to the incident beam between glancing angles from 90° to ~66°. Theoretical calculations predict that the silica CCA diffraction will have a full width at half maximum (FWHM) of 2 nm with a transmission of  $\sim 10^{-11}$  at the band center. We demonstrate the utility of this silica CCA filter to reject the Rayleigh scattering in 229 nm deep UV Raman measurements of highly scattering Teflon.

## 2.1 INTRODUCTION

The development of novel wavelength-selective optical devices enables major advances in spectroscopic methodologies and instrumentation.<sup>1-16</sup> Spectroscopies such as Raman, fluorescence, hyperspectral imaging, and pump-probe techniques require wavelength-selective optical elements that reject particular regions of the electromagnetic spectrum while transmitting adjacent spectral regions.<sup>5-8, 10, 11, 17</sup> The recent development of highly efficient holographic filters and multilayer dielectric filters have dramatically advanced near UV, visible and near IR spectroscopies.<sup>9-12, 18-21</sup> Unfortunately, analogous devices do not exist in the deep UV because the typical materials used absorb deep UV light.<sup>9, 22, 23</sup> Thus, the important new field of deep UV Raman spectroscopy has not benefited from these instrumentation advances.

In the late 1980's we developed the first photonic crystal device.<sup>7, 8, 15, 16</sup> This optical device, that functioned as a Bragg diffraction filter, was fabricated from a crystalline colloidal array (CCA) of ~100 nm diameter highly charged, monodisperse polystyrene particles.<sup>7, 8</sup> These highly charged particles self-assembled into a face centered cubic structure that efficiently Bragg diffracted light from its 111 planes, but freely transmitted light in adjacent spectral regions. This optic functioned as a highly efficient Rayleigh rejection filter for Raman spectral measurements. This device was licensed from the University of Pittsburgh by EG&G Princeton Applied Research and was commercialized. These CCA Rayleigh rejection filters also served as the basis of novel Raman spectrometers.<sup>7, 8, 15, 16</sup> This CCA technology was leapfrogged in the 1990's when holographic filters became readily available.<sup>24-26</sup>

In the work here we describe an analogous photonic crystal device that functions as an efficient Bragg diffraction filter in the deep UV. To accomplish this we developed a method to prepare CCA photonic crystals of silica spheres that efficiently diffract but do not absorb deep UV light.<sup>7, 8, 22, 27, 28</sup> To accomplish this we developed a facile method to fabricate ~50 nm diameter monodisperse highly charged silica particles that self-assemble into CCAs. We also here demonstrate the utility of this highly charged silica CCA as a Rayleigh rejection filter in deep UV Raman measurements.<sup>28</sup>

## 2.2 EXPERIMENTAL SECTION

### 2.2.1 Fabrication of Highly Charged Monodisperse Small Silica Particles

We synthesized monodisperse, small silica particles by using a modified Stöber method<sup>29</sup>. We then functionalized the silica particle surface with a low deep UV absorption silane coupling agent 3-(trihydroxysilyl)-1-propane-sulfonic acid (THOPS, 30% in water, Gelest, Inc.). A typical reaction used 5 mL tetraethoxysilane (TEOS, Fluka, Lot code 133281541207016) as the silica precursor, 8 mL ammonium hydroxide (29.40 wt%, J. T. Baker) as the catalyst, and 200 mL ethanol as the reaction solvent. The reaction mixture was stirred for 24 h. The resulting silica dispersion was filtered through nylon mesh (Small Parts, Inc). 200 mL of water was slowly added to the Stöber silica dispersion under stirring. The mixture was first heated to 50 °C for ~ 30 min, then heated to 80 °C for ~ 1 h. 6 mL of the silane coupling agent THOPS was adjusted to pH ~ 6 with ammonium hydroxide and then added to the silica dispersion. The reaction was refluxed for 6 h at 80 °C.

### 2.2.2 Silica CCA Fabrication and Transmission Measurements

The functionalized silica colloids were cleaned by six repetitions of centrifugation at 12,000 rpm and redispersion of the resulting silica pellet in Nanopure water (Barnstead). The silica particle concentration was adjusted by controlling the amount of water added during the last redispersion. Further purification was achieved by shaking the silica dispersion with mixed bed ion-exchange resin (Bio-Rad AG 501-X8). After purification, these highly charged silica particles self-assemble into CCA at volume concentrations above 1%. The surface charge density of the functionalized silica particles was determined by conductometric titration (712 conductometer, Brinkmann and 794 Basic Titrino, Metrohm) with 0.01 N Standard NaOH solutions (Fisher Scientific Inc.).

The CCA filter cell is shown in Fig. 2.1a. Two fused silica quartz discs (2" dia. x 3/16") were separated by a ~125  $\mu\text{m}$  thick Parafilm spacer and mounted on a rotation stage. The highly charged silica colloidal dispersion (volume percent 7.0 %) was carefully injected into one of the holes in one of the quartz discs to fill the cell, in order to avoid bubbles. The system self-assembled into a CCA. Transmission spectra of the CCA filter with incident glancing angles at 90°, 69° and 66° were measured with a Cary 5000 (Varian, Inc.) spectrophotometer using the double beam mode and zero/baseline correction.

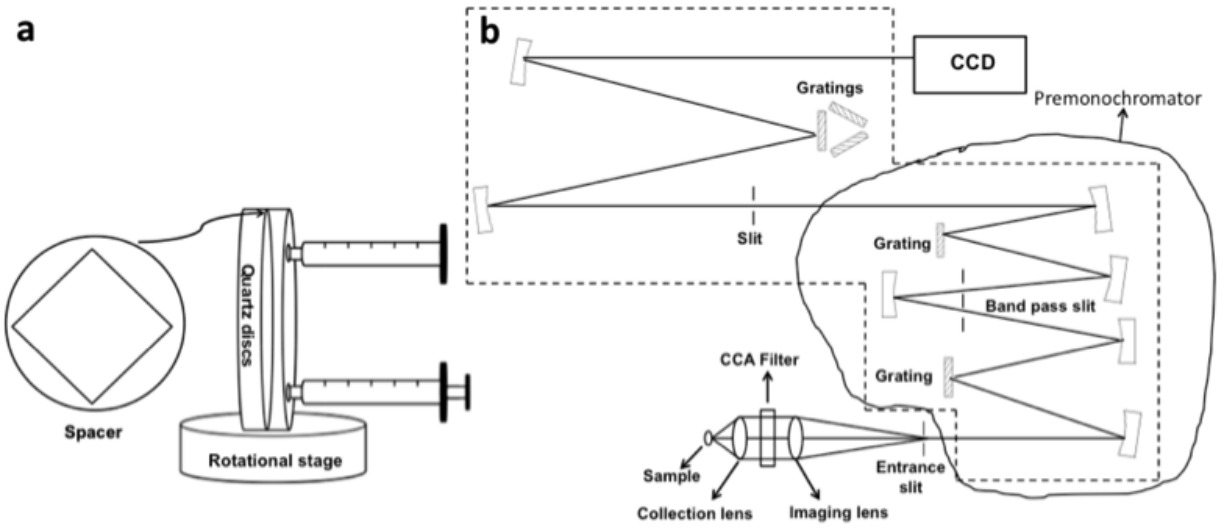


**Figure 2.1** (a) A CCA flow cell for transmission measurements; (b) Schematic of triple-stage monochromator for Raman measurements.

### **2.2.3 Silica CCA Rayleigh Rejection Filter Raman Measurements**

We measured deep UV Raman spectra of highly scattering Teflon with excitation at 229 nm line (2 mW) by using a continuous-wave UV Ar laser (Innova 300 FReD, Coherent Inc.). The laser excited the Teflon sample in a backscattering geometry with the laser beam focused to a ~20  $\mu\text{m}$  diameter spot. Fig. 2.1b shows the schematic of the triplemate monochromator used for the Raman measurements.

The spectrometer filter stage premonochromator was aligned to conveniently block a portion of the Rayleigh scattered light to allow us to make quantitative measurements of the CCA laser light attenuation. The spectrometer setups were identical for Raman spectra measured in the absence and presence of the CCA filter. The CCA filter was placed between a collection and imaging lens (Fig. 2.1b) where the light is collimated.

### **2.2.4 Characterization Techniques**

We measured the silica particle sizes by using dynamic light scattering (DLS) and transmission electron microscopy (TEM). DLS and zeta potential were measured by using a Brookhaven Instruments Corporation ZetaPALS. The silica particles were also examined by using a JEOL 200 CX TEM. A few drops of the dilute silica particle dispersion were dried on a carbon-coated copper grid (Ted Pella, Inc.) for the TEM measurements.

## 2.3 RESULTS AND DISCUSSION

### 2.3.1 Fabrication of Highly Charged, Monodisperse, Small Silica Particles

We used a modified Stöber method to prepare the Stöber silica dispersion where an aqueous ammonium hydroxide solution is used instead of saturated alcoholic solutions of ammonia<sup>29</sup>. The typical recipe yielded Stöber silica particles with a diameter of  $53.6 \pm 0.3$  nm (polydispersity 0.045) as determined by DLS. Fig. 2.2a shows a TEM image of monodisperse silica particles with a diameter of  $43.6 \pm 3.9$  nm. The TEM diameter is smaller than that measured by DLS because DLS measures the hydrodynamic diameter while TEM measures the diameter of the dehydrated particles.

The Stöber silica dispersion after cleaning and ion-exchange does not have sufficient surface charge to self-assemble into CCA; the  $pK_a$  of the surface  $-\text{SiOH}$  is relatively high ( $\sim 7.1$ ).<sup>30</sup> The zeta potential of these cleaned Stöber silica particles is only  $-12$  mV at pH 4.0. We developed a facile method to attach strong sulfonic acid groups ( $-\text{SO}_3\text{H}$ ) to the surface of the monodisperse silica colloids by using THOPS as the silane coupling agent. THOPS was attached to the silica particle surface by a condensation reaction between the silanols ( $-\text{SiOH}$ ) groups on the Stöber silica surface and that of THOPS. The resulting silica particles are highly charged due to the low  $pK_a < 1$  of the surface sulfonic acid groups.<sup>31</sup> Since the Stöber silica dispersion is only stable at basic pH,<sup>32</sup> we found that the silica particles immediately aggregate if we directly added the THOPS solution (pH=0.34) to the Stöber silica dispersion. However, aggregation does not occur if we adjust the THOPS pH to  $\sim 6$  before addition. After cleaning and ion-exchange, the surface functionalized silica particles self-assemble into CCA.

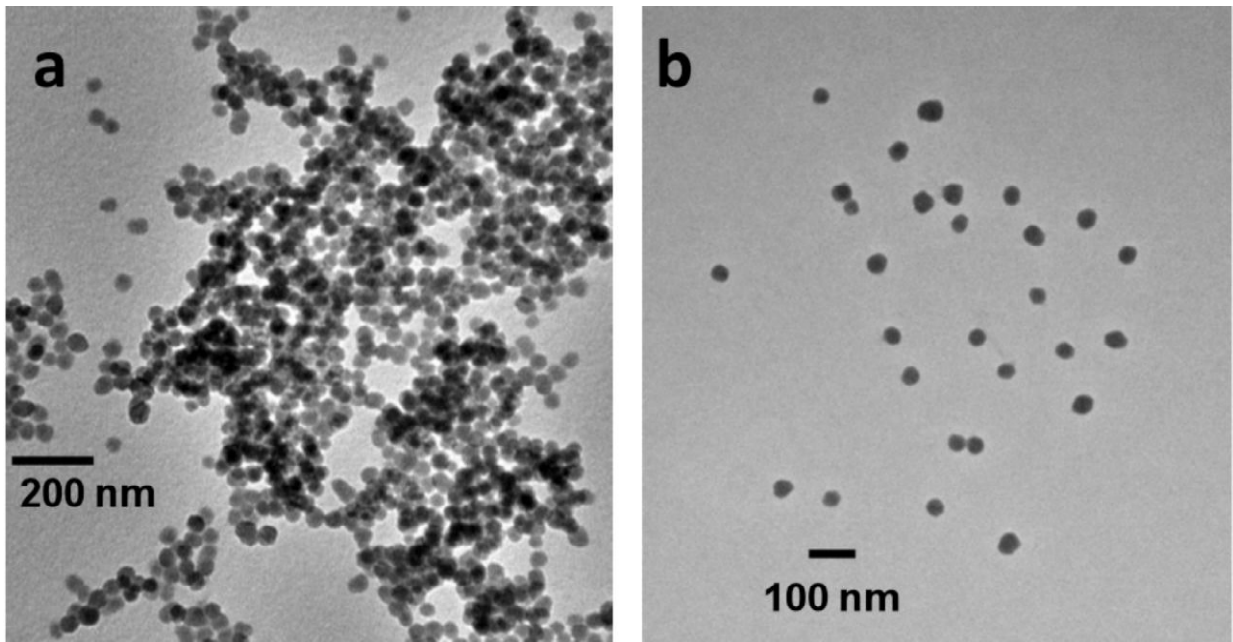


**Figure 2.2** TEM images of (a) the Stöber silica particles; (b) the silica CCA particles.

Fig. 2.2b shows a TEM image of our charged silica CCA particles that show an average diameter of  $47.3 \pm 5.1$  nm. The diameter measured by DLS is  $60.2 \pm 0.3$  nm, slightly larger than that determined by TEM. The zeta potential of the charged silica particles is -43 mV (pH 4.0) which indicates high surface charge. We also determined the surface charges of these silica CCA particles by using conductrometric titration with 0.01 N NaOH. The typical recipe yields 4740 charges per silica particle ( $10.8 \mu\text{C}/\text{cm}^2$ ). Table 2-1 shows that the surface charge density of the silica particles can be easily tuned by varying the amount of THOPS during the surface modification. The zeta potential increases as we increase the amount of THOPS during the surface modification reaction.

**Table 2-1** Dependence of Silica CCA Particle Surface Charge on THOPS\*

| <b>Sample</b> | <b>Diameter/nm<br/>(TEM)</b> | <b>THOPS/mL</b> | <b>Charges per<br/>particle</b> | <b>Charge<br/>Density<br/>(<math>\mu\text{C}/\text{cm}^2</math>)</b> | <b>Zeta Potential<br/>(mV)</b> |
|---------------|------------------------------|-----------------|---------------------------------|----------------------------------------------------------------------|--------------------------------|
| A             | $46.1 \pm 5.7$               | 2               | 1094                            | 2.6                                                                  | -31                            |
| B             | $48.8 \pm 5.1$               | 4               | 2847                            | 6.1                                                                  | -40                            |
| C             | $47.3 \pm 5.1$               | 6               | 4736                            | 10.8                                                                 | -43                            |

\* Only the amount of THOPS is varied with the other conditions remaining that of the typical recipe

Although our main objective here is to fabricate highly charged, monodisperse silica particles with diameters  $\sim 50$  nm, we were also able to prepare highly charged larger silica particles. The silica particle size strongly depends on the amount of ammonium hydroxide added during the Stöber silica condensation process.<sup>29</sup> Fig. 2.3 shows the TEM images of highly charged silica CCA with an average diameter of (a)  $70 \pm 5$  nm and (b)  $237 \pm 7$  nm, respectively.

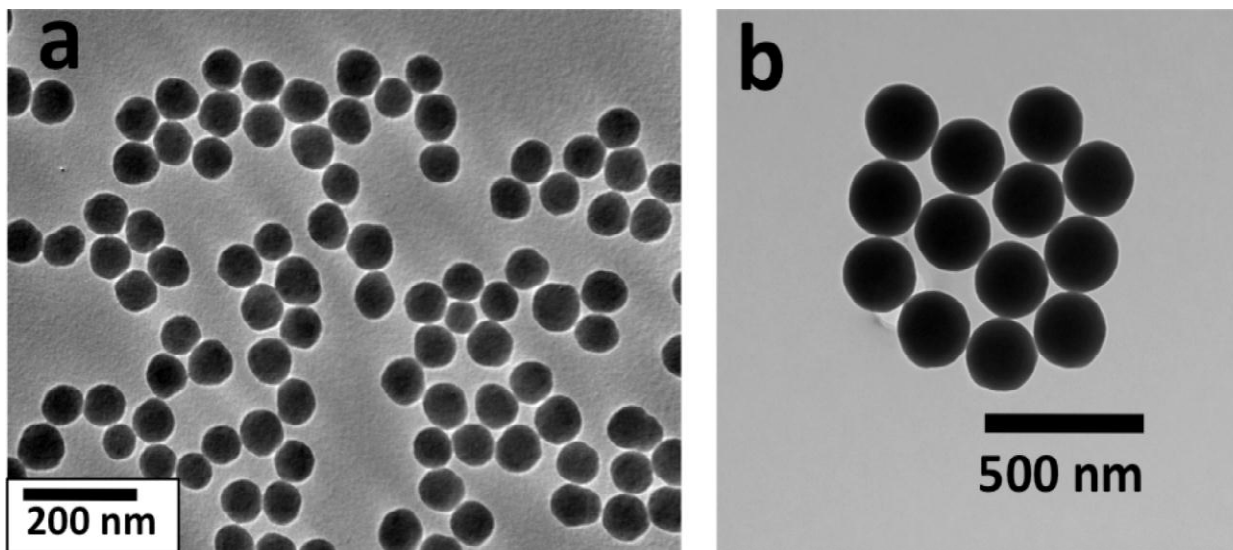


**Figure 2.3** TEM images of samples (a) synthesized with 10 mL and (b) 15 mL of ammonium hydroxide in the Stöber silica synthesis. 2 mL of THOPS was added in the surface modification. Other conditions are those of the typical recipe.

The zeta potentials for these two samples are (a) -33 mV and (b) -46.7 mV respectively, indicating that the silica particles are highly charged.

### 2.3.2 Transmission Measurements of Silica CCA

The highly charged silica particles self-assemble into a CCA after cleaning and ion-exchange. The silica CCA diffraction wavelength can be calculated from Bragg's and Snell's laws according to eqns. 2-1 and 2-2, where  $\lambda_0$  is the wavelength in air diffracted by the CCA, which depends on the average refractive index of the CCA,  $n_{avg}$ , the lattice spacing,  $d$ , and the glancing incident light angle,  $\theta$ . The glancing angle,  $\theta$  in the CCA medium is calculated from Snell's law for refraction, where  $\theta_0$  is the incident glancing angle in air.<sup>27, 33-35</sup>

$$\lambda_0 = 2n_{avg}d \sin \theta \quad (2-1)$$

$$\theta = \cos^{-1} \left[ \frac{\cos \theta_0}{n_{avg}} \right] \quad (2-2)$$

According to Bragg's law, the CCA diffracted wavelength, the  $\lambda_0$  can be easily tuned by adjusting the filter orientation relative to the incident light ( $\theta_0$ ). Larger diffraction wavelength shifts are obtained by changing the particle spacings by adjusting the concentrations of the CCA particles. We diluted the concentrated highly charged silica particles after the last centrifugation to obtain a volume concentration of 6-7 %, for which the silica CCA dispersion Bragg diffracts light in the deep UV. The concentration of the silica CCA was determined gravimetrically from the ratio of the dry weight of the silica CCA particles to the overall weight of the silica CCA dispersion.

The silica CCA dispersion is visually transparent because only light in the deep UV range is diffracted. Fig. 2.4 shows transmission spectra of the silica CCA (volume percent 7.0 %) for incident glancing angles of  $90^\circ$ ,  $69^\circ$  and  $66^\circ$ . The band rejection wavelength was tuned from 237 nm, to 229 nm, and to 227 nm by tilting the filter with respect to the incident beam from  $90^\circ$ , to  $69^\circ$ , and to  $66^\circ$ , as shown in Fig. 2.4. The bandwidths determined from these transmission measurements are broader than the true CCA bandwidths because the absorption spectrophotometer utilizes a somewhat focused exciting beam. The measured attenuation is also artifactually decreased. For normal incidence in Fig. 2.4 the full bandwidth at half maximum (FWHM) observed is 5.0 nm. The CCA filter shows only slight broadening of the rejected FWHM as the filter is angle-tuned, with a FWHM of 5.9 nm as the incident glancing angle is tuned to  $69^\circ$  and  $66^\circ$ .

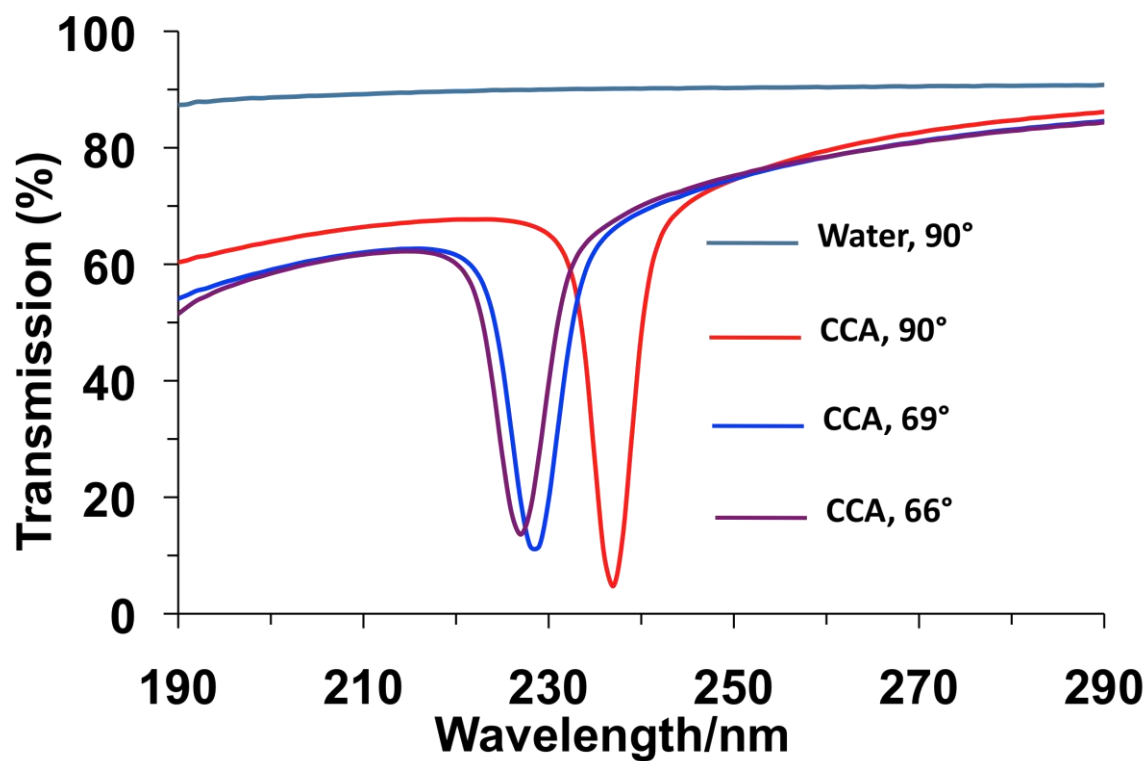


**Figure 2.4** Transmission spectrum of flow cell filled with pure water; and of the flow cells filled with highly charged silica CCA dispersion for incident glancing angles of 90°, 69° and 66°. Silica colloid diameter is  $47.3 \pm 5.1$  nm.

The width of the narrow wavelength Bragg diffraction band depends on the degree of ordering of the silica face centered cubic array within the CCA, the particle diameter, the CCA thickness and the difference between the refractive indices of the charged silica particles and the medium.<sup>8, 27, 36, 37</sup> The diffraction was theoretically calculated by modeling the 3D CCA (111) layers as a 1D stack of dielectric slabs.<sup>27, 36, 38</sup>

Fig. 2.5 compares the observed and calculated diffraction of this silica CCA filter. The dashed line shows the observed light diffraction transmission of the CCA dispersion relative to that of the cell filled with water as obtained in Fig. 2.4. The solid line shows the calculated diffraction from a silica CCA consisting of 1200 face-centered cubic (111) silica particle layers (101  $\mu\text{m}$  total thickness, silica particle diameter of 47 nm). Theory predicts a FWHM of 2 nm and an ultra high attenuation Bragg diffraction transmission of  $\sim 10^{-11}$ . The difference between the observed and theoretical results is presumably due to crystal disorder in the CCA.<sup>37</sup>

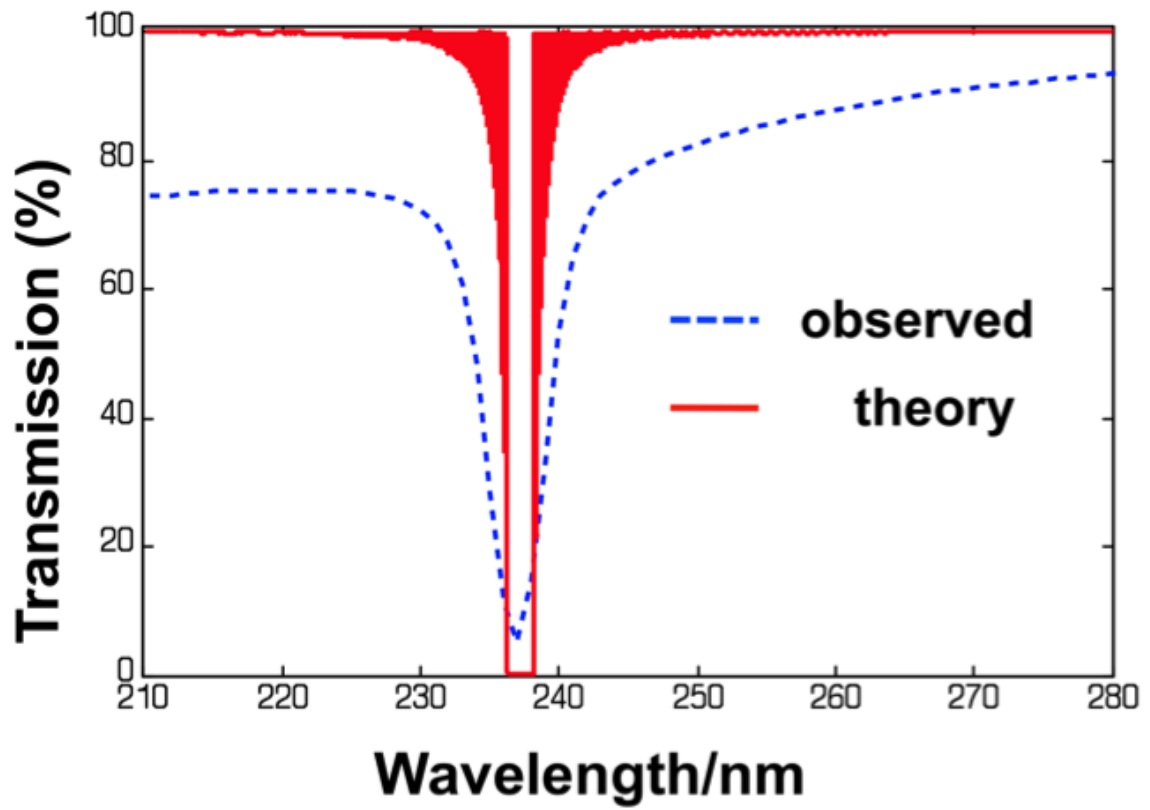
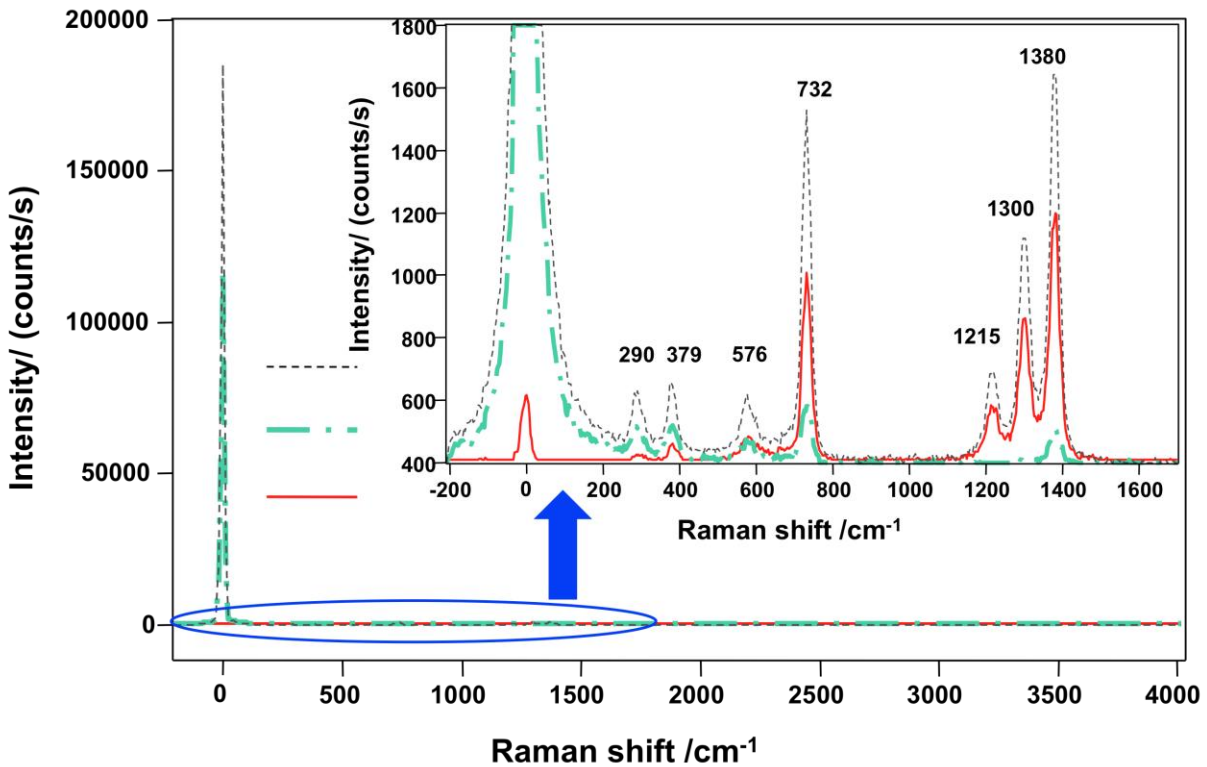


**Figure 2.5** Observed and calculated transmission spectrum of diffraction by silica CCA at a 90° incident angle.

### 2.3.3 Utilization of CCA for UV Raman Rayleigh Rejection

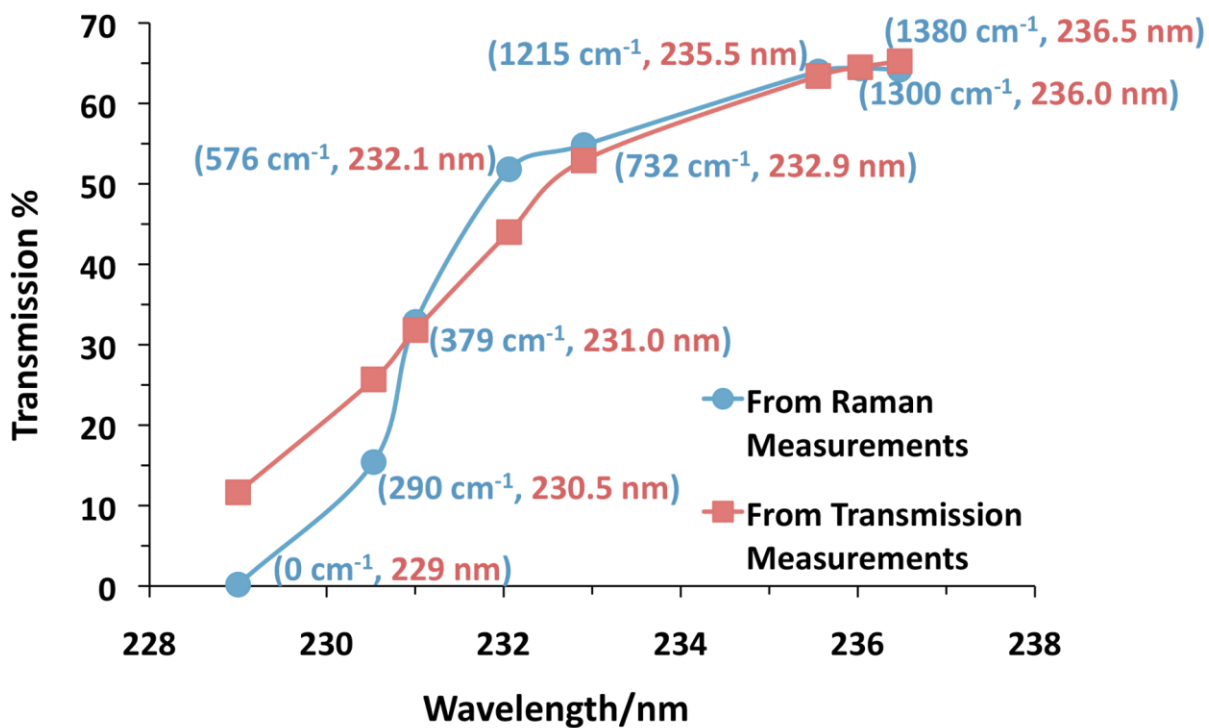
The highly charged silica CCA of Fig. 2.4 was used to reject Rayleigh scattered light in 229 nm excited Raman measurements of Teflon. To conveniently avoid saturating the CCD camera and to quantitatively measure the CCA filter rejection efficiency, we carefully adjusted the premonochromator shown in Fig. 2.1b so that it blocked a portion of the Rayleigh scattered light. The CCA filter was placed between the collection and imaging lens (Fig. 2.1b) where the light is collimated.

Fig. 2.6 shows that the Teflon Raman spectrum measured in the absence of the CCA filter shows a high “Rayleigh peak”. The Fig. 2.6 Teflon Raman spectrum measured using the CCA filter at an incident glancing angle of  $\sim 69^\circ$ , shows a dramatically decreased Rayleigh scattering because the CCA filter Bragg diffracts 229 nm light at the  $\sim 69^\circ$  incident angle orientation (Fig. 2.4). Fig. 2.6 indicates that the CCA filter rejects 99.82 % (ratio of integrated areas) of the Rayleigh scattered light at 229 nm while transmitting the Raman bands of Teflon including the low frequency band at  $290 \text{ cm}^{-1}$  ( $\Delta\lambda=1.5 \text{ nm}$ ). At around normal incidence for the CCA Fig. 2.6 shows that most of the “Rayleigh peak” is present, while the CCA filter rejects the Raman scattered light at  $\sim 1215 \text{ cm}^{-1}$  ( $\sim 236 \text{ nm}$ ), as expected from Fig. 2.4.



**Figure 2.6** Teflon 229 nm UV Raman spectra in the absence (-----) and presence (—) of the CCA filter at an incident glancing angle of ~69°. In addition, the Raman spectrum is shown for the CCA close to normal incidence (— · —). The inset shows an expansion of the circled region.

We calculated the transmission at the wavelengths of the Teflon Raman bands in Fig. 2.6 from the ratios of the integrated Raman band intensities in the absence of the CCA filter. These transmission data were plotted against wavelengths as shown by the dots in Fig. 2.7 and compared to the directly measured transmission from the UV-Vis spectrometer. The Raman data indicate that the CCA filter has a higher rejection efficiency (99.82%) and narrower diffraction bandwidth (HWHM: 2 nm) than the measured transmission (Fig. 2.4). This is because the incident light is well collimated for the CCA filter Raman measurements, while the absorption spectrophotometer uses a somewhat focused beam; the Bragg diffraction strongly depends on the incident angle (eqn. 2-1). We also directly measured that the CCA filter shows a rejection efficiency of 99.9% of the incident 229 nm laser beam using a silicon powermeter.



**Figure 2.7** Transmission calculated from the ratios of integrated intensities of Teflon Raman Bands in Fig. 2.6 for CCA at glancing incident angle of  $\sim 69^\circ$  (the dots, blue); Also shown are transmission data from Fig. 2.4 for CCA at glancing incident angle of  $\sim 69^\circ$  (the squares, red). For comparison, the Raman shifts and corresponding wavelengths were listed next to the data.

## 2.4 CONCLUSIONS

We developed a method to synthesize highly charged, monodisperse silica particles with diameters of ~50 nm and as well as distinctly larger diameters. We can easily incorporate surface charge by reacting the silica particles with the sulfonated silating agent THOPS. The highly charged silica particles self-assemble into CCAs that Bragg diffract light in the deep UV. The CCA Bragg diffracted wavelength can be tuned from 237 nm to 227 nm by tilting the incident glancing angle from ~90° to ~66°. We also demonstrate that the silica CCA filter can be used as a Rayleigh rejection filter for 229 nm deep UV Raman measurements of highly scattering Teflon. The UV Raman measurements show a Rayleigh rejection efficiency of 99.82% and a narrower bandwidth (HWHM= 2 nm). We expect that the performance of the CCA filter can be improved by increasing the ordering of the CCA face centered cubic array by increasing the particle monodispersity and charge.

## 2.5 ACKNOWLEDGEMENT

The authors acknowledge support for this work from the National Institutes of Health (NIH) grant 1R01EB009089. The authors also thank David Tuschel for the help on Teflon Raman measurements as well as Dr. Dan Qu, Zhenmin Hong and Lu Ma for many helpful discussions.

## 2.6 REFERENCES

1. Vieira, M.; Vieira, M. A.; Louro, P.; Costa, J.; Fernandes, M.; Fantoni, A.; Barata, M. J. *Nanosci. Nanotechnol.* **2011**, 11, 5299.
2. Raszewski, Z.; Kruszelnicki-Nowinowski, E.; Kedzierski, J.; Perkowski, P.; Piecek, W.; Dabrowski, R.; Morawiak, P.; Ogrodnik, K. *Mol. Cryst. Liq. Cryst. Sci.* **2010**, 525, 112.
3. Lee, J.; Hahn, C.; Wang, B.; Reichard, K.; Ditto, D.; Glista, D.; Wang, Q.; Yin, S. *Opt. Commun.* **2006**, 258, 184.
4. Philip, J.; Jaykumar, T.; Kalyanasundaram, P.; Raj, B. *Meas. Sci. Technol.* **2003**, 14, 1289.
5. Gupta, N. *Biosensors technologies: acousto-optic tunable filter-based hyperspectral and polarization imagers for fluorescence and spectroscopic imaging; Methods in molecular biology*; Clifton: N.J., 2009, p. 503293
6. Lim, S. H.; Yu, E. T. *Appl. Phys. Lett.* **2009**, 95, 161107.
7. Flaugh, P. L.; O'Donnell, S. E.; Asher, S. A. *Appl. Spectrosc.* **1984**, 38, 847.
8. Asher S. A.; Flaugh, P. L. *Spectroscopy* **1986**, 1, 26.

9. Semenov, G. B.; Aristov, A. K.; Shchedrunova, T. V.; Varnaev, A. V.; Zhevnikov, A. P.; Grozdilov, V. M. *J. Opt. Technol.* **2005**, 72, 196.
10. Cullum, B. M.; Mobley, J.; Chi, Z.; Stokes, D. L.; Miller, G. H.; Vo-Dinh, T. *Rev. Sci. Instrum.* **2000**, 71, 1602.
11. Mobley, J., Cullum, B. M.; Wintenberg, A. L.; Frank, S. S.; Maples, R. A.; Stokes, D. L.; Vo-Dinh, T. *Rev. Sci. Instrum.* **2004**, 75, 2016.
12. Fox, A. E.; Rai, K.; Fontecchio, A. K. *Appl. optics* **2007**, 46, 6277.
13. Lebedkin, S.; Blum, C.; Stürzl, N.; Hennrich, F.; Kappes, M. M. *Rev. Sci. Instrum.* **2011**, 82, 013705.
14. Paillet, M.; Meunier, F.; Verhaegen, M.; Blais-Ouellette, S.; Martel, R. *Rev. Sci. Instrum.* **2010**, 81, 053111.
15. Asher, S. A. *Crystalline Colloidal Narrow Band Radiation Filter*, U. S. Patent 4,627,689, Dec. 9, 1986.
16. Asher, S. A. *Crystalline Colloidal Narrow Band Radiation Filter*, U. S. Patent 4,632,517, Dec. 30, 1986.
17. Kang, K.; Koh, Y. K.; Chirtitescu, C.; Zheng, X.; Cahill, D. G. *Rev. Sci. Instrum.* **2008**, 79, 114901.
18. Pilotto, S.; Pacheco, M. T.; Silveira, L.; Villaverde, A. B.; Zangaro, R. A. *Lasers in medical science* **2001**, 16, 2.
19. de Lima, C. J.; Pacheco, M. T. T.; Villaverde, A. B.; Zangaro, R. A.; Moreira, L. M.; Damiao, A. J. *Spectroscopy* **2008**, 22, 459.
20. Matousek, P. *Appl. Spectrosc.* **2007**, 61, 845.
21. Munro, C. H.; Pajcini, V.; Asher, S. A. *Appl. Spectrosc.* **1997**, 51, 1722.
22. Pelletier, M. J. *Analytical Applications of Raman Spectroscopy*; Blackwell Science Ltd: Oxford, 1999, p. 87.
23. Greenham, A. C.; Nichols, B. A.; Wood, R. M.; Nourshargh, N.; Lewis, K. L. *Opt. Eng.* **1993**, 32, 1018.
24. Zajac M.; Nowak, J. *Applied optics* **1990**, 29, 5198.
25. Pelletier, M. J.; Reeder, R. C. *Appl. Spectrosc.* **1991**, 45, 765.

26. Yang, B.; Morris, M. D.; Michael, D.; Owen, H. *Appl. Spectrosc.* **1991**, 45, 1533.
27. Rundquist, P. A.; Photinos, P.; Jagnathan, S.; Asher, S. A. *J. Chem. Phys.* **1989**, 91, 4932.
28. Asher, S. A.; Wang L.; Tuschel, D. *Crystalline Colloidal Array Deep UV Narrow Band Radiation Filter*, U.S.13/227,066, Patent Pending
29. Stöber, W.; Fink, A. *J. Colloid Interface Sci.* **1968**, 26, 62.
30. Hair M. L.; Hertl, W. *J. Phys. Chem.* **1970**, 74, 91.
31. Kwon, Y. *Handbook of Essential Pharmacokinetics, Pharmacodynamics, and Drug Metabolism for Industrial Scientists*; Kluwer Academic/Plenum Publishers: New York, 2001.
32. Beck, C.; Hartl, W.; Hempelmann, R. *Angew. chem. Int. Ed.* **1999**, 38, 1297.
33. Asher, S. A.; Holtz, J.; Liu, L.; Wu, Z. *J. Am. Chem. Soc.* **1994**, 116, 4997.
34. Hiltner P. A.; Krieger, I. M. *J. Phys. chem.* **1969**, 73, 2386.
35. Krieger I. M.; O'Neill, F. M. *J. Am. Chem. Soc.* **1968**, 90, 3114.
36. Tikhonov, A.; Coalson, R. D.; Asher, S. A. *Phys. Rev. B* **2008**, 77, 235404.
37. Asher, S. A.; Weissman, J. M.; Tikhonov, A.; Coalson, R. D.; Kesavamoorthy, R. *Phys. Rev. E* **2004**, 69, 066619.
38. Yeh, P.; Yariv, A.; Hong, C. S. *J. Opt. Soc. Am.* **1977**, 67, 423.

### **3.0    TEMPLATED PHOTONIC CRYSTAL FABRICATION OF STOICHIOMETRICALLY COMPLEX NANOPARTICLES FOR RESONANCE RAMAN SOLID CROSS SECTION DETERMINATIONS**

(This chapter was published in the *Journal of Physical Chemistry C* 2011, 115, 15767–15771.

The coauthors are Luling Wang, David Tuschel, and Sanford A. Asher.)

Development of methods to fabricate nanoparticles is of great interest for many applications. In this paper, we developed a facile method to fabricate complex stoichiometrically defined nanoparticles by utilizing the defined volume interstices of close-packed photonic crystals. Fabrication of small defined size nanoparticles enables measurements of resonance Raman cross sections of solid materials. We successfully utilized this method to fabricate mixed  $\text{NaNO}_3/\text{Na}_2\text{SO}_4$  nanoparticles with a defined stoichiometry on the surface of the photonic crystal spherical particles. We used these stoichiometrically defined  $\text{NaNO}_3/\text{Na}_2\text{SO}_4$  nanoparticles to determine the solid UV resonance Raman cross section of the  $\text{NO}_3^-$   $\nu_1$  symmetric stretching band (229 nm excitation wavelength) by monitoring the Raman spectrum of  $\text{Na}_2\text{SO}_4$  as an internal standard. These are the first resonance Raman cross section measurements of solids that avoids the biasing of self-absorption. These  $\text{NaNO}_3/\text{Na}_2\text{SO}_4$  nanoparticles appear to show a more facile photolysis than is observed for normal solid  $\text{NaNO}_3$  samples. This templated photonic crystal fabrication of complex nanoparticle method will be important for many applications.

### 3.1 INTRODUCTION

There is great interest in fabricating designer nanoparticles (NPs) for numerous applications, including sophisticated photonic crystals (PCs),<sup>1-6</sup> drug delivery,<sup>7</sup> bioimaging,<sup>8</sup> catalysis,<sup>9</sup> electronics,<sup>10</sup> etc.. The fabrication methodologies often require careful control of reaction conditions such as pH,<sup>1</sup> temperature,<sup>2</sup> reactants,<sup>1, 2</sup> solvents<sup>3</sup> and electric fields<sup>11</sup>. In general, it is still difficult to make NPs of most pure materials, and it is especially difficult to make NPs which homogeneously combine materials with defined stoichiometries.

We report here a facile method to fabricate complex stoichiometrically defined NPs by utilizing the defined volume interstices of close-packed PCs as templates within which we form NPs. We fill the PC interstices with a solution containing the materials of interest. We then freeze the solution and then sublime the solvent which leaves the solute NPs within the PC interstices.

The NPs made here are a homogeneous nanomixture of  $\text{NaNO}_3$ , an energetic material that we wish to determine the resonance Raman cross section of, and  $\text{Na}_2\text{SO}_4$ , an internal standard that is transparent and whose solid Raman cross section we recently measured to be  $2.74 \times 10^{-28} \text{ cm}^2 \cdot \text{molecule}^{-1} \text{ sr}^{-1}$  at 229 nm excitation.<sup>12</sup> While these solid materials can be mixed, any resonance Raman measurement of the mixtures will be biased because the  $\text{NaNO}_3$  particles strongly absorb light and the contribution of  $\text{NaNO}_3$  Raman scattering is decreased compared to that of  $\text{Na}_2\text{SO}_4$ .<sup>13</sup> What is needed is a nanomixture of the materials in which the  $\text{NaNO}_3$  NPs do not significantly attenuate the excitation source traversing the particles. We here demonstrate a method to form a stoichiometrically defined nanomixture of materials with a particle size from 1  $\mu\text{m}$  down to  $\sim 1$  nm.

For many applications it is possible to utilize or study the NPs within the PC interstices. In the case here, the PC is composed of silica spheres that do not absorb light in the UV, visible or in most of the IR spectral region.

If necessary, the NPs can be isolated by dissolving the silica spheres in HF. Alternatively, the PC can be prepared from monodisperse polymer spheres that can be dissolved in organic solvent.

## **3.2 EXPERIMENTAL SECTION**

### **3.2.1 Preparation of Close-Packed Silica PCs**

Silica NPs were purchased from Allied High Tech Products, Inc. (item # 18050015). The silica NPs dispersion was cleaned by six repetitions of the following procedure: The dispersion was centrifuged at 6000 rpm for 20 min and the pellet was discarded. This dispersion was then centrifuged at 10000 rpm for 30 min. This pellet was collected and redispersed in water. Further purification was achieved by shaking the silica dispersion with mixed bed ion-exchange resin (Bio-Rad AG 501-X8) to remove ionic impurities.

The original silica colloid had a dynamic light scattering (DLS) diameter of 84 nm with a DLS calculated polydispersity of 19.1 %. After fractionation the silica colloid had a DLS diameter of 88 nm and a polydispersity of 4.3 %. Fig. 3.1a shows the transmission electron microscopy (TEM) of the original silica colloid while Fig. 3.1b shows a TEM image of fractionated silica colloid which shows a TEM diameter of  $73\pm 7$  nm. The improved

monodispersity is evident, especially the removal of the smaller diameter particles. After cleaning, these silica particles self-assemble into a crystalline colloidal array (CCA).<sup>3, 14, 15</sup>

The close-packed silica PCs were prepared by concentrating the silica CCA solution to 15 wt % silica particles. A 5.75 g portion of this silica CCA in a 10 mL clean beaker was dried at 60 °C in an oven for 24 hr. As the solvent evaporated, the silica CCA formed a close-packed PC.<sup>1</sup>

### **3.2.2 Formation of NaNO<sub>3</sub>/Na<sub>2</sub>SO<sub>4</sub> NPs in Close-packed PCs Interstices**

Fifty milligrams of the silica PCs was placed in a small plastic tube and 8.9 μL of a solution containing NaNO<sub>3</sub> (0.0235 M) and Na<sub>2</sub>SO<sub>4</sub> (0.94 M, mole ratio 1:40) was dropped onto the PC. The solution was sucked into the PC interstices by capillary forces. The PC was then frozen by liquid N<sub>2</sub> and pumped under vacuum for 6 hr to sublime the water. During sublimation, NaNO<sub>3</sub>/Na<sub>2</sub>SO<sub>4</sub> composite NPs formed in the interstices. The PC containing NaNO<sub>3</sub>/Na<sub>2</sub>SO<sub>4</sub> NPS was characterized by scanning electron microscopy (SEM) and Raman spectroscopy.

### **3.2.3 Characterization**

DLS was measured by using a Brookhaven Corp. ZetaPALS. For TEM measurements, a few drops of a dilute dispersion of silica NPs were dried on a carbon-coated copper grid (Ted Pella, Inc.) and observed by using a Philips Mogagni 268 TEM. Samples for SEM were sputter-coated with palladium. SEM studies were performed on a Phillips FEG XL-30 FESEM. Optical images of the silica PC were recorded by using digital stereo zoom microscope (Motic DM-143 series, Ted Pella, Inc.).

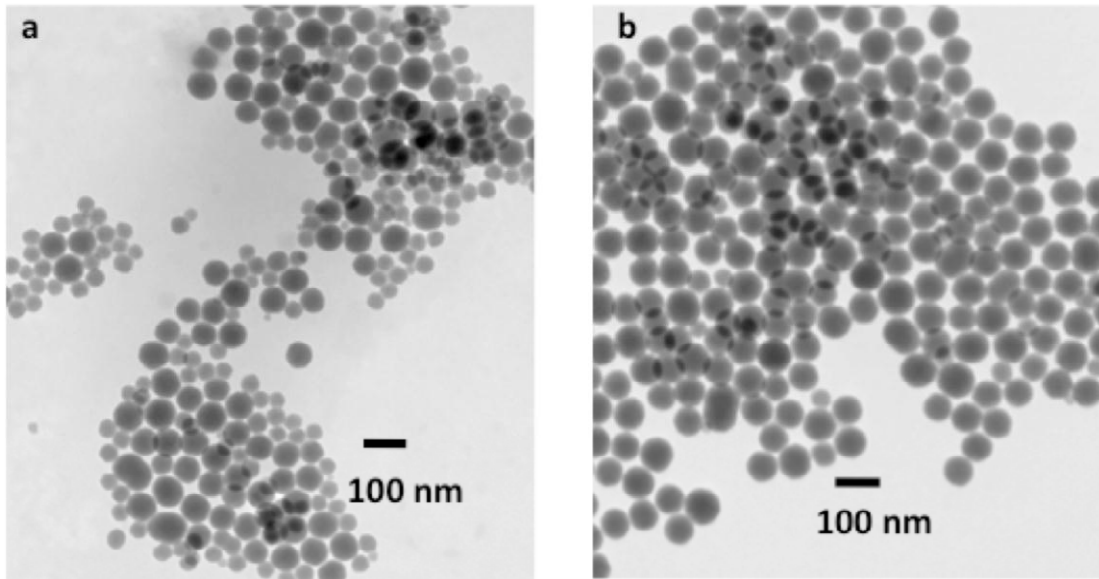


**Figure 3.1** (a) TEM image of original silica colloid; (b) TEM image of silica colloid after cleaning and fractionation

### 3.2.4 Raman of NaNO<sub>3</sub>/Na<sub>2</sub>SO<sub>4</sub> NPs in PC Interstices

Raman spectra were excited with the 229 nm line (0.80 mW) of a CW UV Ar laser (Innova 300 FReD, Coherent Inc.).<sup>16,17</sup> Laser excitation excited the spinning sample approximately in a backscattering geometry with the laser beam focused to a ~20 μm diameter spot. The spinning cell was mounted with its axis of rotation parallel to the optical axis of the collection lens and the cell was spun at > 600 rpm. The samples were mounted on the outer ring (1.5 cm diameter, ~ 2 mm wide) of the spinning cell by using double stick tape (3M, Inc.). The Raman light was dispersed by a modified Spex triplemate spectrograph and a Princeton Instruments CCD camera (Spec-10 System, Model 735-0001).<sup>16,17</sup>

## 3.3 RESULTS AND DISCUSSION

We fabricated these mixed NaNO<sub>3</sub>/Na<sub>2</sub>SO<sub>4</sub> composite NPs within the defined volume interstices of the close-packed silica PC (Figs. 3.2, 3.3). The interstices of the PC were filled with a NaNO<sub>3</sub>/Na<sub>2</sub>SO<sub>4</sub> solution that contained the NaNO<sub>3</sub>/Na<sub>2</sub>SO<sub>4</sub> concentration necessary to form NP of a size equal to the maximum particle size desired. Strong capillary forces sucked the solution into the interstices of the PC. Penetration of the solution was evident since the PC became more transparent as the air was replaced by a solution that better refractive index matched the silica particles. The PC containing the solution was quickly frozen by contact with liquid N<sub>2</sub>. The solvent was sublimated by exposure of the sample to vacuum, leaving behind the NPs.

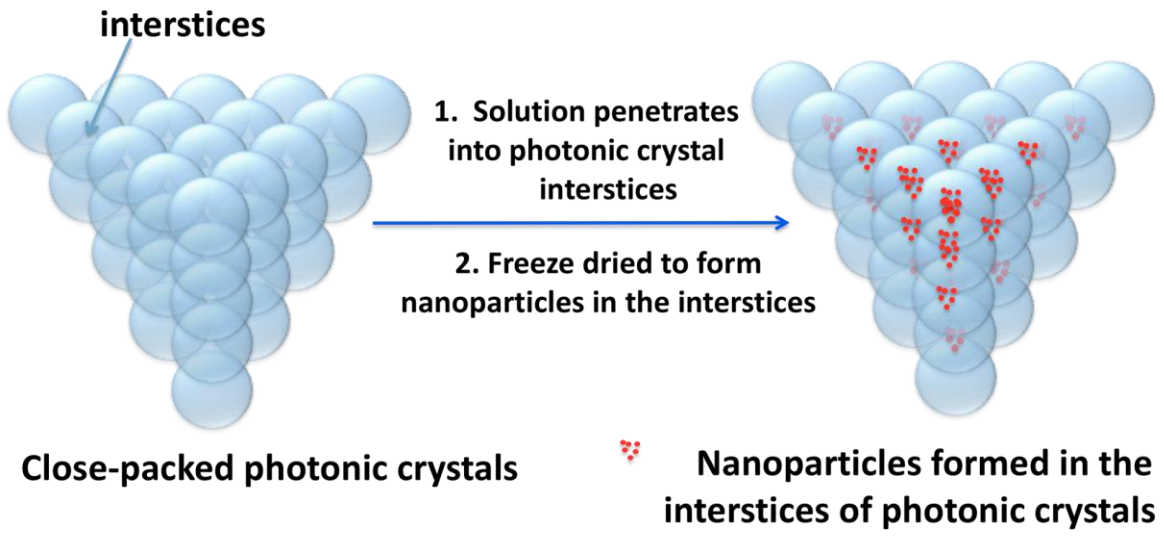


**Figure 3.2** Templated fabrication of nanoparticles in PC interstices.

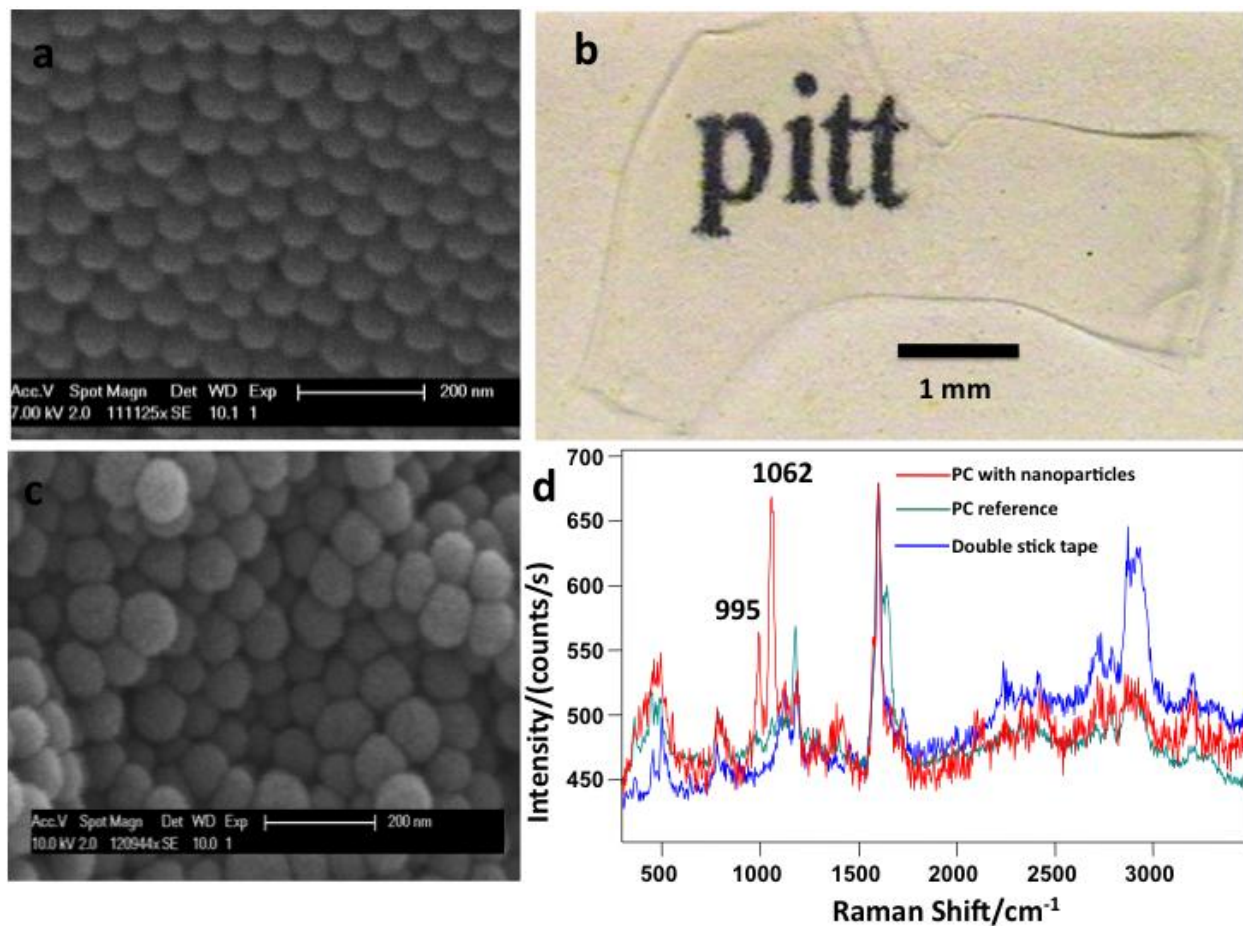


**Figure 3.3** (a) SEM of close-packed PC; (b) Optical image of the close-packed silica PC; (c) SEM image of close-packed PC with NPs ( $\text{NaNO}_3$  to  $\text{Na}_2\text{SO}_4$  mole ratio 1:40) formed in the interstices; (d) Raman spectra of the PCs with NPs in the interstices (red), PC reference (green) and double stick tape.

Fig. 3.3a shows a SEM of the close-packed silica PC, while Fig. 3.3b shows an optical micrograph of the PC prior to solution incorporation. The PC is relatively transparent because the particles are small and the PC diffracts light only in the UV.

The PC interstices function as nanodomains that enclose the penetrating solution. The interstitial volume of the close packed PC is 26%.<sup>18</sup> The single interstitial volume ( $V_{in}$ ) can easily be calculated as:  $V_{in} = (\sqrt{2}/6 - \pi/18)D^3$ , where D is the close packed sphere diameter. The volume of the solution necessary to completely fill all interstices of the PC,  $V_{sol}$  can be calculated from w, the weight of the PC, given that the silica density,  $\rho$ , is 2.0 g/mL<sup>19</sup>:  $V_{sol} = 0.35 w/\rho$ .

We can calculate the maximum diameter of the formed NPs in the interstices from the concentration of non vaporous species in the solution that fills the interstitial volume. The calculated particle diameter is a maximum since the solids can either agglomerate into one single particle or can form numerous particles, or can form arrays of NPs that coat the silica particles surfaces.

The Fig. 3.3c SEM shows that the  $\text{NaNO}_3/\text{Na}_2\text{SO}_4$  NPs coat the surface of silica particles. Visually we estimate a diameter of  $\sim 4$  nm.

We measured the resonance Raman spectra of the  $\text{NO}_3^-$  in the PC by exciting at 229 nm within the  $\text{NO}_3^- \pi \rightarrow \pi^*$  electronic transition.<sup>17, 20, 21</sup> The Fig. 3.3d UV Resonance Raman (RR) spectrum shows a dominating  $1062 \text{ cm}^{-1}$   $\text{NO}_3^-$   $\nu_1$  symmetric stretching vibration<sup>22</sup> as well as the  $995 \text{ cm}^{-1}$   $\text{SO}_4^{2-}$  symmetric stretch. The other Raman bands observed are mainly from the double stick tape and from Raman scattering of the silica PC (Fig. 3.3d). The shoulder at  $\sim 1653 \text{ cm}^{-1}$  in

the PC reference Raman spectrum derives from the degradation of the tape. The spectra in Fig. 3.3d were normalized to the tape 1604  $\text{cm}^{-1}$  Raman band.

Because of the small particle sizes we can ignore the self-absorption by the  $\text{NaNO}_3/\text{Na}_2\text{SO}_4$  NPs since we estimate that it would take a  $\sim 70$  nm thick pure  $\text{NaNO}_3$  film to absorb 50 % of the incident 229 nm excitation light.<sup>21</sup> We can calculate the solid Raman cross section of the  $\nu_1$  symmetric stretch of  $\text{NO}_3^-$  ( $\sigma_{\text{NO}_3^-}$ ) from the ratio of intensities of the  $\text{NO}_3^-$   $\nu_1$  symmetric stretch band ( $I_{\text{NO}_3^-}$ ) to the  $\text{SO}_4^{2-}$  symmetric stretch band ( $I_{\text{SO}_4^{2-}}$ ) by using eqn. 3-1.

$$\frac{I_{\text{NO}_3^-}}{I_{\text{SO}_4^{2-}}} = \frac{\sigma_{\text{NO}_3^-} * C_{\text{NO}_3^-}}{\sigma_{\text{SO}_4^{2-}} * C_{\text{SO}_4^{2-}}} \Rightarrow \sigma_{\text{NO}_3^-} = \frac{I_{\text{NO}_3^-} * C_{\text{SO}_4^{2-}}}{I_{\text{SO}_4^{2-}} * C_{\text{NO}_3^-}} * \sigma_{\text{SO}_4^{2-}} \quad (3-1)$$

The concentration ratio ( $C_{\text{NO}_3^-}/C_{\text{SO}_4^{2-}}$ ) of the NP is that of the solution that penetrated the PC interstices (1:40). The measured relative intensity ( $I_{\text{NO}_3^-}/I_{\text{SO}_4^{2-}}$ ) of 2.6 was obtained by integrating the Raman bands in Fig. 3.3d. We recently measured a solid state Raman cross section of the 995  $\text{cm}^{-1}$   $\text{SO}_4^{2-}$  band of  $1.97 \times 10^{-28} \text{ cm}^2 \cdot \text{molc}^{-1} \text{ sr}^{-1}$  with 244 nm excitation.<sup>12</sup> By using the Raman cross section wavelength dispersion,<sup>20</sup> we calculated a solid state 229 nm Raman cross section of the 995  $\text{cm}^{-1}$   $\text{SO}_4^{2-}$  band of  $2.74 \times 10^{-28} \text{ cm}^2 \cdot \text{molc}^{-1} \text{ sr}^{-1}$ . From this, we calculate a solid 229 nm resonance Raman cross section for the  $\text{NO}_3^-$   $\nu_1$  symmetric stretch band of  $2.85 \times 10^{-26} \text{ cm}^2 \cdot \text{molc}^{-1} \text{ sr}^{-1}$ .

Thus, we find that the solid state Raman cross section of the  $\text{NO}_3^-$   $\nu_1$  symmetric stretch band is around 40% of the solution 229 nm Raman cross section of  $7.4 \times 10^{-26} \text{ cm}^2 \cdot \text{molecule}^{-1} \text{ sr}^{-1}$ .<sup>17</sup> We believe that this is the first solid state resonance Raman cross section measurement for any compound. The fact that the solid state and solution resonance Raman cross sections are different indicates the resonance Raman enhancement is somewhat impacted by interactions

between adjacent electronic transitions of the  $\text{NO}_3^-$  groups in the lattice, relative to that of the isolated  $\text{NO}_3^-$  in water.

The solid and solution  $\text{NO}_3^-$  Raman cross sections are expected to differ because of both chemical and electromagnetic differences. The chemical difference will cause changes in the ground and excited states and shift the transition energies and cause changes in the homogeneous and inhomogeneous linewidths. These effects will also change the relative Raman cross sections between the solution and solid states.

The electromagnetic differences result from the change in the exciting and Raman scattered electric fields in the solution state with refractive index  $n_s$  versus the solid state with refractive index of  $n_c$ .<sup>23</sup> From the local field corrections we expected to see larger solid nitrate Raman cross section than the solution value because of higher refractive index of the solid materials. However, this is opposite to our experimental results where the solid nitrate Raman cross section is around 40% of the solution value, which indicates that the cross section differences between the pure solid versus the solution are dominated by chemical differences.

This result is important in any understanding of the difference in quantum yields of the photochemical reaction  $\text{NO}_3^- + h\nu \rightarrow \text{NO}_2^-$  that we measured to be 0.04 for  $\text{NO}_3^-$  dissolved in water, but is much smaller with a quantum yield of  $10^{-8}$  for solid  $\text{NaNO}_3$ .<sup>24</sup> This suggests that the decreased solid state quantum yield may be related to constraints by the  $\text{NO}_3^-$  surrounding lattice.

In this regard we see a significantly larger photochemical quantum yield for the  $\text{NaNO}_3/\text{Na}_2\text{SO}_4$  NPs than for solid  $\text{NaNO}_3$ . Fig. 3.4 shows the illumination time dependence of the 229 nm excited UVRR of a spinning sample of the  $\text{NaNO}_3/\text{Na}_2\text{SO}_4$  NPs. We observed a significant decrease in the relative intensity of the  $1062\text{ cm}^{-1}$   $\text{NO}_3^-$   $\nu_1$  symmetric stretching

vibration compared to the  $995\text{ cm}^{-1}$   $\text{SO}_4^{2-}$  symmetric stretch after 60 s illumination. A spinning solid  $\text{NaNO}_3$  sample shows negligible photochemistry under these conditions.<sup>24</sup> It is surprisingly that Fig. 3.4 does not show the  $\nu_1$  symmetric stretching band at  $\sim 1332\text{ cm}^{-1}$  of  $\text{NO}_2^-$ , the expected photochemical product.

In contrast, the Fig. 3.5 UV resonance Raman spectrum of a stationary sample of the  $\text{NaNO}_3/\text{Na}_2\text{SO}_4$  NP clearly shows the  $\text{NO}_2^-$   $\nu_1$  symmetric stretching band at  $\sim 1332\text{ cm}^{-1}$  of the photochemical formation of  $\text{NO}_2^-$ . We will investigate the lack of the  $\sim 1332\text{ cm}^{-1}$   $\text{NO}_2^-$  band in the spinning samples in future studies. We will also better characterize the photochemical quantum yields of the  $\text{NaNO}_3/\text{Na}_2\text{SO}_4$  NPs.

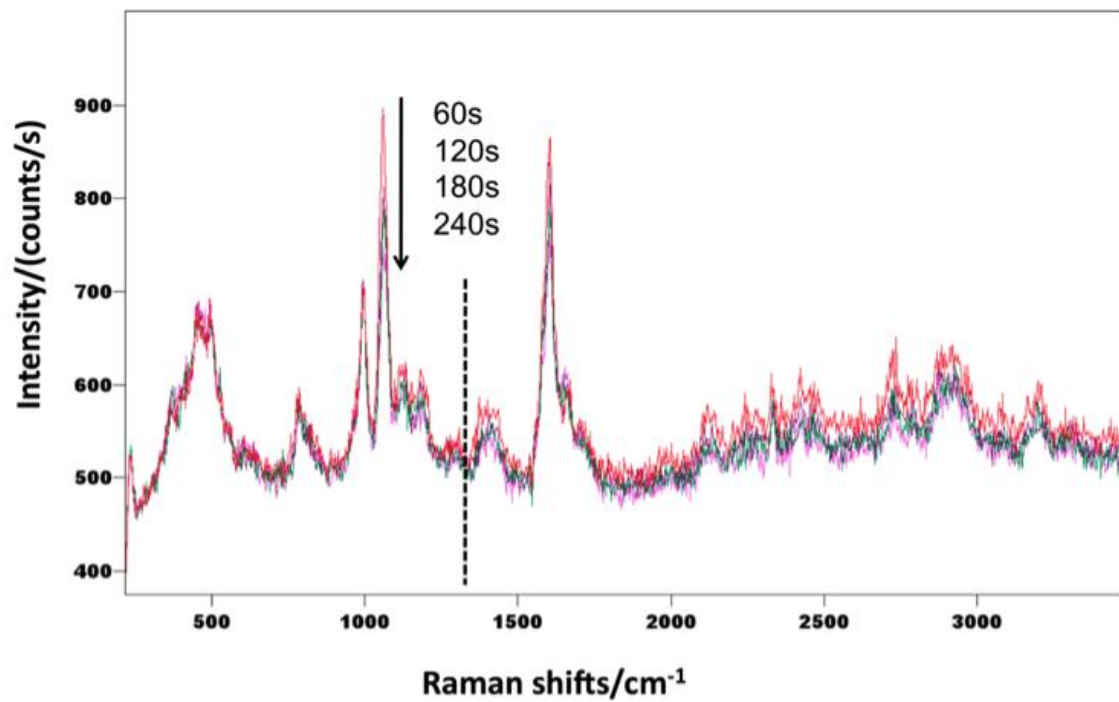


**Figure 3.4** Raman spectra of the NaNO<sub>3</sub>/Na<sub>2</sub>SO<sub>4</sub> nanoparticles (NaNO<sub>3</sub> to Na<sub>2</sub>SO<sub>4</sub> mole ratio 1:40) in the PC interstices at illuminating times of 60 s, 120 s, 180 s and 240 s respectively.

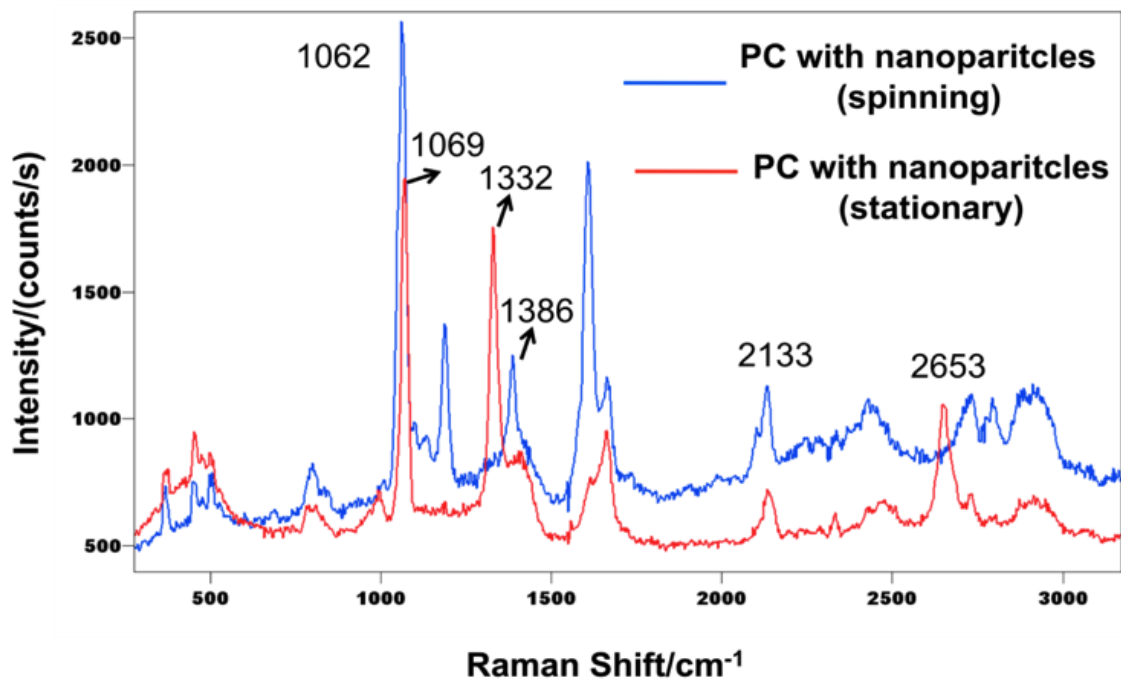


**Figure 3.5** Raman spectra of the NaNO<sub>3</sub>/Na<sub>2</sub>SO<sub>4</sub> nanoparticles (NaNO<sub>3</sub> to Na<sub>2</sub>SO<sub>4</sub> mole ratio 1.67:1) in the PC interstices under the spinning (blue) and stationary (red) conditions.

### 3.4 CONCLUSIONS

We developed a facile method of fabricating complex stoichiometry NPs by utilizing the defined volume interstices of close-packed PC as templates. We successfully utilized this method to fabricate mixed  $\text{NaNO}_3/\text{Na}_2\text{SO}_4$  NPs. SEM and Raman spectroscopy show that the  $\sim 4$  nm mixed  $\text{NaNO}_3/\text{Na}_2\text{SO}_4$  NPs formed on the surfaces of the PC spherical particles. By using  $\text{Na}_2\text{SO}_4$  as an internal standard, we determined that the solid Raman cross section of the  $\text{NO}_3^-$   $\nu_1$  symmetric band is  $2.85 \times 10^{-26} \text{ cm}^2 \cdot \text{molecule}^{-1} \text{ sr}^{-1}$ . We also observe much more facile photolysis of the  $\text{NaNO}_3/\text{Na}_2\text{SO}_4$  NPs than for solid  $\text{NaNO}_3$ . This templated PC fabrication of complex NPs method will be important for many applications, one of which is for determining the resonance Raman cross section of solid materials.

### 3.5 ACKNOWLEDGEMENTS

We acknowledge partial funding of this work by the West Virginia High Technology Consortium Foundation under contract number HSHQDC-09-C-00159 from the Department of Homeland Security Science and Technology Directorate. We thank Materials Micro-characterization Laboratory (University of Pittsburgh) for the use of the SEM instrument.

### 3.6 REFERENCES

1. Wang, L.; Asher, S. A. *Chem. Mater.* **2009**, 21, 4608.
2. Reese, C. E.; Guerrero, C. D.; Weissman, J. M.; Lee, K.; Asher, S. A. *J. Colloid Interface Sci.* **2000**, 232, 76.
3. Wang, W.; Asher, S. A. *J. Am. Chem. Soc.* **2001**, 123, 12528.
4. Xu, X.; Majetick, S.; Asher, S. A. *J. Am. Chem. Soc.* **2002**, 124, 13864.
5. Luo, J.; Qu, D.; Tikhonov, A.; Bohn, J.; Asher, S. A. *J. Colloid Interface Sci.* **2010**, 345, 131.
6. Pan, G.; Tse, A.S.; Kesavamoorthy, R.; Asher, S. A. *J. Am. Chem. Soc.* **1998**, 120, 6518.
7. Moinard-Checot, D.; Chevalier, Y.; Briancon, S.; Fessi, H.; Guinebretiere, S. J. *Nanosci. Nanotechnol.* **2006**, 6, 2664.
8. Selvan, S. T.; Tan, T. T. Y.; Yi, D. K.; Jana, N. R. *Langmuir* **2010**, 26, 11631.
9. Toshima, N. *Inorganic Nanoparticles*; CRC Press: Boca Raton, FL, 2011; Chapter 17, pp 475.
10. Joo, S.; Baldwin, D. F. *IEEE Electron. Compon. Technol. Conf.* **2007**, 1, 219.
11. Zhao, H.; Liu, X.; Tse, S. D. *J. Nanopart. Res.* **2008**, 10, 907.
12. Wang, L.; Asher, S. A. *Refractive-index Matching Avoids Local Field Corrections and Scattering Bias in Solid State Na<sub>2</sub>SO<sub>4</sub> UV Raman Cross Section Measurements*, *Appl. Spectrosc.*, (accepted).
13. Shriver, D. F.; Dunn, J. B. R. *Appl. Spectrosc.* **1974**, 28, 319.
14. Carlson, R. J.; Asher, S. A. *Appl. Spectrosc.* **1984**, 38, 297.
15. Rundquist, P. A.; Photinos, P.; Jagannathan, S.; Asher, S. A. *J. Chem. Phys.* **1989**, 91, 4932.

16. Asher, S. A.; Bormett, R. W.; Chen, X. G.; Lemmon, D. H.; Cho, N.; Peterson, P.; Arrigoni, M.; Spinelli, L.; Cannon, J. *Appl. Spectrosc.* **1993**, 47, 628.
17. Tuschel, D. D.; Mikhonin, A. V.; Lemoff, B. E.; Asher, S. A. *Appl. Spectrosc.* **2010**, 64, 425.
18. Chung, Y. *Introduction to materials science and engineering*; CRC Press: Boca Raton, FL, 2007; p 16.
19. Jiang, P.; Bertone, J. F.; Hwang, K. S.; Colvin, V. L. *Chem. Mater.* **1999**, 11, 2132.
20. Dudik, J. M.; Johnson, C. R.; Asher, S. A. *J. Chem. Phys.* **1985**, 82, 1732.
21. Ianoul, A.; Coleman, T.; Asher, S. A. *Anal. Chem.* **2002**, 74, 1458.
22. Hickey, L.; Kloprogge, J. T.; Frost, R. L. *J. Mater. Sci.* **2000**, 35, 4347.
23. Mirone, P. *Spectrochimica Acta* **1966**, 22, 1897.
24. Asher, S. A.; Tuschel, D. D.; Vargson, T. A.; Wang, L.; Geib, S. *J. Phys. Chem. A* **2011**, 115, 4279.

#### 4.0 REFRACTIVE-INDEX MATCHING AVOIDS LOCAL FIELD CORRECTIONS AND SCATTERING BIAS IN SOLID-STATE Na<sub>2</sub>SO<sub>4</sub> UV RAMAN CROSS SECTION MEASUREMENTS

(This chapter was submitted to *Applied Spectroscopy* and has been accepted. It is tentatively scheduled for publication as a Submitted Paper in the February 2012 issue [66(2)] of *Applied Spectroscopy*. The coauthors are Luling Wang and Sanford A. Asher. The work here is part of the extension from Chapter 3 which needs the solid state Na<sub>2</sub>SO<sub>4</sub> Raman cross section as an internal standard for the solid state NaNO<sub>3</sub> Raman cross section determination.)

We report a refractive-index matching method to measure nonabsorbing solid UV Raman cross sections that avoids the local field correction and interface scattering of incident light. We used refractive-index matched chloroform as an internal standard to determine the solid state 995 cm<sup>-1</sup> Na<sub>2</sub>SO<sub>4</sub> 244 nm Raman cross sections. The pure liquid chloroform 668 cm<sup>-1</sup> 244 nm Raman cross section was determined by using acetonitrile as an internal standard and by calculating the local field corrections for the observed Raman intensities. Our measured 244 nm UV Raman cross sections of the solid-state 995 cm<sup>-1</sup> SO<sub>4</sub><sup>2-</sup> band of  $1.97 \pm 0.07 \times 10^{-28}$  cm<sup>2</sup>/(mol·sr), is about half of its aqueous solution Raman cross section indicating interactions between the sulfate species in the solid that decrease the Raman polarizability.

## 4.1 INTRODUCTION

Raman spectroscopy is a powerful method for studying molecular structure and environment.<sup>1-3</sup> The Raman intensities observed are proportional to the molecular Raman cross sections. Thus, Raman intensities can be used to determine molecular concentrations if the Raman cross sections are known, if and only if, the excitation beam sampling is defined with respect to the collection optics.<sup>4</sup> Unfortunately, direct measurements of Raman cross sections are very difficult because the measurements require a detailed understanding of both the incident laser light excitation geometry (including the excitation beam attenuation within the sample), the effective Raman scattered light collection solid angle, as well as the transfer efficiency of the spectrometer.<sup>5-9</sup>

Most previous studies of Raman cross sections measured the Raman cross sections of liquid solutions by using internal standards with known Raman cross sections.<sup>10-18</sup> Some of these studies<sup>10, 18</sup> directly reference their relative intensity measurements to the determination of the absolute Raman cross section of benzene at 514.5 nm by Kato et al.<sup>5</sup> and Abe et al.,<sup>19</sup> while others<sup>11-17</sup> reference their measured intensities to more recently measured Raman cross sections, that, however, were also referenced to benzene. The internal standard methods are relatively easy and quite accurate for measuring Raman cross sections for liquids or species in solution.

In contrast, there are very few measurements of Raman cross sections of solids.<sup>20-22</sup> Raman cross section measurements of solids are more challenging because it is more difficult to homogeneously disperse different species in order to use internal standard methods. Many analytically important applications require determination of the concentrations of solid state materials. This is the case for explosive materials, for example, that are almost always found in the solid state.<sup>20</sup>

We recently developed a method to disperse sub 20 nm solid particles in the interstices of close packed silica photonic crystals.<sup>23</sup> This created a solid state sample where the individual particles were too small to attenuate the resonant incident exciting light or the Raman scattered light traversing individual particles. This prevented self-absorption bias in the measurement such that the relative intensities observed were proportional to the solid state particle Raman cross sections.

We achieved the intimate mixing of the <20 nm particles of the analyte and the internal standard by subliming a frozen solution containing both the analyte and internal standard species that filled the nanosize interstices of a close packed silica opal photonic crystal. In order to determine the solid Raman cross section of the analyte solid particles we needed to determine the Raman cross sections of a convenient solid particle internal standard.<sup>23</sup>

In the work here we demonstrate a refractive-index matching method used to determine the Raman cross sections for solid nonabsorbing Na<sub>2</sub>SO<sub>4</sub> particles. We use pure chloroform as an internal standard since it has a 244 nm refractive index of ~1.53,<sup>24</sup> almost identical to that of solid Na<sub>2</sub>SO<sub>4</sub>.<sup>25</sup> In addition, it does not dissolve Na<sub>2</sub>SO<sub>4</sub>. Refractive index matching the solid Na<sub>2</sub>SO<sub>4</sub> particles avoids any scattering by the particle-solvent interface which would limit the particle penetration of the excitation wavelength. We determined the 244 nm UV Raman cross section of chloroform by measuring the Raman intensity ratio of chloroform to that of acetonitrile in a chloroform/acetonitrile solution. We determined the Raman cross section of chloroform in the neat solvent by calculating the local field correction. We then suspended the rapidly mixed, finely ground solid Na<sub>2</sub>SO<sub>4</sub> particles in neat chloroform in order to measure the 244 nm UV Raman intensity ratio of the solid Na<sub>2</sub>SO<sub>4</sub> particle relative to chloroform.

## 4.2 EXPERIMENTAL SECTION

### 4.2.1 UV Raman Spectroscopy Instrumentation

The spectroscopic instrumentation was described in detail elsewhere.<sup>26, 27</sup> Raman spectra were excited with the 244 nm line of a CW UV Ar Laser (Innova 300 FReD, Coherent Inc.). The samples were rapidly stirred in a sealed fused-silica cylindrical quartz cell with a 10 mm light path. The laser excitation excited the sample in a backscattering geometry with a beam spot size ~25  $\mu\text{m}$ . The Raman scattered light was dispersed and detected by a Spex Triplemate Spectrograph and a Princeton Instruments CCD camera (Spec-10 System, Model 735-0001). Neat acetonitrile was used for the Raman shift calibration.

### 4.2.2 UV Raman Measurements of Acetonitrile, Chloroform and Chloroform/Acetonitrile

The chloroform/acetonitrile mixture was prepared by mixing a volume ratio of 1:3 of the two liquids. We consecutively collected three spectra of 1.5 s accumulations each. No UV Raman spectral differences were evident between consecutive spectra. This indicates a lack of sample degradation, even though the  $\text{CHCl}_3$  absorbs some of the laser light (molar absorptivity of  $0.0743 \text{ L}\cdot\text{mol}^{-1}\cdot\text{cm}^{-1}$ , calculated from the pure chloroform UV-Vis absorption spectrum (Fig. 4.1)).

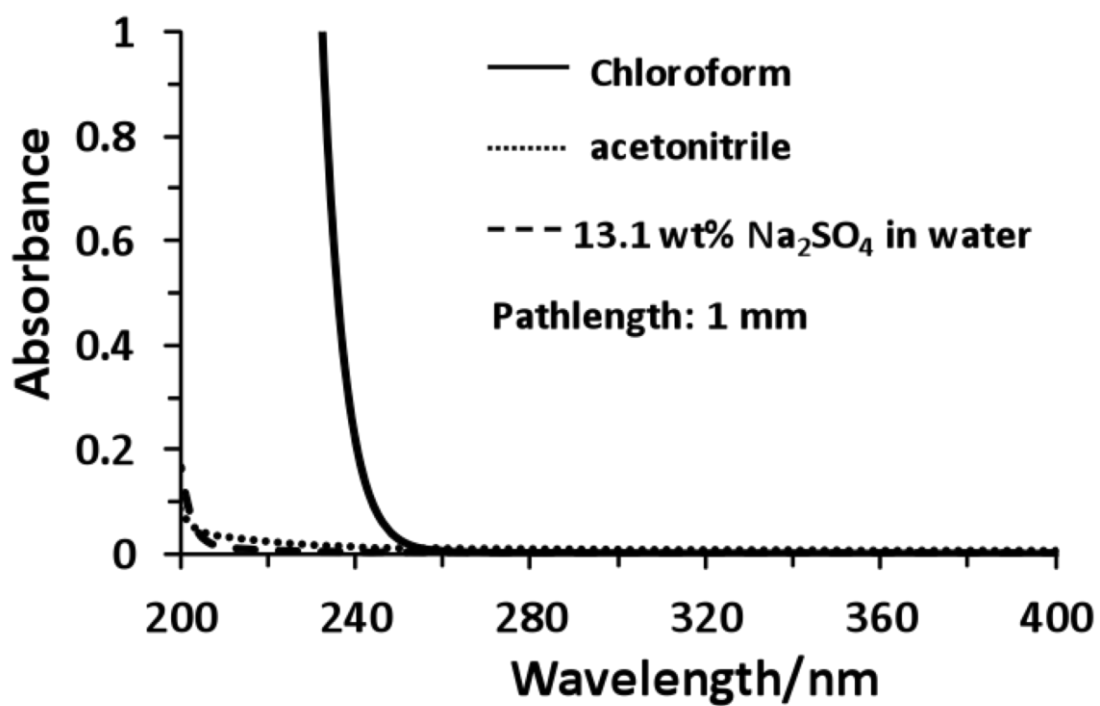


**Figure 4.1** UV-Vis absorbance spectra of pure chloroform, pure acetonitrile and 13.1 wt% Na<sub>2</sub>SO<sub>4</sub> in water.

### 4.2.3 UV Raman Measurements of Chloroform and Na<sub>2</sub>SO<sub>4</sub>/Chloroform Dispersion

Anhydrous solid Na<sub>2</sub>SO<sub>4</sub> was finely ground by using a mortar and pestle. Fig. 4.2 shows a micrograph of ground solid Na<sub>2</sub>SO<sub>4</sub> particles showing an average diameter <30 μm. The finely powdered Na<sub>2</sub>SO<sub>4</sub> was suspended in neat chloroform at Na<sub>2</sub>SO<sub>4</sub> concentrations of 23.6 mg/mL (mole ratio 1:73.7), 29.8 mg/mL (mole ratio 1:58.1) and 86.6 mg/mL (mole ratio 1:19.6). The sample was rapidly stirred to produce a homogeneous suspension in the cylindrical fused quartz sample cell. For each sample, Raman spectra were obtained at, at least, three different heights; the similarity of the spectra indicated sample homogeneity. Each measurement was repeated at least three times with 15 s accumulations each. The Raman spectra were similar indicating that no sample degradation occurred.

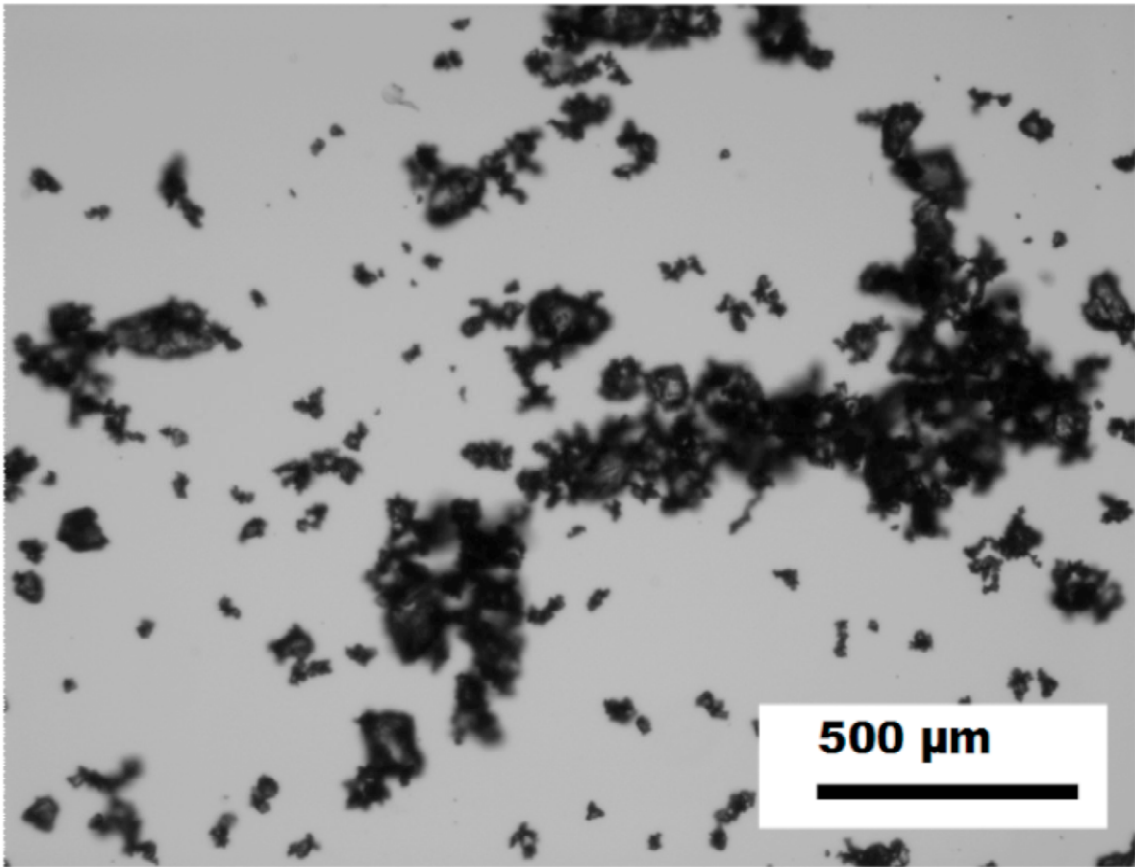


**Figure 4.2** Optical image of ground solid  $\text{Na}_2\text{SO}_4$  particles.

#### 4.2.4 UV Raman Measurements of Acetonitrile and Na<sub>2</sub>SO<sub>4</sub>/ acetonitrile

For comparison, we also measured UV Raman spectra of finely powdered Na<sub>2</sub>SO<sub>4</sub> suspended in non refractive-index matched acetonitrile at Na<sub>2</sub>SO<sub>4</sub> concentrations of 19.4 mg/mL (mole ratio 1:136.6), 29.0 mg/mL (mole ratio 1:90.6) and 52.1 mg/mL (mole ratio 1:48.8) using a method identical to that for solid Na<sub>2</sub>SO<sub>4</sub> particles in chloroform, as described above.

### 4.3 RESULTS AND DISCUSSION

#### 4.3.1 Dependence of Raman Cross Sections on the Local Field

Eqn. 4-1 shows the expression for the Raman cross section  $\sigma(\nu_0)$ , where  $\nu_0$  and  $\nu$  are the frequencies (cm<sup>-1</sup>) of the excitation light and the molecular vibrational frequency,  $b$  is the zero-point amplitude of the vibrational mode,  $g$  is the vibrational mode degeneracy,  $\alpha'$  is the symmetric and  $\gamma'$  is the anisotropic invariant of the polarizability tensor,  $\rho_s$  is the depolarization ratio for linearly polarized incident light,  $\mathbf{e}$  and  $\mathbf{e}'$  are the electric field polarization vectors of the exciting light and the Stokes scattered light,  $L$  is a local field correction factor associated with the increase in the Raman intensity of the analyte in the condensed phase of refractive index  $n$ , compared to that of the isolated molecule in the gas phase.<sup>28, 29</sup>  $L$  is described by eqn. 4-2, where  $n_0$  and  $n_s$  are the *homogeneous* sample refractive indices at  $\nu_0$  and  $\nu_0 - \nu$ .<sup>28, 29</sup>

$$\sigma(\nu_0) = \frac{(2\pi)^4}{45} b^2 g \frac{(\nu_0 - \nu)^4}{1 - \exp(-\frac{hc\nu}{kT})} \cdot (45\alpha'^2 + 7\gamma'^2) \left[ \frac{\rho_s + (1 - \rho_s) \cdot |\mathbf{e} \cdot \mathbf{e}'|^2}{1 + \rho_s} \right] \cdot L \quad (4-1)$$

$$L = (n_s / n_0)(n_s^2 + 2)^2(n_0^2 + 2)^2 / 81 \quad (4-2)$$

Many previous studies demonstrated that the ratio of Raman cross sections of a molecule dissolved within its own pure liquid state ( $\sigma_l$ ) to that as a solute molecule ( $\sigma_m$ ) in solution is proportional to the ratio of the local field correction factors of the pure liquid ( $L_l$ ) to that of the solution ( $L_m$ ) as described by eqn. 4-3, where the refractive indices  $n_l$  and  $n_m$  are those of the pure liquid and of the solution samples of the molecule, respectively.<sup>19,30,31</sup>

$$\frac{\sigma_m}{\sigma_l} = \frac{L_m}{L_l} = \left[ \frac{3}{(n_l / n_m)^2 + 2} \right]^4 \quad (4-3)$$

This local field correction accounts for the increase in the electromagnetic field associated with the polarization of the environment around the Raman scattering molecule. The observed Raman intensity ( $I$ ) is described by eqn. 4-4, where  $N$  is the number of molecules contained in the illuminated volume whose Raman scattering is transferred into the spectrometer.  $F(n, \theta)$  is the fraction of the scattered light imaged into the spectrometer which depends upon the solid angle collected ( $\theta$ ), which depends upon the sample refractive index ( $n$ ) at the Raman scattered frequency.  $S(\nu_0 - \nu)$  is a complex factor describing the efficiency of light collection from the sample volume elements whose scattering is transferred into the spectrometer. It recognizes attenuation of the excitation beam and Raman scattered light within the sample by phenomena such as absorption and sample scattering.  $E(\nu_0 - \nu)$  is the throughput efficiency of the spectrometer at the Raman scattered frequency.<sup>10</sup>

$$I(\nu_0) = N I_0 F(n, \theta) S(\nu_0 - \nu) E(\nu_0 - \nu) \sigma(\nu_0) \quad (4-4)$$

The observed Raman intensity ratio of two species, a, the analyte and b, the internal standard molecularly dispersed within a single solution is given by eqn. 4-5.

$$\frac{I_m^a(\nu_0)}{I_m^b(\nu_0)} = \frac{N_a I_0 F(n, \theta) S(\nu_0 - \nu) E(\nu_0 - \nu) \sigma_m^a(\nu_0)}{N_b I_0 F(n', \theta) S(\nu_0 - \nu') E(\nu_0 - \nu') \sigma_m^b(\nu_0)} \sim \frac{N_a \sigma_m^a(\nu_0)}{N_b \sigma_m^b(\nu_0)} \quad (4-5)$$

$$\sigma_m^a(\nu_0) \sim \frac{I_m^a(\nu_0)}{I_m^b(\nu_0)} \cdot \frac{N_b}{N_a} \cdot \sigma_m^b(\nu_0) \quad (4-6)$$

Equation 4-6 shows that the common internal standard method of determining the analyte Raman cross section ( $\sigma_m^a(\nu_0)$ ) from the ratio of observed intensities of the analyte to that of the internal standard only requires knowing the relative concentrations of the analyte ( $N_a$ ) and internal standard molecules ( $N_b$ ), as well as the internal standard Raman cross section ( $\sigma_m^b(\nu_0)$ ), assuming negligible differences between  $F(n, \theta)$  and  $F(n', \theta)$ ,  $S(\nu_0 - \nu)$  and  $S(\nu_0 - \nu')$ , and  $E(\nu_0 - \nu)$  and  $E(\nu_0 - \nu')$  at the Raman scattered frequency of the analyte ( $\nu_0 - \nu$ ) versus that at the internal standard ( $\nu_0 - \nu'$ ), respectively. The subscript  $m$  indicates the sample solution.

The local field effect causes the Raman cross sections of molecules with identical Raman polarizabilities to show different Raman cross sections, and, thus, scatter with different Raman intensities in media of different refractive index. Eqn. 4-3 indicates that the local field correction increases the Raman cross section in the pure liquid if its refractive index exceeds that of the solution sample. The solution Raman cross sections of the analyte and internal standard can be related to their pure molecule Raman cross sections by Eqn. 4-3.

We can calculate the analyte pure liquid Raman cross section from that measured in the solution with the dissolved internal standard if we know the pure internal standard Raman cross section. Substituting the  $\sigma_m^a(\nu_0)$  and  $\sigma_m^b(\nu_0)$  in eqn. 4-6 with that of the pure analyte ( $\sigma_l^a(\nu_0)$ ) and pure internal standard Raman cross sections ( $\sigma_l^b(\nu_0)$ ) and including the local field correction, we can write the relationship between the pure analyte Raman cross section to that of pure internal

standard (eqn. 4-7, the subscript  $l$  indicates pure liquid or solid compound state). Therefore, the pure liquid analyte Raman cross section ( $\sigma_l^a(\nu_0)$ ) can be calculated from the observed Raman intensity ratio ( $I_m^a(\nu_0)/I_m^b(\nu_0)$ ), the concentration ratio ( $N_b/N_a$ ), the refractive indices ( $n_l^a$ ,  $n_m$ ,  $n_l^b$ ) and the pure internal standard Raman cross section  $\sigma_l^b(\nu_0)$ .

$$\sigma_l^a(\nu_0) = \frac{I_m^a(\nu_0)}{I_m^b(\nu_0)} \cdot \frac{N_b}{N_a} \cdot \left[ \frac{(n_l^a/n_m)^2 + 2}{(n_l^b/n_m)^2 + 2} \right]^4 \sigma_l^b(\nu_0) \quad (4-7)$$

### 4.3.2 Chloroform 244 nm UV Raman Cross Section Determination

Fig. 4.3 shows the UV Raman spectra of pure acetonitrile, pure chloroform and a chloroform/acetonitrile mixture (volume ratio, 1:3). The 668 and 918  $\text{cm}^{-1}$  bands derive from the liquid chloroform  $\nu_3$  symmetric stretching mode<sup>32</sup> and the liquid acetonitrile  $\nu_4$  C–C stretching mode,<sup>33</sup> respectively. The measured relative Raman intensity ( $I_m^a(668)/I_m^b(918)= 1.86$ ) was obtained by integrating the Fig. 4.3 Raman bands of the  $\text{CHCl}_3 / \text{CH}_3\text{CN}$  solution (solid line). The aqueous solution 918  $\text{cm}^{-1}$  acetonitrile (3.8 M) Raman cross section was been reported by Asher et al. as  $2.66 \times 10^{-29} \text{ cm}^2/(\text{molc}\cdot\text{sr})$  at 244 nm excitation.<sup>10</sup> Given a calculated 1.382 refractive index of this acetonitrile aqueous solution, close to that of pure acetonitrile, we calculate a similar Raman cross section to that of the pure liquid acetonitrile ( $\sigma_l^b(918)$ ) of  $2.70 \times 10^{-29} \text{ cm}^2/(\text{molc}\cdot\text{sr})$  using eqn. 4-3.

The relative concentration of the chloroform and acetonitrile ( $N_a(668)/N_b(918)=0.215$ ) was calculated from the volume ratio (1:3) and densities (1.474 g/mL for chloroform, 0.787 g/mL for acetonitrile). The refractive indices of chloroform and acetonitrile are 1.53 and 1.39 at 244 nm, respectively.<sup>24, 34</sup> We calculated a solution refractive index of 1.425 at 244 nm. By using

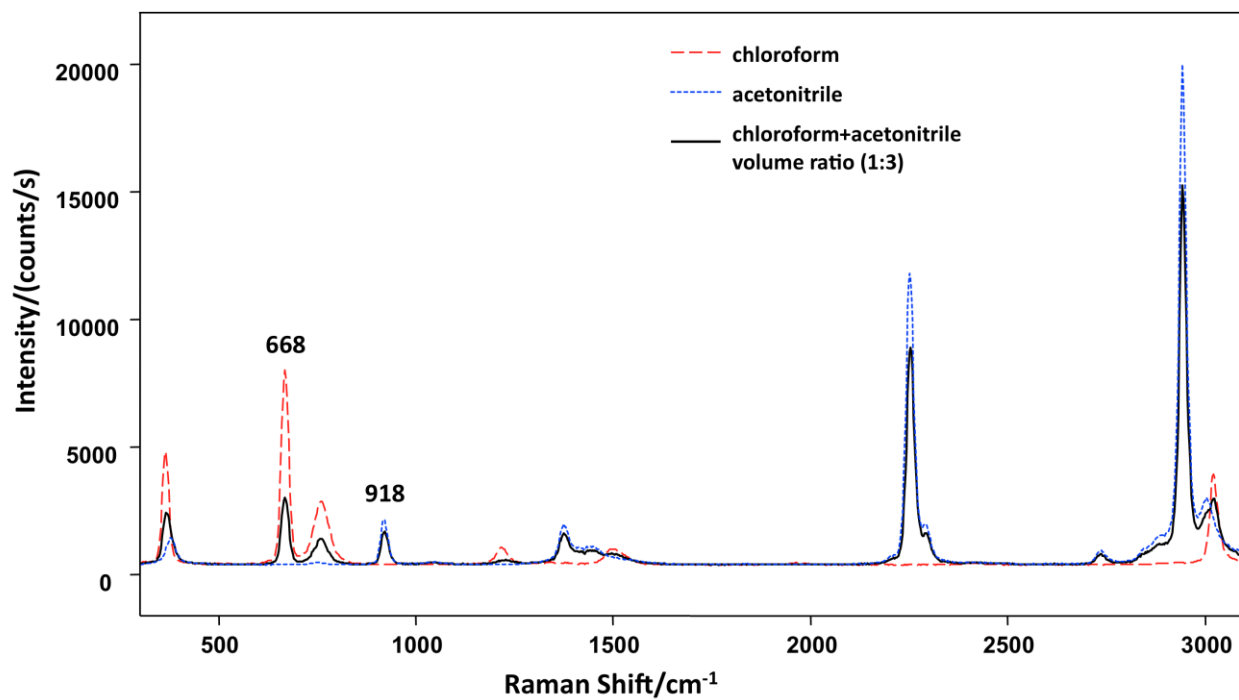


**Figure 4.3** UV Raman spectra of chloroform (dashed line), acetonitrile (dotted line), and chloroform/acetonitrile mixture (volume ratio, 1:3, solid line).

eqn. 4-7, we calculate a pure liquid chloroform 244 nm UV Raman cross section for the 668  $\text{cm}^{-1}$  band of  $\sigma_l^a(668)=3.00\pm 0.09\times 10^{-28} \text{ cm}^2/(\text{mol}\cdot\text{sr})$ .

### 4.3.3 244 nm UV Raman Spectra of Chloroform and $\text{Na}_2\text{SO}_4$ /Chloroform

Fig. 4.4 shows the 244 nm Raman spectra for the  $\text{Na}_2\text{SO}_4$ /chloroform dispersions of  $\text{Na}_2\text{SO}_4$  particles. We calculated  $\text{Na}_2\text{SO}_4$  concentrations of 23.6 mg/mL (mole ratio 1:73.7), 29.8 mg/mL (mole ratio 1:58.1) and 86.6 mg/mL (mole ratio 1:19.6), respectively. The measured relative intensities of the 995  $\text{cm}^{-1}$   $\text{SO}_4^{2-}$  symmetric stretching band to that of the liquid chloroform 668  $\text{cm}^{-1}$  band ( $I_m^a(995)/I_m^b(668)$ ), that were obtained by integrating the Raman bands in Fig. 4.4, increased from 0.0091, to 0.0108, and to 0.0342 as the solid  $\text{Na}_2\text{SO}_4$  concentration increased from 23.6 mg/mL, to 29.8 mg/mL, and to 86.6 mg/mL.

Because of the very similar refractive index of chloroform to that of solid  $\text{Na}_2\text{SO}_4$  at 244 nm, the local field correction factor should be close to 1.0 and will not impact the Raman cross section. We calculate the solid 244 nm UV Raman cross sections for the 995  $\text{cm}^{-1}$   $\text{SO}_4^{2-}$  symmetric stretch band of  $2.01\pm 0.08\times 10^{-28}$ ,  $1.88\pm 0.07\times 10^{-28}$  and  $2.01\pm 0.07\times 10^{-28} \text{ cm}^2/(\text{mol}\cdot\text{sr})$  for these three different sample concentrations respectively, giving an average solid 244 nm UV Raman cross sections for the 995  $\text{cm}^{-1}$   $\text{SO}_4^{2-}$  band of  $1.97\pm 0.07\times 10^{-28} \text{ cm}^2/(\text{mol}\cdot\text{sr})$ . This value is around half of the aqueous Raman cross section of  $3.54\times 10^{-28} \text{ cm}^2/(\text{mol}\cdot\text{sr})$  at 244 nm. The difference is close to the solid and solution  $\text{NaNO}_3$  Raman cross section difference reported by Asher et al.,<sup>23</sup> which is dominated by chemical differences between the solid state and solution state.<sup>23</sup>

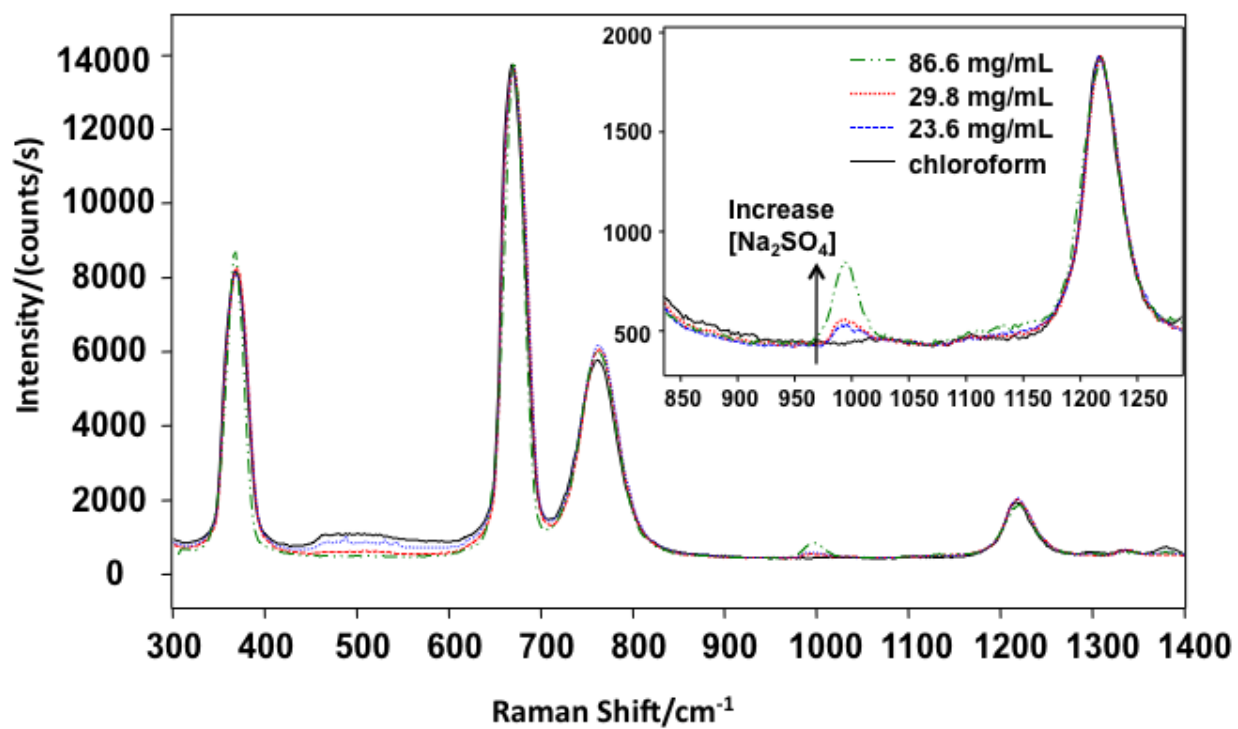


**Figure 4.4** UV Raman spectra of liquid chloroform and chloroform with increasing amounts of solid Na<sub>2</sub>SO<sub>4</sub> particles of 23.6 mg/mL, 29.8 mg/mL, and 86.6 mg/mL. Raman spectra were normalized to the chloroform 668 cm<sup>-1</sup> band.

By using the wavelength dispersion relationship for the solution  $981\text{ cm}^{-1}\text{ SO}_4^{2-}$  band, we can calculate that the 229 nm solid Raman cross section for the  $995\text{ cm}^{-1}\text{ SO}_4^{2-}$  band is  $2.74\times 10^{-28}\text{ cm}^2/(\text{molc}\cdot\text{sr})$  compared to an aqueous solution value of  $4.94\times 10^{-28}\text{ cm}^2/(\text{molc}\cdot\text{sr})$  at 229 nm excitation.<sup>10</sup>

#### 4.3.4 UV Raman Spectra of Acetonitrile and $\text{Na}_2\text{SO}_4$ /acetonitrile

For comparison, we also measured the solid sulfate Raman intensities in a liquid that was not refractive index matched to the solid particles. Fig. 4.5 shows the 244 nm UV Raman spectra of solid  $\text{Na}_2\text{SO}_4$  dispersed in pure acetonitrile containing  $\text{Na}_2\text{SO}_4$  particles at concentrations of 19.4 mg/mL (mole ratio 1:136.6), 29.0 mg/mL (mole ratio 1:90.6) and 52.1 mg/mL (mole ratio 1:48.8). Fig. 4.5 also shows the neat acetonitrile spectrum. The increasing stray light background observed between  $400$  and  $800\text{ cm}^{-1}$  indicates that elastic scattering is increased as the solid sulfate concentration increases in this non-refractive-index-matched solution. As the  $\text{Na}_2\text{SO}_4$  particle concentration increases, the integrated relative Raman intensity ratio  $I_m^a(995)/I_m^b(918)$  increases from 0.0347, 0.0572 to 0.118.

Unlike the dissolved solution, for the  $\text{Na}_2\text{SO}_4$  particle/acetonitrile dispersion both the acetonitrile and solid  $\text{Na}_2\text{SO}_4$  molecules are in their own pure phases with their particular refractive indices. Therefore, eqn. 4-7 becomes independent of the refractive indices, and we calculate solid state  $995\text{ cm}^{-1}\text{ SO}_4^{2-}$  band 244 nm Raman cross sections of  $1.28\pm 0.04\times 10^{-28}$ ,  $1.40\pm 0.04\times 10^{-28}$  and  $1.55\pm 0.05\times 10^{-28}\text{ cm}^2/(\text{molc}\cdot\text{sr})$  as the  $\text{Na}_2\text{SO}_4$  particle concentration increases. The average solid 244 nm UV Raman cross sections for the  $995\text{ cm}^{-1}\text{ SO}_4^{2-}$  band is  $1.41\pm 0.14\times 10^{-28}\text{ cm}^2/(\text{molc}\cdot\text{sr})$ . This value is about 30% smaller than that found for solid  $\text{Na}_2\text{SO}_4$

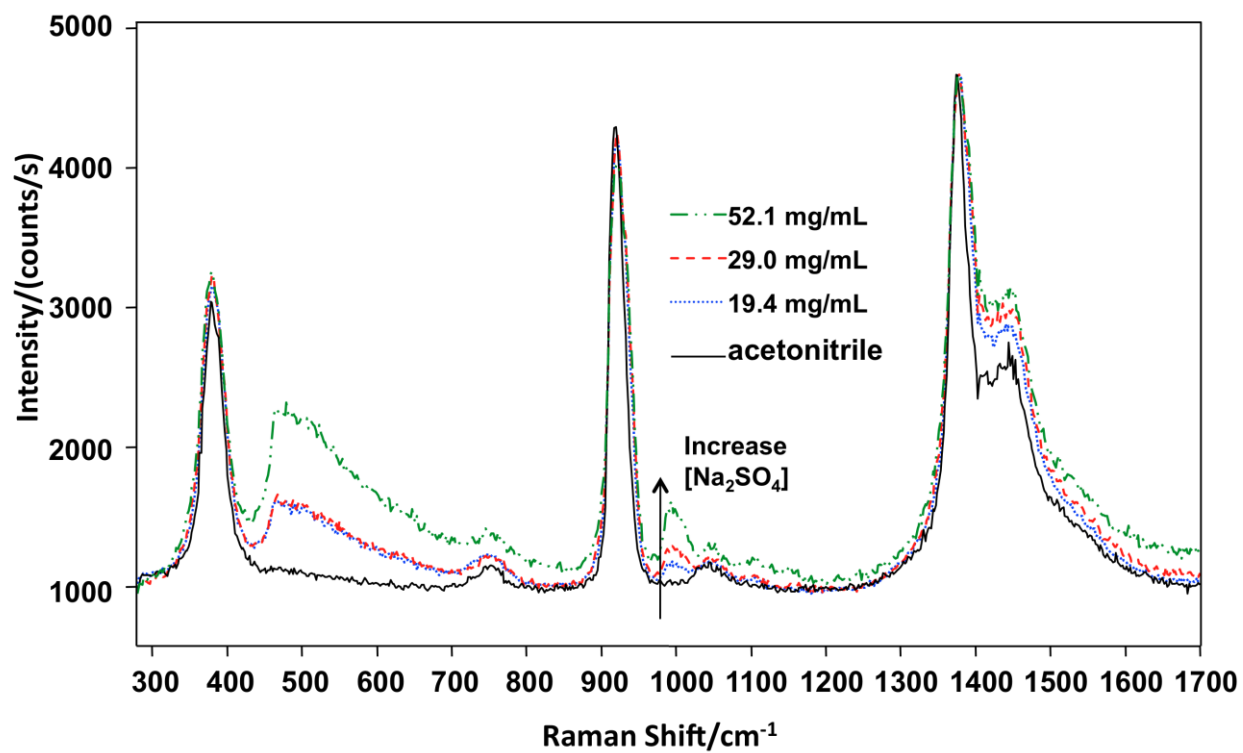


**Figure 4.5** UV Raman spectra of liquid acetonitrile and acetonitrile with increasing amounts of solid Na<sub>2</sub>SO<sub>4</sub> particles of 19.4 mg/mL, 29.0 mg/mL, and 52.1 mg/mL. Raman spectra were normalized to the acetonitrile 1375 cm<sup>-1</sup> band.

in chloroform. This decrease results from less penetration of the exciting light into the  $\text{Na}_2\text{SO}_4$  particles because of the interface scattering of the incident light due to the refractive index difference between solid  $\text{Na}_2\text{SO}_4$  and the acetonitrile.

We conclude that the refractive index-matching method used here is a fast and convenient method to determine solid particle Raman cross sections because it avoids both the local field correction and interface scattering. In cases where a single solvent doesn't match the solid analyte's refractive index, one could use mixed solvents to match the refractive index and use the local field correction method.

#### 4.4 CONCLUSIONS

We demonstrated a refractive-index matching method for determining the solid state  $\text{Na}_2\text{SO}_4$  particle 244 nm UV Raman cross section. The 244 nm UV Raman cross section of liquid chloroform was measured by using acetonitrile as an internal standard. The 244 nm Raman cross section of liquid chloroform was found to be  $3.00 \pm 0.09 \times 10^{-28} \text{ cm}^2/(\text{molc}\cdot\text{sr})$ . We then used liquid chloroform as an internal standard to determine that the solid  $\text{Na}_2\text{SO}_4$  244nm UV Raman cross section of the  $995 \text{ cm}^{-1}$  symmetric stretching band is  $1.97 \pm 0.07 \times 10^{-28} \text{ cm}^2/(\text{molc}\cdot\text{sr})$ . This is the first report of a method to measure nonabsorbing solid UV Raman cross section that avoids interface-scattering bias.

We also measured a 30% smaller value for the solid  $995 \text{ cm}^{-1}$   $\text{Na}_2\text{SO}_4$  Raman cross sections when we attempted to use non refractive-index matched acetonitrile. This 30% decrease results from the  $\text{Na}_2\text{SO}_4$  particle interface scatterings.

The refractive index matching method provides a simple and accurate way to determine the solid state particle Raman cross sections, avoiding the use of the local field corrections and avoiding interface scattering bias. This method is useful for accurate determination of solid state Raman cross sections.

#### 4.5 ACKNOWLEDGEMENT

We appreciate partial funding of this work by the West Virginia High Technology Consortium Foundation under contract number HSHQDC-09-C-00159 from the Department of Homeland Security Science and Technology Directorate. We also thank Hong Zhang from Dr. Weber's group at University of Pittsburgh for the help on the optical imaging of ground solid Na<sub>2</sub>SO<sub>4</sub> particles.

#### 4.6 REFERENCES

1. Lewis, I. R.; Edwards, H. G. M. *Handbook of Raman spectroscopy: from the research laboratory to the process line*; Marcel Dekker, Inc.: New York, 2001, p. 1.
2. Asher, S. A. *Anal. Chem.* **1993**, 65, 59A.
3. Asher, S. A. *Anal. Chem.* **1993**, 65, 201A.
4. Penney, C. M.; Goldman, L. M.; Lapp, M. *Nat. Phys. Sci.* **1972**, 235, 110.
5. Kato, Y.; Takuma, H. *J. Opt. Soc. Am.* **1971**, 61, 347.

6. Hughes, L. J.; Steenhoek, L. E.; Yeung, E. S. *Chem. Phys. Lett.* **1978**, 58, 413.
7. Schomacker, K. T.; Delaney, J. K.; Champion, P. M. *J. Chem. Phys.* **1986**, 85, 4240.
8. Trulson, M. O.; Mathies, R. A. *J. Chem. Phys.* **1986**, 84, 2068.
9. Kincaid, B. E.; Fontana, J. R. *Appl. Phys. Lett.* **1976**, 28, 12.
10. Dudik, J. M.; Johnson, C. R.; Asher, S. A. *J. Chem. Phys.* **1985**, 82, 1732.
11. Asher, S. A.; Johnson, C. R. *J. Phys. Chem.* **1985**, 89, 1375.
12. Asher, S. A.; Ludwig, M.; Johnson, C. R. *J. Am. Chem. Soc.* **1986**, 108, 3186.
13. Asher, S. A.; Murtaugh, J. L. *Appl. Spectrosc.* **1988**, 42, 83.
14. Lorentzen, J. D.; Guha, S.; Menéndez, J.; Giannozzi, P.; Baroni, S. *Chem. Phys. Lett.* **1997**, 270, 129.
15. Chi Z., Asher, S. A. *J. Phys. Chem. B* **1998**, 102, 9595.
16. Tian, Y.; Zuo, J.; Zhang, L.; Li, Z.; Gao, S.; Lu, G. *Appl. Phys. B* **2007**, 87, 727.
17. Shim, S.; Stuart, C. M.; Mathies, R. A. *ChemPhysChem* **2008**, 9, 697.
18. Colles, M. J.; Griffiths, J. E. *J. Chem. Phys.* **1972**, 56, 3384.
19. Abe, N.; Wakayama, M.; Ito, M. *J. Raman Spectrosc.* **1977**, 6, 38.
20. Emmons, E. D.; Fountain III, A.W.; Guicheteau, J. A.; Christesen, S. D. *XXII International Conference on Raman Spectroscopy AIP Conference Proceedings* **2010**, 1267, 508.
21. Emmons, E. D.; Guicheteau, J. A.; Fountain III, A. W.; Christesen, S. D. "Comparison of Absolute Raman Cross Sections of Explosives in Solution and in the Solid State", *Appl. Spectrosc.* (in preparation).
22. Nagli, L.; Gaft, M.; Fleger, Y.; Rosenbluh, M. *Opt. Mater.* **2008**, 30, 1747.

23. Wang, L.; Tuschel, D.; Asher, S. A. *J. Phys. Chem. C* **2011**, 115, 15767.
24. Samoc, A. *J. Appl. Phys.* **2003**, 94, 6167.
25. Smith, B. W.; Fan, Y.; Slocum, M.; Zavyalova, L. *Optical Microlithography XVIII. Proceedings of the SPIE* **2005**, 5754, 141.
26. Asher, S. A.; Bormett, R. W.; Chen, X. G., Lemmon, D. H.; Cho, N.; Peterson, P.; Arrigoni, M.; Spinelli, L.; Cannon, J. *Appl. Spectrosc.* **1993**, 47, 628.
27. Tuschel, D. D.; Mikhonin, A.V.; Lemoff, B. E.; Asher, S. A. *Appl. Spectrosc.* **2010**, 64, 425.
28. Nestor, J. R.; Lippincott, E. R. *J. Raman Spectrosc.* **1973**, 1, 305.
29. Eckhardt, G.; Wagner, W. G. *J. Mol. Spectrosc.* **1966**, 19, 407.
30. Mirone, P. *Spectrochimica Acta* **1966**, 22, 1897.
31. Fini, G.; Mirone P.; Patella, P. *J. Mol. Spectrosc.* **1968**, 28, 144.
32. Rao, M. V. *Proceedings Mathematical Sciences* **1946**, 24, 510.
33. Loewenschuss A.; Yellin, N. *Spectrochimica Acta* **1975**, 31A, 207.
34. Krivacic, J. R.; Urry, D. W. *Anal. Chem.* **1970**, 42, 596.

## 5.0 FABRICATION OF SILICA SHELL PHOTONIC CRYSTALS THROUGH FLEXIBLE CORE TEMPLATES

(This chapter was published in the *Chemistry of Materials* 2009, 21, 4608-4613. The coauthors are Luling Wang and Sanford A. Asher.)

We attached very small silica particles onto flexible monodisperse poly (*N*-isopropylacrylamide, PNIPAm) core particles synthesized by dispersion polymerization. These silica particles were attached to the partially swollen PNIPAm particles by the hydrolysis and condensation of tetraethoxysilane at 24 °C. The resulting silica particle-functionalized PNIPAm core particles show reversible swelling and shrinking as the temperature is cycled. These particles form close-packed-array photonic crystals as the solvent evaporates; the cores shrink to form a silica shell around the pure PNIPAm dry core particles as they close pack. The PNIPAm cores were removed by calcination, leaving a PC composed of essentially pure continuous silica shells. These silica shell photonic crystals Bragg diffract UV light at ~310 nm. The close packed particle interstices are continuous and are easily filled by water. In contrast, the silica shells are impervious to water because the process of making them results in a continuous shell of silica without holes.

## 5.1 INTRODUCTION

Developing synthetic methodologies to fabricate monodisperse nano and mesoscale materials is important because these materials can be used as the building blocks for novel complex and smart materials such as catalysts,<sup>1</sup> drug delivery materials<sup>2</sup> and photonic crystals (PCs).<sup>3-13</sup> It would be especially useful if these building blocks could self-assemble into functional devices.<sup>5-8</sup>

PC materials are of great technological interest because they can be used to control the propagation of light, for example, in future photonic circuitry.<sup>14-16</sup> In the simplest cases PCs will possess one dimensional periodicities which will result in photonic bandgaps for specific spectral intervals at specific angles that meet the Bragg condition.<sup>5-8</sup> Light at wavelengths and angles that meet the Bragg diffraction condition cannot propagate through PC materials. The PC diffraction efficiencies, the diffraction wavelengths and the diffraction bandwidths depend upon the periodicity of the PC refractive index modulation and the modulation depth.<sup>16, 17</sup>

Much of the work in photonic crystals has utilized materials made from colloidal particles. In this case the important parameters include the particle refractive index, its diameter and the particle morphology.<sup>18-21</sup> Some particle array crystal structures, such as the inverse face centered cubic (fcc) structure permit the PC to possess 3-D photonic bandgaps if a sufficiently large refractive index contrast occurs between the sphere air holes and the interstitial spaces.<sup>22-25</sup>

There is an extensive literature describing methods to synthesize the simplest monodisperse building blocks of PC, which are colloidal spheres of specific size possessing particular surface functionalities.<sup>26-29</sup> These monodisperse colloidal particles can be composed of polymer<sup>28</sup> or inorganic<sup>29</sup> or metallic materials.<sup>30</sup> In addition, more complex spherical colloidal particles have been synthesized which contain nanoscopic inclusions such as semiconductor quantum dots, as well as silver, gold and other quantum dots.<sup>6, 31, 32</sup> These particles can form

close-packed PCs through various methods of packing such as slow sedimentation and solvent evaporation,<sup>33</sup> centrifugation,<sup>34</sup> spin coating<sup>35</sup> and convective self-assembly.<sup>36</sup>

Alternatively, charged colloidal particles have been synthesized whose surfaces are functionalized by strong acid groups.<sup>5-8</sup> These charged particles in pure water readily self-assemble into highly-ordered crystalline colloidal arrays (CCA) PCs.<sup>5-8</sup>

The next level of complexity for colloidal particle building blocks would utilize additional design degree of freedoms enabled by the use of particles which consist only of hollow spherical shells.<sup>5, 18-21</sup> The diffraction properties could be controlled by modifying the colloidal particle shell thickness, as well as by controlling the refractive index of materials which are diffused into the cores of the hollow spherical shells.<sup>19-21, 37</sup> In addition, the shell material could be replaced by air to form air shell complex PC structures.

We have been working on developing PC composed of shells of colloidal particles. We were among the first to synthesize monodisperse hollow spherical polystyrene shell particles and were the first to form PCs from hollow particles.<sup>5</sup> We prepared monodisperse core-shell particles by polymerizing a polystyrene shell around a silica core. Etching away the silica core resulted in hollow monodisperse polystyrene particles. A major limitation was that the polystyrene shell was flexible like a balloon and could collapse to form bowl shaped structures. Other synthetic approaches have fabricated more structurally rigid shells out of silica and titania etc.<sup>18, 38-47</sup>

Caruso et al.<sup>38-40</sup> utilized a layer-by-layer self-assembly technique to coat submicrometer spherical polymer particles with silica nanoparticles. The polymer core was then removed by dissolution or calcination to create hollow particles. Hollow silica spheres were also synthesized through the hydrolysis and condensation of tetraethoxysilane (TEOS) on the surface of polystyrene particles<sup>41</sup> or on ZnS particles.<sup>42</sup> The core was then removed to produce hollow

spherical silica shells. Wong et al.<sup>43</sup> reported a room-temperature, wet chemical-based synthesis route in which silica and gold nanoparticles were cooperatively assembled with lysine-cysteine diblock copolypeptides into robust hollow spheres. Chen et al.<sup>44, 45</sup> reported a technique to fabricate hollow silica shells and hollow titania shells via a one-step process where the polystyrene core particles dissolved as the silica shell condensed. Yin et al.<sup>46</sup> reported the spontaneous transformation of silica colloids from solid particles to hollow spheres in the presence of NaBH<sub>4</sub>.

In addition, Colvin et al.<sup>18</sup> reported a “lost-wax” method that grew colloidal particle shells within an inverse opal template. Xia et al.<sup>47</sup> prepared mesoscale hollow spheres of TiO<sub>2</sub> and SnO<sub>2</sub> by templating their sol-gel condensation products within a crystalline array of monodisperse polystyrene particles.

Small ~30 nm hollow spherical rigid shells have been synthesized by using of polymeric micelles.<sup>48</sup> The advantages of flexible micelles or microgels are that the size and morphology of the particles can be easily tuned by adjusting the solution temperature, ionic strength, and solvent composition.<sup>49</sup>

In the work here we demonstrate the synthesis of monodisperse silica shells around a flexible PNIPAm colloidal particle core. We first attach very small silica particles onto the exterior of swollen PNIPAm particles. PNIPAm is a well-known polymer that is highly swollen in water below its lower critical solution temperature (LCST). Above this temperature, it undergoes a reversible volume phase transition to a collapsed, dehydrated state.<sup>7</sup> The swollen PNIPAm core particles are utilized as a highly elastic and soft template. As solvent is evaporated from a dispersion of these monodisperse core-shell particles, the PNIPAm cores shrink and the silica particles on the surface form a silica shell. During this process, the core-shell particles self-

assemble into a close-packed array PC. The system is further condensed as the core is removed by calcination at high temperature.

## 5.2 EXPERIMENTAL SECTION

### 5.2.1 Preparation of monodisperse PNIPAm core particles

PNIPAm nanoparticles were synthesized by dispersion polymerization. 1.4 g NIPAm, 2.0 g polyvinylpyrrolidone (PVP40), 0.066 g N, N'-methylenebisacrylamide (BIS) were dissolved in 95 mL water and bubbled with nitrogen gas for 0.5 hr. A 0.2 g portion of  $\alpha$ ,  $\alpha'$ -azodiisobutyramidine dihydrochloride (AIBA, initiator, Fluka) was dissolved in 5 mL water and bubbled with nitrogen gas before addition. The polymerization was carried out at 70 °C for 6 h under a nitrogen atmosphere, and then, the reaction mixture was cooled to room temperature while stirring. The particle solution was filtered through glass wool and dialyzed for 14 days by using 10,000 MWCO dialysis tubing (Pierce). Water was changed three times a day. The particles were characterized by both transmission electron microscopy (TEM) and dynamic light scattering (DLS).

### 5.2.2 Preparation of PNIPAm-silica core-shell particles

The silica coating process was carried out by hydrolysis and condensation of TEOS on the surface of the PNIPAm nanoparticles by using either of two different recipes. In the first example, 1.0 mL of a PNIPAm (0.80 wt %) particle dispersion was added to 9 mL water under

stirring. The mixture was adjusted to pH 11.0 with ammonium hydroxide. Thirty microliters TEOS was added to the solution under stirring. The reaction was continued for 4 h at 24 °C, and the resulting particles were characterized by TEM. The second recipe was the same except that the pH was initially adjusted to 8.0 with ammonium hydroxide. The temperature dependence of the core-shell particle was characterized by DLS.

### **5.2.3 Fabrication of silica shell PC**

The PNIPAm-silica core-shell particle dispersion was dried overnight at 90 °C to form a close packed PC. Then the sample was heated at 250 °C for 4 h and at 450 °C overnight to remove the PNIPAm core. The samples were redispersed in water and then characterized by scanning electron microscopy (SEM) and TEM. The reflectance spectrum was taken on microspectrophotometer (Craic Technologies, Inc., QDI 2010). The microscope objective was a Davin reflecting objective 15×, NA 0.28.

### **5.2.4 Characterization**

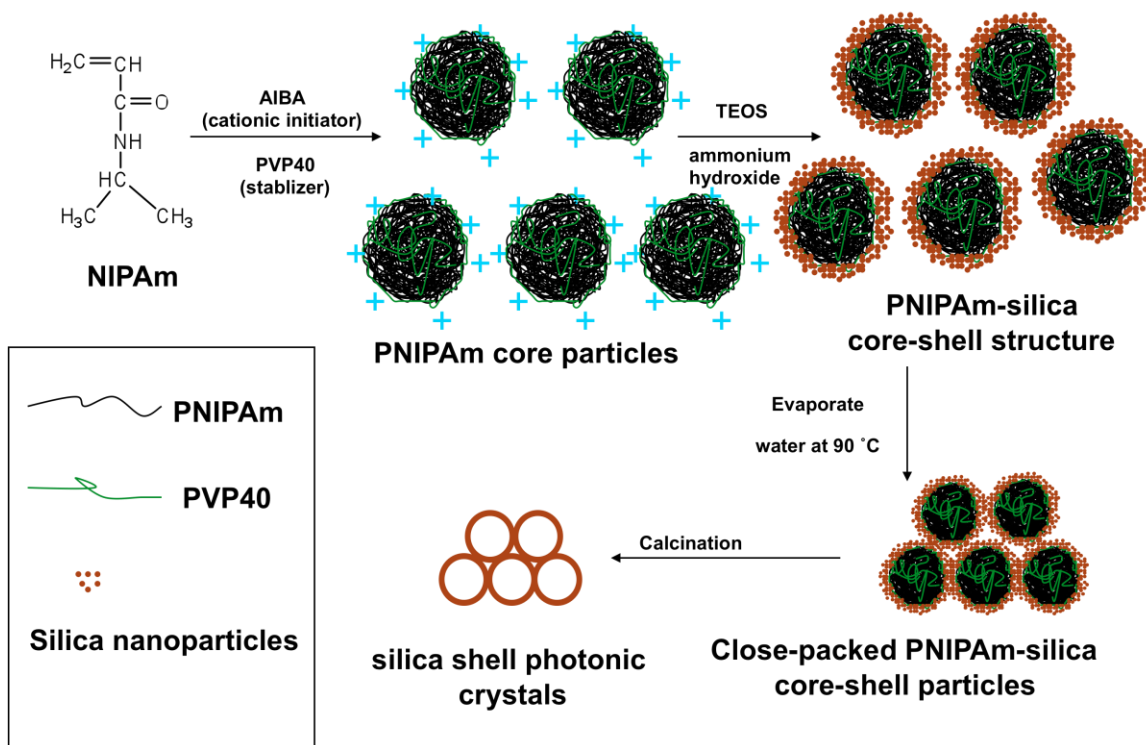
For TEM measurements, a few drops of a dilute dispersion of the nanoparticles were dried on a carbon-coated copper grid (Ted Pella, Inc.) and observed by Philips Mogagni 268 TEM. Samples for SEM were sputter-coated with palladium. SEM studies were performed on Phillips FEG XL-30 FESEM. DLS was measured by using a Brookhaven Corp. ZetaPALS.

### 5.3 RESULTS AND DISCUSSION

Our objective in this work was to synthesize a silica shell close-packed PC. To accomplish this, we needed to form a flexible silica precursor shell which would survive the ultimate removal of the core. To accomplish this, we developed a synthesis of a flexible PNIPAm nanogel core which during the silica condensation was swollen where silica particles attached to the exterior hydrogel surface. We expected that as the system self-assembled into the final close packed array the PNIPAm particles would shrink to assemble a fully dense silica shell.

The route for the fabrication of silica shell photonic crystals is shown in Scheme 5.1. Monodisperse PNIPAm colloidal particles were synthesized by dispersion polymerization. These PNIPAm colloidal particles were then coated with a silica shell. The resulting monodisperse PNIPAm-silica core-shell particles self-assembled into a close-packed PC as the solvent evaporated. Heating decomposed and vaporized the PNIPAm cores, leaving a PC composed of a close-packed array of silica shells that diffracted light.

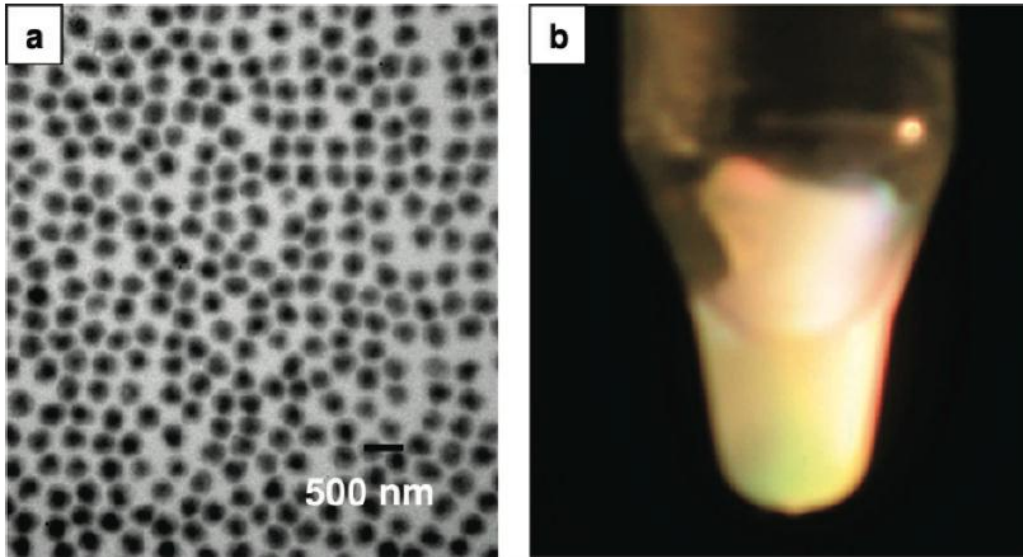
We originally tried to utilize the negatively charged, monodisperse PNIPAm nanoparticles we previously synthesized<sup>7, 8</sup> which readily self-assemble into CCA. However, we were unable to fabricate a silica shell on the surface of these PNIPAm particles, presumably because the silica particles are also negatively charged through the ionization of surface silanol groups.



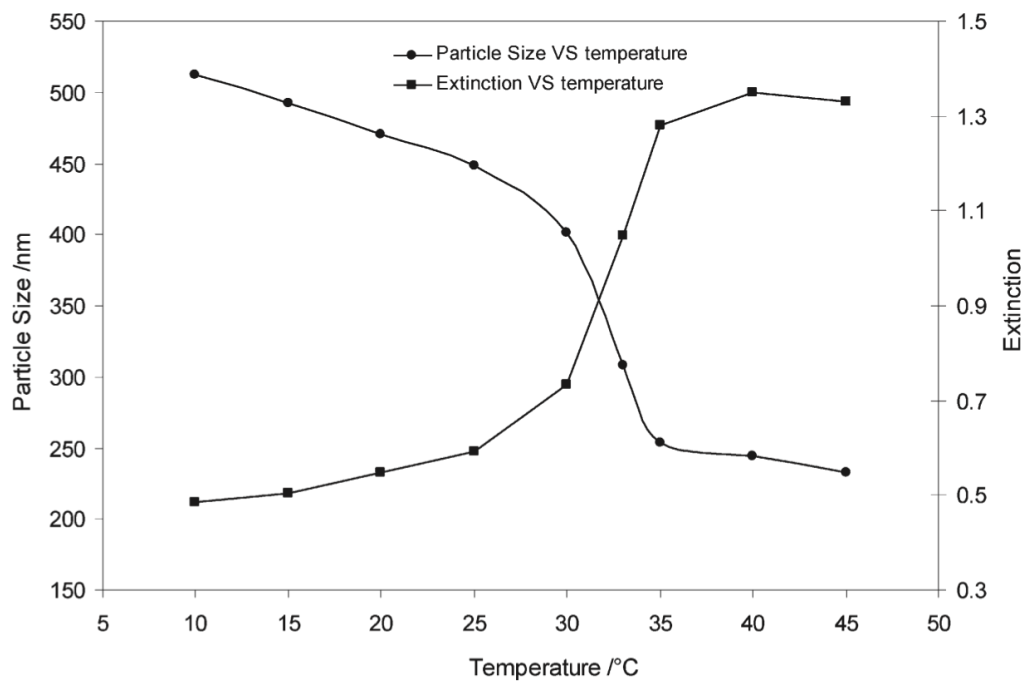
**Scheme 5.1** Preparation of Silica shell Photonic Crystals.

Thus, we instead synthesized positively charged PNIPAm core particles by using the cationic initiator AIBA. In addition, we used the amphiphilic polymer PVP40 instead of anionic sodium dodecyl sulfate (SDS) as a stabilizer during the polymerization. The polymerization process is similar to that described elsewhere.<sup>44, 50</sup> Fig. 5.1a shows a TEM image of the monodisperse PNIPAm core particles with diameters measured by TEM and DLS of  $294 \pm 25$  nm and  $453 \pm 4$  nm (at 24 °C). The TEM particle size is much smaller than that from DLS due to shrinkage during the drying process. Bragg diffraction iridescence was observed when the particles were centrifuged at 12000 g for 1 h at 24 °C (Fig. 5.1b).

Fig. 5.2 shows that the diameter of the PNIPAm core colloids decreases from ~512 nm at 10 °C to ~244 nm at 40 °C due to the well-known volume phase transition which shows an LCST<sup>49</sup> of ~32 °C. The turbidity of a dilute unordered dispersion of the PNIPAm core colloids increases as the diameter decreases due to the increased refractive index of the smaller particles.<sup>7</sup>



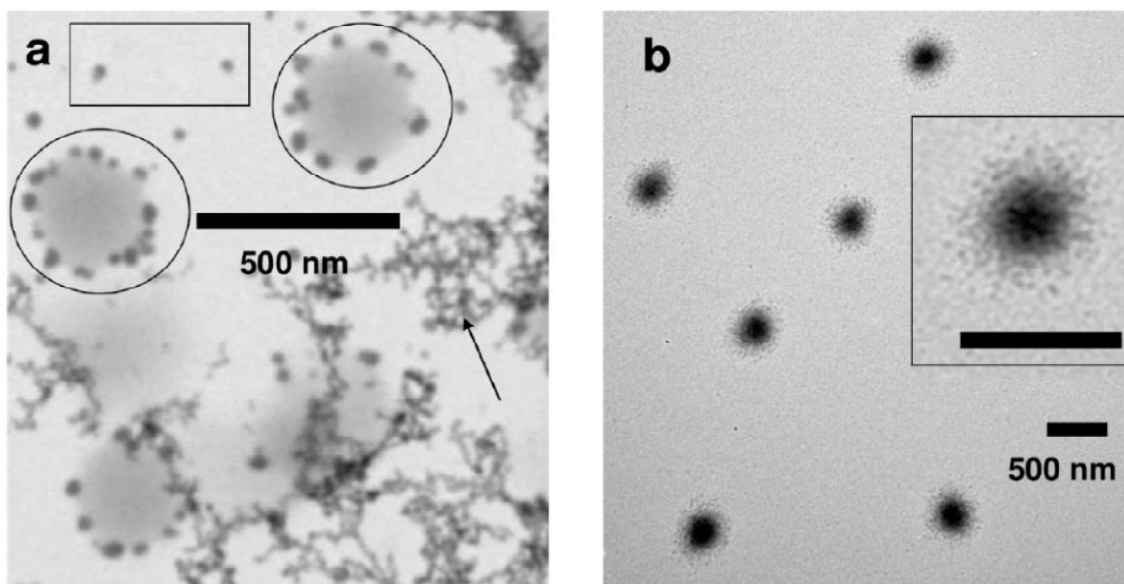
**Figure 5.1** (a) TEM image of PNIPAm core particles. (b) Photograph of Bragg diffraction from PNIPAm core particles.



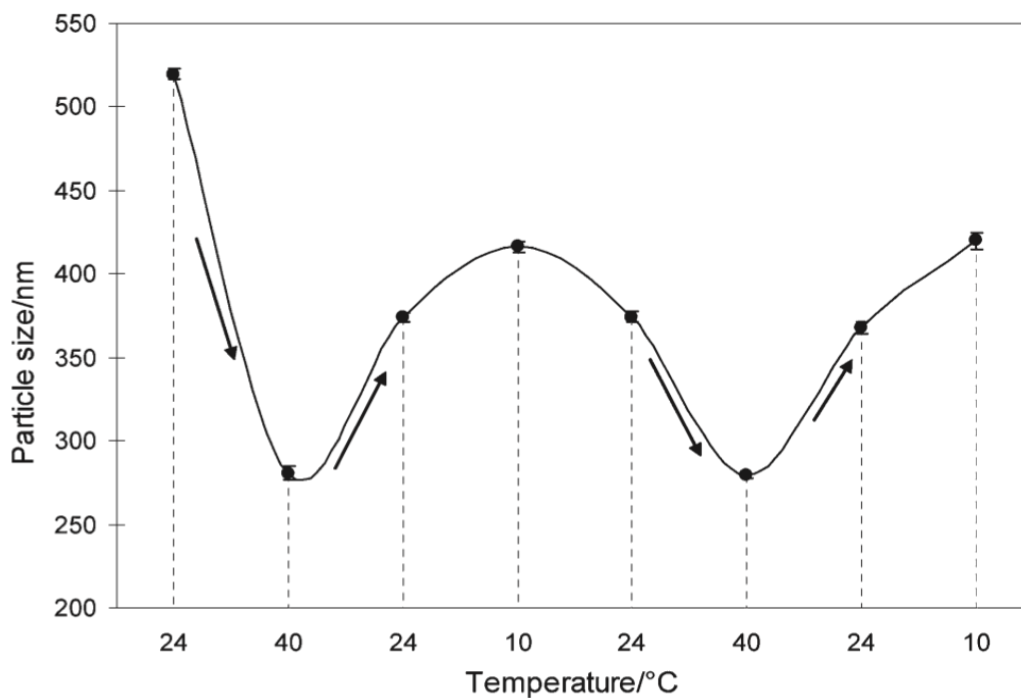
**Figure 5.2** Temperature dependence of diameter and turbidity of PNIPAm Particles.

To coat the PNIPAm with silica, we utilized a modified Stöber process. A typical reaction mixture contained TEOS as the silica precursor, ammonium hydroxide as the catalyst and water as the reaction solvent. The silica coatings were performed either at pH 11.0 or pH 8.0. Fig. 5.3a shows that at pH 11.0 the PNIPAm core particles were coated with small 20~40 nm silica particles. In addition, other silica aggregates (as indicated by the arrow) and free silica particles (within the rectangle) also form in solution. Fig. 5.3b shows that by slowing the hydrolysis rate by decreasing the pH to 8.0 we obtain monodisperse PNIPAm-silica core-shell particles with a diameter of  $456 \pm 24$  nm and a silica shell thickness of  $\sim 80$  nm. Iridescence of this sample was also observed (similar to Fig. 5.1b) after centrifugation.

Fig. 5.4 shows the temperature dependence of apparent diameter of the PNIPAm-silica core-shell particles. After silica coating, the particle has a diameter of  $520 \pm 3$  nm (at  $24^\circ\text{C}$ ) which is about 70 nm larger than that of original PNIPAm core particles at  $24^\circ\text{C}$  ( $453 \pm 4$  nm). As the temperature increases to  $40^\circ\text{C}$ , the core-shell particle diameter decreases to  $280 \pm 4$  nm. This diameter is also about 40 nm larger than that of the PNIPAm core particles ( $244 \pm 2$  nm at  $40^\circ\text{C}$ ). After heating to  $40^\circ\text{C}$  during the first temperature cycle, the core-shell particle diameter does not fully return to its original diameter; at  $24^\circ\text{C}$  it has a 28 % decreased diameter of  $374 \pm 3$  nm. The silica shell prevents the full expansion of the core-shell particle. Further temperature cycles show continued reversible expansions and contractions of this core shell particle.



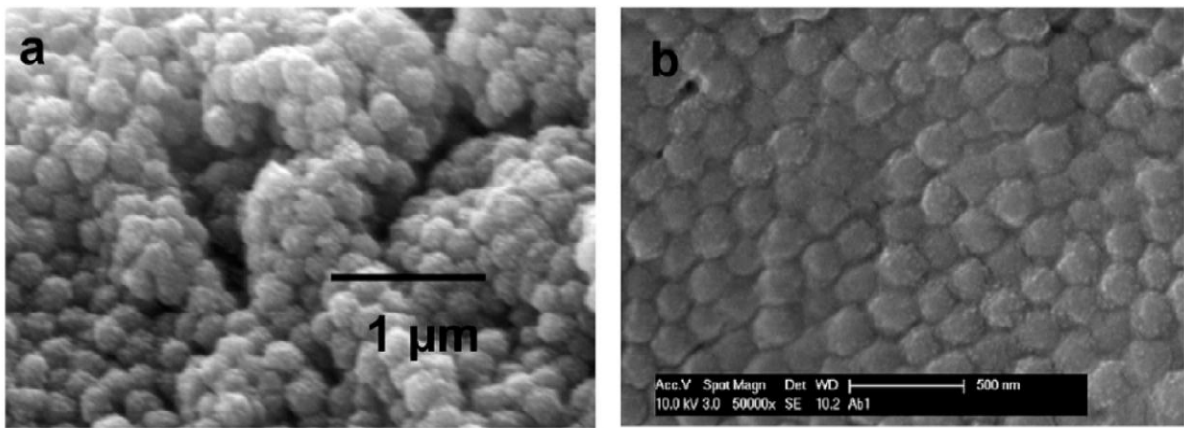
**Figure 5.3** TEM of PNIPAm core particles after silica coating at (a) pH11.0 and (b) pH 8.0 (the inset shows a core-shell particle at higher magnification; the scale bar is 500 nm).



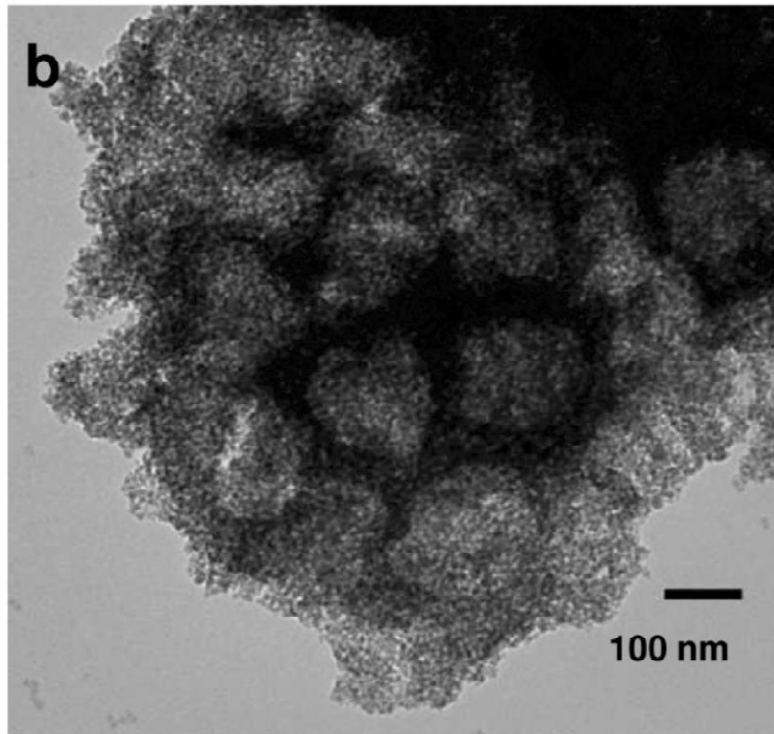
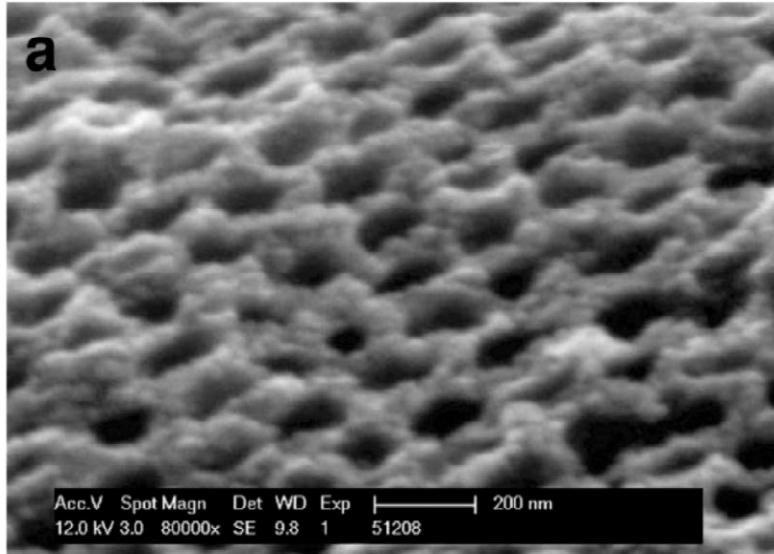
**Figure 5.4** Temperature dependence of the DLS measured apparent particle diameter of the PNIPAm-silica core-shell particles (solid line drawn to help the eye).

Fig. 5.5a shows SEM of 210 nm diameter unordered PNIPAm-silica core-shell particles formed by slow sedimentation followed by drying in air. By carefully controlling the temperature and slowly evaporating water,<sup>33</sup> we fabricated an ordered, close-packed structure as shown in Fig. 5.5b. If the image of the particles is magnified, numerous small white dots appear which derive from the silica particles on the surface of the PNIPAm cores.

Fig. 5.6a shows SEM of the ordered hollow close packed silica shell structure formed after removal of the polymer core by calcination. Ordered hollow silica structures can be clearly observed. Fig. 6b shows a TEM of a very thin evaporated sample where the individual silica shells can be discerned. The diameter of the hollow core measured by both TEM and SEM is ~140 nm. This diameter is much less than that measured for the pure shrunken PNIPAm particles, presumably because the silica shell further collapses upon calcination. We measure a ~15 nm shell thickness by using TEM and SEM.



**Figure 5.5** SEM of (a) unordered and (b) ordered close-packed silica-shell/ PNIPAm-core particles.



**Figure 5.6** (a) SEM image of the cross section of silica shell photonic crystals.  
(b) TEM image of the silica shell photonic crystals.

Fig. 5.7 shows the reflectance spectrum of these close-packed silica shell PCs measured at normal incidence by using a microspectrophotometer. The reflectance peaks in Fig. 5.7 result from Bragg diffraction from the ordered structure<sup>51</sup> of the silica shell PCs. We assume that the silica shells arrange in an ideal fcc close-packed array where the volume fraction composed of the silica shells and hollow cores is 0.74. This leaves the interstitial space volume fraction to be 0.26.

We measured the diffraction for the dried PC as well as for the same PC immersed in water. We expected a large diffraction red shift due to the increase in refractive index due to the expected increase in water volume fraction. In contrast, Fig. 5.7 shows little shift of the diffraction peak wavelength between air (~306 nm) and water (~321 nm) which indicates only a ~5 % increase in refractive index. Apparently, water cannot penetrate to the cores.

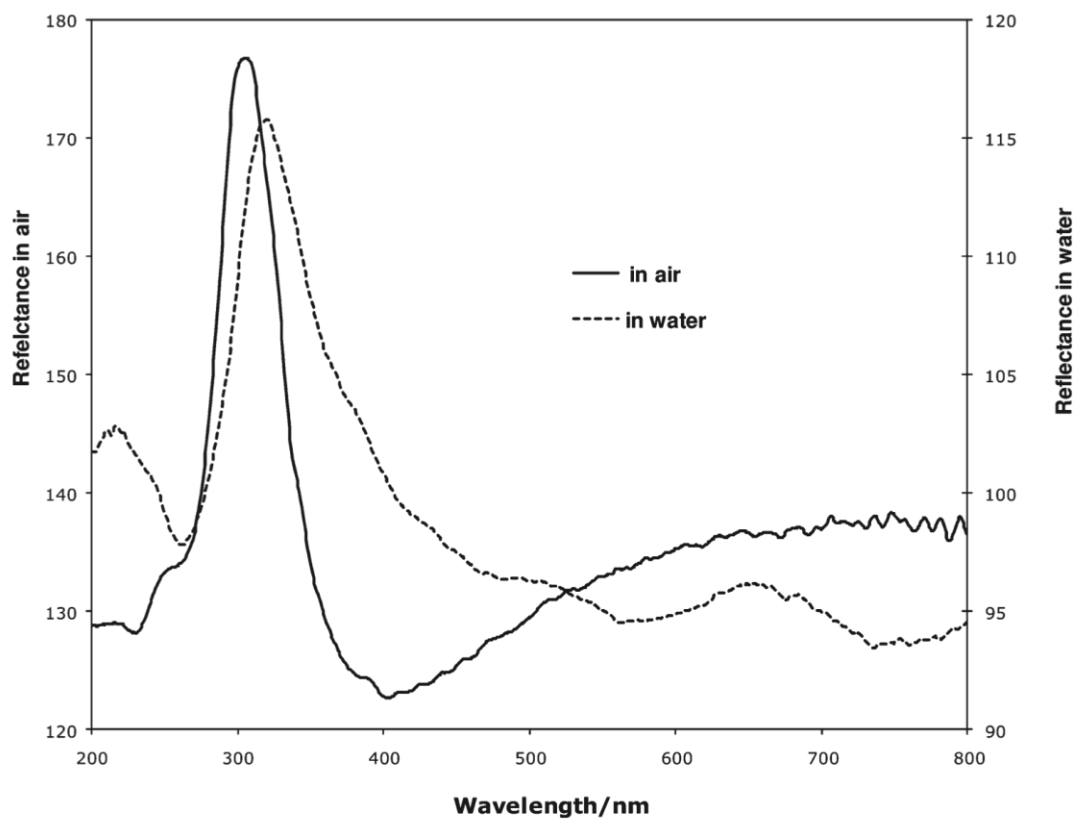


**Figure 5.7** Reflectance spectrum of silica shell photonic crystals in air (solid line) and water (dash line).

We calculated the impact of water only filling the interstices from equations 5-1 to 5-3, where  $n_{avg}$  is the average refractive index of the PC which relates the wavelength diffracted,  $\lambda$ , lattice spacing,  $d$ , and glancing angle,  $\theta$ , in Bragg's law:  $\lambda = 2 n_{avg} d \sin\theta$ . Eqn. 5-1 calculates  $n_{avg}$  assuming that water can only fill the interstices but not the cores. The volume fraction of interstices for close packed spherical particles is 0.26.  $n_w$ ,  $n_{SiO_2}$ , and  $n_{air}$  are the refractive indices of the solvent, silica (1.425), and air (1.000),  $\phi_{SiO_2}$  is the volume fraction of silica shells,  $D$  is the outside diameter of the core-shell particles and  $D_i$  is the diameter of the hollow cores.

$$n_{ave} = 0.26n_w + n_{SiO_2}\phi_{SiO_2} + (0.74 - \phi_{SiO_2})n_{air} \quad (5-1)$$

$$\phi_{SiO_2} = \frac{D^3 - D_i^3}{D^3} \cdot 0.74 \quad (5-2)$$

$$\lambda = 2\left(\frac{2}{3}\right)^{\frac{1}{2}} D n_{avg} \quad (5-3)$$

We calculate  $n_{avg} = 1.139$  in air and  $n_{avg} = 1.224$  in water. Thus, we calculate that we will observe a red shift of ~7%, close to that experimentally observed. This indicates that the cores are actually sealed during the calcination process.

## 5.4 CONCLUSIONS

We developed a synthesis to attach silica particles onto flexible monodisperse PNIPAm nanogel core particles. These PNIPAm-silica core-shell particles show reversible swelling and shrinking in water as the temperature is cycled. Slow evaporation of solvent causes these particles to self-assemble into a close packed PC. Calcination removes the PNIPAm particle core leaving a PC composed of a silica shell close packed array which has air both in the interstices as well as in

the cores. The shrinking of the silica shell/PNIPAm core particles during solvent evaporation and calcination seals the cores due to formation of a continuous silica shell. This makes the shells impermeable to water.

## 5.5 ACKNOWLEDGMENT

The authors acknowledge support for this work from the National Institutes of Health NIH grant 1R01EB009089. The authors also thank Dr. Sasha Tikhonov, Jia Luo, and Justin Bohn for many helpful discussions.

## 5.6 REFERENCES

1. Bell, A. T. *Science* **2003**, 299, 1688.
2. Lai, C.; Trewyn, B. G.; Jeftinija, D. M.; Jeftinija, K.; Xu, S.; Jeftinija, S.; Lin, V. *J. Am. Chem. Soc.* **2003**, 125, 4451.
3. Chang, S.; Liu L.; Asher S. A. *J. Am. Chem. Soc.* **1994**, 116, 6739.
4. Chang, S.; Liu L.; Asher S. A. *J. Am. Chem. Soc.* **1994**, 116, 6745.
5. Xu, X.; Asher, S. A. *J. Am. Chem. Soc.* **2004**, 126, 7940.
6. Wang, W.; Asher, S. A. *J. Am. Chem. Soc.* **2001**, 123, 12528.
7. Weissman, J. M.; Sunkara, H. B.; Tse, A. S.; Asher, S. A. *Science* **1996**, 274, 959.

8. Reese, C. E.; Mikhonin, A. V.; Kamenjicki, M.; Tikhonov, A.; Asher, S. A. *J. Am. Chem. Soc.* **2004**, 126, 1493.
9. Nayak, S.; Lyon, L. A. *Angew. Chem. Int. Ed.* **2005**, 44, 7686.
10. Lyon, L. A.; Debord, J. D.; Debord, S. B.; Jones, C. D.; McGrath, J. G.; Serpe, M. *J. Phys. Chem. B* **2004**, 108, 19099.
11. Suzuki D.; McGrath J. G.; Kawaguchi H.; Lyon L. A. *J. Phys. Chem. C* **2007**, 111, 5667
12. Gorelikov I.; Field L. M.; Kumacheva E. *J. Am. Chem. Soc.* **2004**, 126, 15938
13. Suzuki D.; Kawaguchi H. *Langmuir* **2005**, 21, 8175
14. Yablonovitch, E. *Phys. Rev. Lett.* **1987**, 58, 2059.
15. John, S. *Phys. Rev. Lett.* **1987**, 58, 2486.
16. Joannopoulos, J. D.; Johnson, S. G.; Winn, J. N.; Meade, R. D. *Photonic crystals: Molding the Flow of the Light (Second Edition)*; Princeton University: New Jersey, 2008.
17. Joannopoulos, J. D.; Villeneuve, P. R.; Fan, S. H. *Nature* **1997**, 387, 830.
18. Jiang, P.; Bertone, J. F.; Colvin, V. L. *Science* **2001**, 291, 453.
19. Colvin, V. L. *MRS Bull.* **2001**, 26, 637.
20. Rengarajan, R.; Jiang, P.; Colvin, V.; Mittleman, D. *Appl. Phys. Lett.* **2000**, 77, 3517.
21. Busch, K.; John, S. *Phys. Rev. E* **1998**, 58, 3896.
22. Norris, D. J.; Vlasov, Y. A. *Adv. Mater.* **2001**, 13, 371.
23. Miguez, H.; Meseguer, F.; Lopez, C.; Lopez-Tejiera, F.; Sanchez-Dehesa, J. *Adv. Mater.* **2001**, 13, 393.

24. Blanco, A.; Chomski, E.; Grabtchak, S.; Ibisate, M.; John, S.; Leonard, S. W.; Lopez, C.; Meseguer, F.; Miguez, H.; Mondia, J. P.; Ozin, G. A.; Toader, O.; van Driel, H. M. *Nature* **2000**, 405, 437.
25. Zakhidov, A. A.; Baughman, R. H.; Iqbal, Z.; Cui, C.; Khayrullin, I.; Dantas, S. O.; Marti, J.; Ralchenko, V. G. *Science* **1998**, 282, 897.
26. Stöber, W.; Fink, A. *J. Colloid Interface Sci.* **1968**, 26, 62.
27. Krieger, I. M.; O'Neill, F. M. *J. Am. Chem. Soc.* **1968**, 90, 3114.
28. Reese, C. E.; Guerrero, C. D.; Weissman, J. M.; Lee, K.; Asher, S. A. *J. Colloid Interface Sci.* **2000**, 232, 76.
29. Eshuis, A.; Koning, C. A. *J. Colloid Polym. Sci.* **1994**, 272, 1240.
30. Graf, C.; van Blaaderen, A. *Langmuir* **2002**, 18, 524.
31. Murray C. B.; Norris D. J.; Bawendi M. G. *J. Am. Chem. Soc.* **1993**, 115, 8706.
32. Jones, C. D.; Lyon, L. A. *J. Am. Chem. Soc.* **2003**, 125, 460.
33. Miguez, H.; Meseguer, F.; Lopez, C.; Mifsud, A.; Moya, J. S.; Vazquez, L. *Langmuir* **1997**, 13, 6009.
34. Holland, B. T.; Blanford, C. F.; Do, T.; Stein, A. *Chem. Mater.* **1999**, 11, 795.
35. Mihi, A.; Ocana, M.; Miguez, H. *Adv. Mater.* **2006**, 18, 2244.
36. Norris, D. J.; Arlinghaus, E. G.; Meng, L.; Heiny, R.; Scriven, L. E. *Adv. Mater.* **2004**, 16, 1393
37. Blanford, C. F.; Schroden, R. C.; Al-Daous, M.; Stein, A. *Adv. Mater.* **2001**, 13, 26.
38. Caruso, R. A.; Susha, A.; Caruso, F. *Chem. Mater.* **2001**, 13, 400.
39. Caruso, F.; Caruso, R. A.; Mohwald, H. *Chem. Mater.* **1999**, 11, 3309.
40. Caruso, F.; Caruso, R. A.; Mohwald, H. *Science* **1998**, 282, 1111.

41. Tissot, I.; Reymond, J. P.; Lefebvre, F.; Bourgeat-Lami, E., *Chem. Mater.* **2002**, 14, 1325.
42. Velikov, K. P.; van Blaaderen, A. *Langmuir* **2001**, 17, 4779.
43. Wong, M. S.; Cha, J. N.; Choi, K.; Deming, T. J.; Stucky, G. D. *Nano Lett.* **2002**, 2, 583.
44. Chen, M.; Wu, L.; Zhou, S.; You, B. *Adv. Mater.* **2006**, 18, 801.
45. Cheng, X.; Chen, M.; Wu, L.; Gu, G. *Langmuir* **2006**, 22, 3858.
46. Zhang, T.; Ge, J.; Hu, Y.; Zhang, Q.; Aloni, S.; Yin, Y. *Angew Chem.* **2008**, 120, 5890
47. Zhong, Z.; Yin, Y.; Gates, B.; Xia, Y. *Adv. Mater.* **2000**, 12, 206.
48. Khanal, A.; Inoue, Y.; Yada, M.; Nakashima, K. *J. Am. Chem. Soc.* **2007**, 129, 1534.
49. Pelton, R. *Adv. Colloid Interface Sci.* **2000**, 85, 1.
50. Bamnolker, H.; Nitzan, B.; Gura, S.; Margel, S. *J. Mater. Sci. Lett.* **1997**, 16, 1412.
51. Yu, A.; Meiser, F.; Cassagneau, T.; Caruso, F. *Nano Lett.* **2004**, 4, 177.

## **6.0 SUMMARY AND FUTURE WORK**

### **6.1 SUMMARY OF WORK**

We developed facile methods to synthesize new types of CCA particles. We developed novel CCA Bragg diffraction devices for deep UV application based on our newly developed silica CCA. We also demonstrated the utilization of the CCA filter as a Rayleigh rejection filter for UV Raman application. We fabricated silica shell photonic crystals using our newly developed PNIPAm-silica core-shell particles. We fabricated complex stoichiometrically-defined nanoparticles using the defined interstices of the close-packed photonic crystals. We successfully conducted the first resonance Raman cross-section measurements of solids that avoids the biasing of self-absorption using these stoichiometrically defined nanoparticles. We also developed a refractive-index method to determine solid-state  $\text{Na}_2\text{SO}_4$  Raman cross section that avoids local field corrections and particle interface scattering.

## 6.2 FUTURE WORK

### 6.2.1 Future work in the silica CCA deep UV narrow band rejection filter

We have developed efficient silica CCA deep UV Bragg diffraction devices and demonstrated the utility of the CCA filter as a Rayleigh rejection filter in deep UV Raman measurements. Theoretical calculations predict that the silica CCA diffraction will have a FWHM of 2 nm with a transmission of  $\sim 10^{-11}$  at the band center. Currently, our silica CCA filter has not achieved these theoretical values. Future work is needed to improve the ordering of the silica CCA for higher rejection efficiency and narrower full width at half maximum (FWHM). In addition, since the silica CCA is in an aqueous dispersion, mechanical vibration and temperature fluctuation will affect the CCA ordering which cause changes in the diffracted wavelength and efficiency. Future work is also needed to improve the stability of the CCA filter by solidifying the silica CCA into a polymerized CCA (PCCA) while maintaining the efficiency of the CCA Bragg diffraction. The CCA filter will also be very important for the development of hyperspectral imaging and portable deep UV Raman instrumentations.

#### 6.2.1.1 Improvement of the ordering of the silica CCA

In contrast to an atomic system, the colloidal dispersion, inevitably, has some distribution of particle sizes. The polydispersity here is defined as the standard deviation of the colloidal particle size distribution divided by its average particle size. Both theoretical and experimental studies show that the polydispersity can influence the structural ordering,<sup>1</sup> optical properties,<sup>2, 3</sup> crystallization,<sup>4-8</sup> phase transitions,<sup>1, 9, 10</sup> defects,<sup>11</sup> and also the thermodynamic properties<sup>12, 13</sup> of

colloidal dispersions. To crystallize into a CCA, the polydispersity of the colloidal particles should not exceed a critical value that is in the range from 6% to 12%.<sup>4</sup>

Chapter 2 indicated that the highly-charged silica CCA particles have an average diameter of ~ 47 nm with a standard deviation of 5.1 nm. The polydispersity is ~11% (in the range of the critical value of polydispersity), which may be responsible for the difference between the theoretical calculations and experimental results.

The water-in-oil microemulsion method can be used to synthesize highly monodisperse silica particles with a polydispersity less than 5%.<sup>14</sup> We have used the water-in-oil microemulsion method to prepare monodisperse, spherical silica particles with a diameter of  $40.5 \pm 2.9$  nm (polydispersity ~ 7%) as shown in Fig. 6.1. We used the recipe developed by Chang et al..<sup>15, 16</sup> The particle surfaces were functionalized with phosphonate ((3-(trihydroxysilyl)propyl)methylphosphonate) to reduce aggregates.<sup>17</sup> The particle distribution is sensitive to the water/surfactant ratio and water/silane ratio.<sup>15, 16</sup> Therefore, further work is needed to adjust these ratios to prepare narrower size distribution silica particles with less polydispersity (< 5%).

The silica particles prepared by microemulsion need to be charged by functionalizing the surfaces with sulfonate groups so that they could self-assemble into CCA. Because the silica particles are suspended in non-polar solvent during the microemulsion reaction, the silica particles must be transferred into aqueous or alcoholic solution while avoiding irreversible aggregation. We can use the surface functionalization method in Chapter 2 to increase the surface charge of these silica particles. We expect that these highly-charged, highly-monodisperse silica particle will show better CCA ordering. Optically, we expect to see narrower and deeper Bragg diffraction bands.

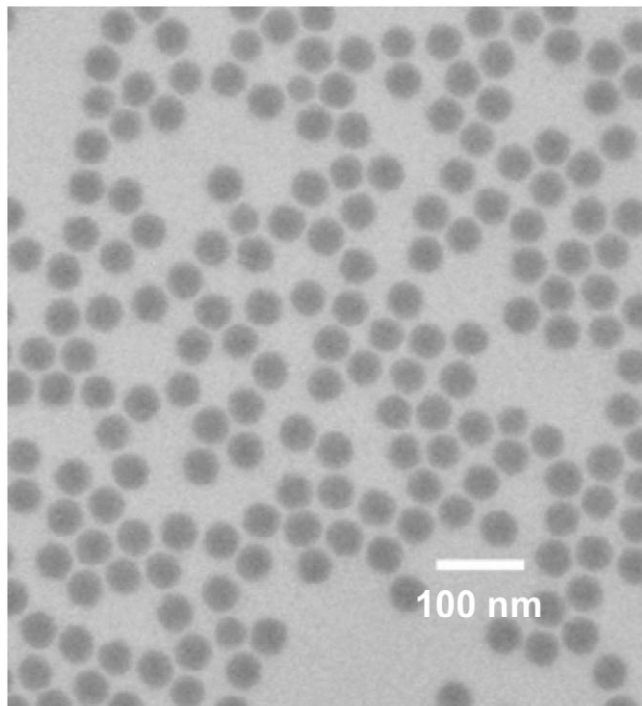


**Figure 6.1** Silica particles synthesized by water-in-oil microemulsion.

Shear-flow is another approach that can be used to improve the CCA ordering.<sup>18-21</sup> Currently, we manually control shear-flow in the CCA dispersion. The ordering would benefit from a mechanically controlled shear-flow process for the CCA fabrication.

For instance, Kanai et al. developed an air-pulse-drive shear-flow for high spectral quality colloidal photonic crystal fabrication as shown in Fig. 6.2a.<sup>22</sup> They demonstrated that the spectral quality of the photonic crystal increased as the pressure increased to a critical pressure as shown in Fig. 6.2b.<sup>22</sup> We can use a similar setup to control the shear-flow for our silica CCA fabrication. We can also connect a peristaltic pump with a flow cell to control the shear-flow of the CCA dispersion for highly ordered CCA fabrication.

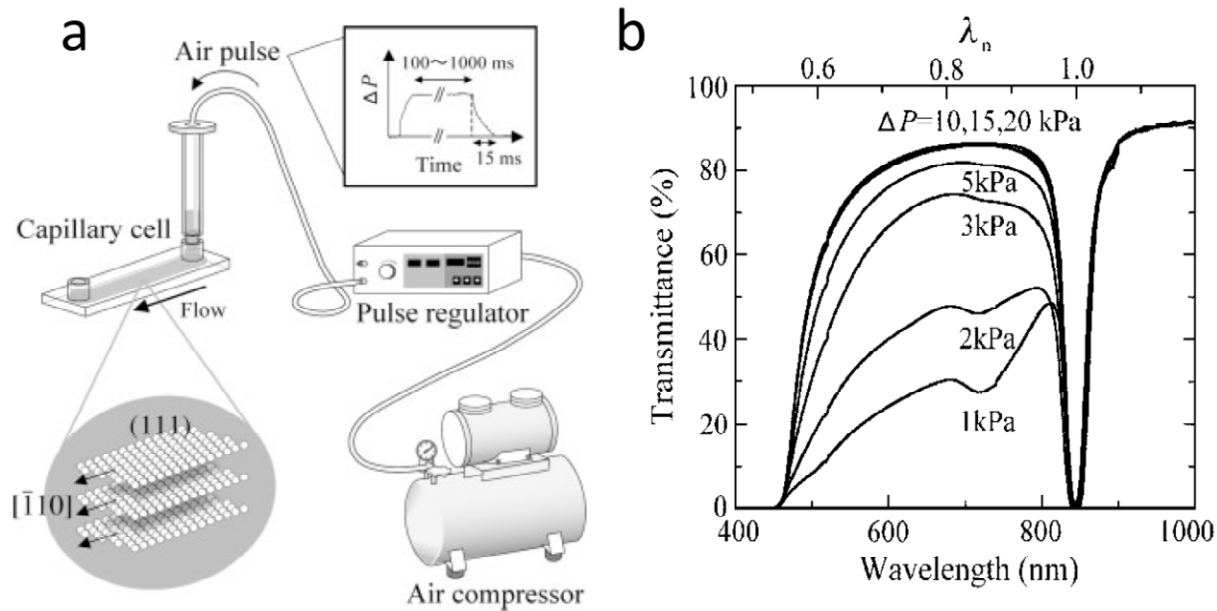


**Figure 6.2** (a) Scheme of the air-pulse-drive system for the uniform colloidal crystal fabrications; (b) Transmission spectra for colloidal crystals produced at various  $\Delta P$ :  $\Delta P$  is the difference from atmospheric pressure. (Both (a) and (b) are from Kanai *et al.*, *Adv. Funct. Mater.* 2005, 15, 25.).

### **6.2.1.2 Silica CCA solidification**

We should also solidify the silica CCA into a poly(vinyl alcohol) hydrogel while keeping the CCA ordering. PVA is used because it has low absorption in deep UV. Asher et al. physically cross-linked a thermoreversible PVA hydrogel within polystyrene CCA to form an enabling photonic crystal material (TGCCA).<sup>23</sup> The TGCCA are stable for weeks or longer at room temperature and further stability can be achieved by irreversibly covalently cross-linking the PVA with glutaraldehyde.<sup>23</sup> Similar work should be applied to silica CCA solidification.

### **6.2.1.3 Silica CCA for imaging applications**

We recently filed a nonprovisional patent application for our CCA deep UV narrow band radiation filter.<sup>24</sup> Light diffraction from the CCA can be angle-tuned over a range of wavelengths. The CCA filter can be used as a novel wavelength-selective optical element for imaging applications.

For instance, Fig. 6.3 shows a diagram of a hyperspectral imaging device that utilizes a CCA deep UV wavelength-selecting device that allows wavelength tuning with a stationary camera.<sup>24</sup> A sample is excited by monochromatic light. A collection lens collimates and directs the light to a Rayleigh rejection CCA filter that blocks the Rayleigh scattered light while passing the Raman scattered light. A wavelength selecting CCA filter Bragg diffracts a specific narrow wavelength band of the collimated Raman scattered light and this collimated diffracted light is directed to a first high-reflectivity mirror that is always parallel to the wavelength selecting CCA filter. The light reflected from the first high-reflectivity mirror is parallel to the light incident to the wavelength selecting CCA filter. The third and fourth high-reflectivity mirrors are placed

such that the displacement of the light after rotation can be compensated. The stationary CCD camera records the sample image at each CCA angle.

The CCA will be angle tuned to diffract adjacent spectral regions. The image obtained at each CCA angle will result from a different narrow wavelength interval. The collection of images of the object (i.e. the star and triangle in Fig. 6.3) over different wavelength bands constitutes a hyperspectral image data set (i.e. images of the object at wavelengths from  $\lambda_1$  to  $\lambda_n$  as shown in Fig. 6.3). The different resulting images are shown in the Fig. 6.3 by the selective appearance of the star and triangle as the different wavelength images are measured from  $\lambda_1$  to  $\lambda_n$ . Each pixel in the image corresponds to a specific location on the object. The variation of the intensity of a given pixel over the spectral wavelength images is the Raman spectrum of that location on the object.

Similarly, the CCA wavelength-selecting device can be also used for transmission based hyperspectral imaging where the CCD camera records the image of the object utilizing the transmitted light through the CCA.

The development of CCA as wavelength-selecting devices will be very important for many imaging applications including Raman, luminescence, transmission, and reflected light hyperspectral imaging.

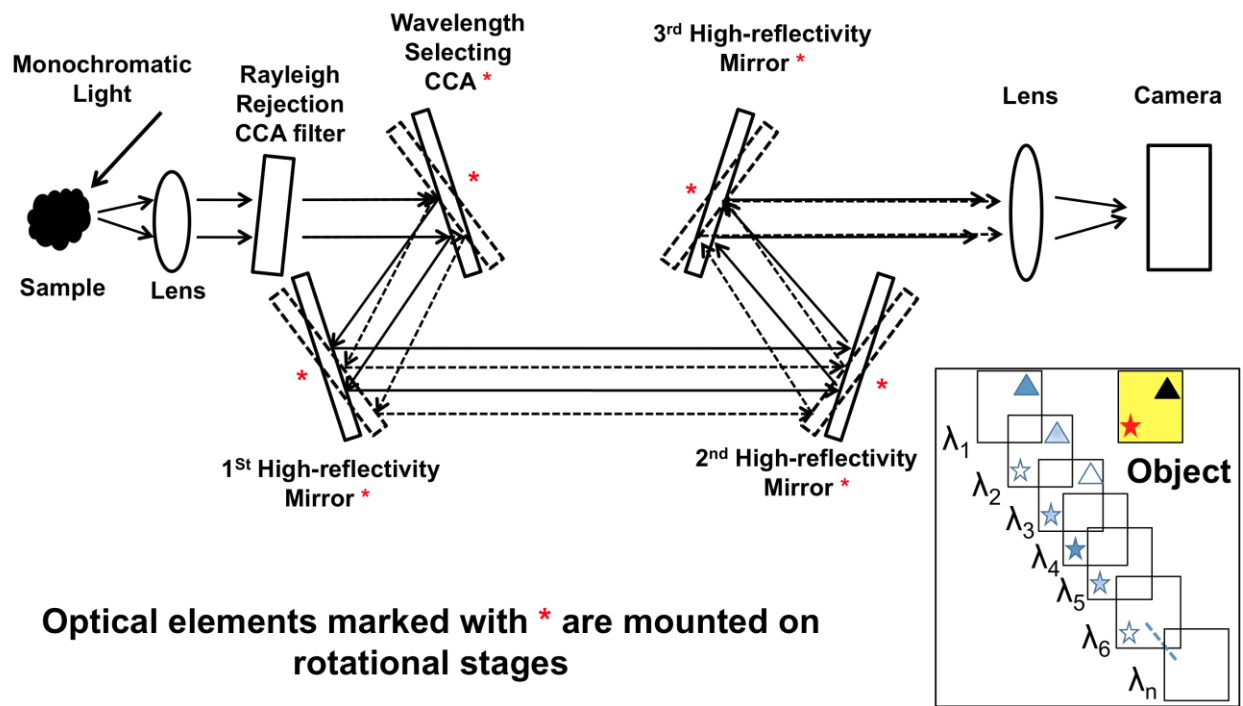


**Figure 6.3** A diagram of a hyperspectral imaging device utilizing a CCA deep UV wavelength-selecting device that allows wavelength tuning with a stationary camera.

## 6.2.2 Future work in solid-state UV Raman cross-section determinations

In Chapter 3, we developed a templated photonic crystal method to fabricate complex stoichiometrically defined nanoparticles.<sup>25</sup> We successfully determined the solid-state  $\text{NaNO}_3$  Raman cross section while avoiding the self-absorption bias by using stoichiometrically defined ( $\text{NaNO}_3/\text{Na}_2\text{SO}_4$ ) nanoparticles.<sup>25</sup> We will use this method to measure the UV Raman cross sections of other solid-state explosive material.

As described in Chapter 3, a solution of the analyte ( $\text{NaNO}_3$ ) and the internal standard ( $\text{Na}_2\text{SO}_4$ ) flowed into the interstices of the close-packed photonic crystals which were then freeze-dried leaving behind complex particles of solid  $\text{NaNO}_3/\text{Na}_2\text{SO}_4$ .<sup>25</sup> Because  $\text{Na}_2\text{SO}_4$  is not resonance enhanced in the deep UV, its Raman cross section is much smaller than that of resonance enhanced materials. For instance, the solid-state  $\text{Na}_2\text{SO}_4$   $\text{SO}_4^{2-}$  symmetric stretching Raman cross section (the strongest band) is  $\sim 100$  times less than that of solid-state  $\text{NaNO}_3$   $\text{NO}_3^-$  symmetric stretching (the strongest band).<sup>25</sup> We would expect a similar ratio of the solid-state  $\text{Na}_2\text{SO}_4$  Raman cross section to the cross sections of solid-state PETN or other explosive material because PETN and other explosive material are resonance enhanced in the deep UV.

The amount of solid  $\text{Na}_2\text{SO}_4$  should be much larger than that of solid  $\text{NaNO}_3$  in order to have comparable Raman intensities of both materials. This is not a problem for solid  $\text{Na}_2\text{SO}_4$  and  $\text{NaNO}_3$  since both are highly soluble in water. However, for analytes such as PETN and the other explosive material, water cannot be used as a solvent.<sup>26</sup> Unfortunately,  $\text{Na}_2\text{SO}_4$  is insoluble in solvents that dissolve PETN and other explosive materials, i.e. acetonitrile.

We will use ammonium nitrate ( $\text{NH}_4\text{NO}_3$ ) as an internal intensity standard for solid-state PETN (or other explosive material) Raman cross section measurements: both  $\text{NH}_4\text{NO}_3$  and PETN (or other explosive material) are resonance enhanced in the deep UV<sup>27</sup>; both  $\text{NH}_4\text{NO}_3$  and

PETN (or other explosive material) are soluble in acetonitrile/water solutions (i.e. 77% acetonitrile/23% H<sub>2</sub>O mixture).<sup>27</sup> We assume the solid-state NO<sub>3</sub><sup>-</sup> UV Raman cross section of NH<sub>4</sub>NO<sub>3</sub> is the same as that of NaNO<sub>3</sub> which has been determined in Chapter 3. We will use the templated photonic crystal method described in Chapter 3 to measure the solid-state UV Raman cross sections of PETN and other explosive material. These solid-state explosive Raman cross sections will be very important for developing explosive detection methods.

### 6.3 REFERENCES

1. Arara, A. K.; Tata, B. V. R. *Adv. Colloid Interface Sci.* **1998**, 78, 49.
2. Allard, M.; Sargent, E. H. *Appl. Phys. Lett.* **2004**, 85, 5887.
3. Rengarajan, R.; Mittleman, D.; Rich, C.; Colvin, V. *Phys. Rev. E* **2005**, 71, 016615.
4. Pusey, P.N. *J. Physique* **1987**, 48, 709.
5. Dickinson, E.; Parker, R. *J. Physique Lett.* **1985**, 46, L-229.
6. Henderson, S. I.; Mortensen, T. C.; Underwood, S. M.; van Megen, W. *Physica A* **1996**, 233, 102.
7. Schöpe, H. J.; Bryant G.; and van Megen, W. *J. Chem. Phys.* **2007**, 127, 084505.
8. Karpov, S. V.; Isaev, I. L.; Gavrilyuk, A. P.; Gerasimov, V. S.; Grachev, A. S. *Colloid Journal* **2009**, 71, 313.
9. Bates, M. A.; Frenkel, D. *J. Chem. Phys.* **1998**, 109, 6193.
10. Yiannourakou, M.; Economou, I. G.; Bitsanis, I. A. *J. Chem. Phys.* **2009**, 130, 194902.

11. Pronk, S.; Frenkel, D. *J. Chem. Phys.* **2004**, 120, 6764.
12. Lacks, D. J.; Wienhoff, J. R. *J. Chem. Phys.* **1999**, 111, 398.
13. Yiannourakou, M.; Economou, I. G.; Bitsanis, I. A. *J. Chem. Phys.* **2010**, 133, 224901.
14. Arriagada, F. J.; Osseo-Asare, K. *J. Colloid Interface Sci.* **1999**, 211, 210.
15. Chang, S.; Liu L.; Asher S. A. *J. Am. Chem. Soc.* **1994**, 116, 6739.
16. Chang, S.; Liu L.; Asher S. A. *J. Am. Chem. Soc.* **1994**, 116, 6745.
17. Bagwe, R. P.; Hilliard, L. R.; Tan, W. *Langmuir* **2006**, 22, 4357.
18. Liu, J.; Weitz, D. A.; Ackerson, B. J. *Phys. Rev. E* **1993**, 48, 1106.
19. Stevens, M. J.; Robbins, M. O. *Phys. Rev. E* **1993**, 48, 3778.
20. Wette, P.; Schöpe, H. J.; Palberg, T. *J. Chem. Phys.* **2005**, 123, 174902
21. Cerdà, J. J.; Sintes, T.; Holm, C.; Sorensen, C. M.; Chakrabarti, A. *Phys. Rev. E* **2008**, 78, 031403.
22. Kanai, T.; Sawada, T.; Toyotama, A.; Kitamura, K. *Adv. Funct. Mater.* **2005**, 15, 25.
23. Asher, S. A.; Kimble, K. W.; Walker, J. P. *Chem. Mater.* **2008**, 20, 7501.
24. Asher, S. A.; Wang L.; Tuschel, D. "Crystalline Colloidal Array Deep UV Narrow Band Radiation Filter", U.S.13/227,066, Patent Pending
25. Wang, L.; Tuschel, D.; Asher, S. A. *J. Phys. Chem. C* **2011**, 115, 15767.
26. Zhuang, L.; Gui, L.; Gillham, R. W. *Environ. Sci. Technol.* **2008**, 42, 4534.
27. Tuschel, D. D.; Mikhonin, A. V.; Lemoff, B. E.; Asher, S. A. *Appl. Spectrosc.* **2010**, 64, 425.